

# Impacts of ionospheric plasma on magnetic reconnection and Earth's magnetosphere dynamics

Sergio Toledo-Redondo<sup>1</sup>, Mats André<sup>2</sup>, Nicolas Aunai<sup>3</sup>, Charles Richard Chappell<sup>4</sup>, Jérémy Dargent<sup>5</sup>, Stephen A. Fuselier<sup>6</sup>, Alex Glozer<sup>7</sup>, Daniel Bruce Graham<sup>2</sup>, Stein Haaland<sup>8</sup>, Michael Hesse<sup>9</sup>, Lynn M. Kistler<sup>10</sup>, Benoit Lavraud<sup>11</sup>, Wenya Li<sup>12</sup>, Thomas Earle Moore<sup>13</sup>, Paul Tenfjord<sup>9</sup>, and Sarah Kimberly Vines<sup>14</sup>

<sup>1</sup>Department of Electromagnetism and Electronics, University of Murcia

<sup>2</sup>Swedish Institute of Space Physics

<sup>3</sup>IRAP, Toulouse, France

<sup>4</sup>Vanderbilt University

<sup>5</sup>Università di Pisa

<sup>6</sup>Southwest Research Institute

<sup>7</sup>NASA/GSFC

<sup>8</sup>Birkeland Centre for Space Science, University of Bergen

<sup>9</sup>University of Bergen

<sup>10</sup>University of New Hampshire

<sup>11</sup>Institut de Recherche en Astrophysique et Planetologie - CNRS

<sup>12</sup>State Key Laboratory of Space Weather

<sup>13</sup>NASA Goddard Space Flight Center

<sup>14</sup>Johns Hopkins University Applied Physics Laboratory

November 21, 2022

## Abstract

Ionospheric ions (mainly H<sup>+</sup>, He<sup>+</sup> and O<sup>+</sup>) escape from the ionosphere and populate the Earth's magnetosphere. Their thermal energies are usually low when they first escape the ionosphere, typically a few eV to tens of eV, but are energized in their journey through the magnetosphere. The ionospheric population is variable, and it makes significant contributions to the magnetospheric mass density in key regions where magnetic reconnection is at work. Solar wind - magnetosphere coupling occurs primarily via magnetic reconnection, a key plasma process that enables transfer of mass and energy into the near-Earth space environment. Reconnection leads to the triggering of magnetospheric storms, aurorae, energetic particle precipitation and a host of other magnetospheric phenomena. Several works in the last decades have attempted to statistically quantify the amount of ionospheric plasma supplied to the magnetosphere, including the two key regions where magnetic reconnection proceeds: the dayside magnetopause and the magnetotail. Recent in-situ observations by the Magnetospheric Multiscale spacecraft and associated modelling have advanced our current understanding of how ionospheric ions alter the magnetic reconnection process at meso- and small-scales, including its onset and efficiency. This article compiles the current understanding of the ionospheric plasma supply to the magnetosphere. It reviews both the quantification of these sources and their effects on the process of magnetic reconnection. It also provides a global description of how the ionospheric ion contribution modifies the way the solar wind couples to the Earth's magnetosphere and how these ions modify the global dynamics of the near-Earth space environment.

# 1 Impacts of ionospheric plasma on magnetic reconnection and Earth's 2 magnetosphere dynamics 3

4 S. Toledo-Redondo<sup>1,2</sup>, M. André<sup>3</sup>, N. Aunai<sup>4</sup>, C. R. Chappell<sup>5</sup>, J. Dargent<sup>6</sup>, S. A. Fuselier<sup>7,8</sup>, A. Glocer<sup>9</sup>, D.  
5 B. Graham<sup>3</sup>, S. Haaland<sup>10,11,12</sup>, M. Hesse<sup>13</sup>, L., M. Kistler<sup>14</sup>, B. Lavraud<sup>2,15</sup>, W. Li<sup>16</sup>, T. E. Moore<sup>8</sup>, P.  
6 Tenfjord<sup>11</sup>, and S. K. Vines<sup>17</sup>

7 <sup>1</sup>Department of Electromagnetism and Electronics, University of Murcia, Murcia, Spain.

8 <sup>2</sup> Institut de Recherche en Astrophysique et Planétologie, Université de Toulouse, CNRS, UPS, CNES,  
9 Toulouse, France.

10 <sup>3</sup>Swedish Institute of Space Physics, Uppsala, Sweden,

11 <sup>4</sup>Laboratoire de Physique des Plasmas, Paris, France,

12 <sup>5</sup>Physics and Astronomy Department, Vanderbilt University, Nashville, TN, USA,

13 <sup>6</sup>Physics Department E. Fermi, University of Pisa, Pisa, Italy,

14 <sup>7</sup>Southwest Research Institute, San Antonio, TX, USA,

15 <sup>8</sup>Department of Physics and Astronomy, University of Texas at San Antonio, San Antonio, TX, USA,

16 <sup>9</sup>NASA Goddard Space Flight Center, Greenbelt, MD, USA,

17 <sup>10</sup>Max-Planck Institute for Solar Systems Research, Göttingen, Germany,

18 <sup>11</sup>Space Plasma Physics Group, University of Bergen, Bergen, Norway,

19 <sup>12</sup>The University Centre in Svalbard Longyearbyen, Norway,

20 <sup>13</sup> Science Directorate, NASA Ames Research Center, Moffett Field, CA,

21 <sup>14</sup>Institute for the Study of Earth Oceans and Space, University of New Hampshire, Durham, NH, USA,

22 <sup>15</sup>Laboratoire d'Astrophysique de Bordeaux, Univ. Bordeaux, CNRS, B18N, allée Geoffroy Saint-Hilaire,  
23 33615 Pessac, France

24 <sup>16</sup>State Key Laboratory of Space Weather, National Space Science Center, Beijing, China,

25 <sup>17</sup>Johns Hopkins University Applied Physics Laboratory, Laurel, MD, USA,

26 Corresponding author: Sergio Toledo-Redondo ([Sergio.Toledo@um.es](mailto:Sergio.Toledo@um.es))

## 27 Key Points:

- 28 • Ionospheric plasma contributes a significant part of the magnetospheric density in the regions  
29 where magnetic reconnection is most frequent
- 30 • Cold and heavy ions of ionospheric origin reduce magnetic reconnection efficiency and modify  
31 energy conversion mechanisms
- 32 • The presence of ionospheric ions and their effects on reconnection and magnetospheric  
33 dynamics are enhanced during geomagnetic storms

## 34 Abstract

35 Ionospheric ions (mainly H<sup>+</sup>, He<sup>+</sup> and O<sup>+</sup>) escape from the ionosphere and populate the Earth's  
36 magnetosphere. Their thermal energies are usually low when they first escape the ionosphere, typically  
37 a few eV to tens of eV, but are energized in their journey through the magnetosphere. The ionospheric  
38 population is variable, and it makes significant contributions to the magnetospheric mass density in key  
39 regions where magnetic reconnection is at work. Solar wind – magnetosphere coupling occurs primarily

40 via magnetic reconnection, a key plasma process that enables transfer of mass and energy into the near-  
41 Earth space environment. Reconnection leads to the triggering of magnetospheric storms, aurorae,  
42 energetic particle precipitation and a host of other magnetospheric phenomena. Several works in the  
43 last decades have attempted to statistically quantify the amount of ionospheric plasma supplied to the  
44 magnetosphere, including the two key regions where magnetic reconnection proceeds: the dayside  
45 magnetopause and the magnetotail. Recent in-situ observations by the Magnetospheric Multiscale  
46 spacecraft and associated modelling have advanced our current understanding of how ionospheric ions  
47 alter the magnetic reconnection process at meso- and small-scales, including its onset and efficiency.  
48 This article compiles the current understanding of the ionospheric plasma supply to the magnetosphere.  
49 It reviews both the quantification of these sources and their effects on the process of magnetic  
50 reconnection. It also provides a global description of how the ionospheric ion contribution modifies the  
51 way the solar wind couples to the Earth's magnetosphere and how these ions modify the global  
52 dynamics of the near-Earth space environment.

### 53 **Plain Language Summary**

54 Above the neutral atmosphere, space is filled with charged particles, which are tied to the Earth's  
55 magnetic field. The particles come from two sources, the solar wind and the upper Earth's atmosphere.  
56 Most of the solar wind particles are deflected by the Earth's magnetic field, but some can penetrate into  
57 near-Earth space. The upper ionized layer of the atmosphere is continuously ejecting particles into  
58 space, which have low energies and are difficult to measure. We investigate the relative importance of  
59 the two charged particle sources for the dynamics of plasma processes in near-Earth space. In particular,  
60 we consider the effects of these sources in magnetic reconnection. Magnetic reconnection allows  
61 initially separated plasma regions to become magnetically connected and mix, and converts magnetic  
62 energy to kinetic energy of charged particles. Magnetic reconnection is the main driver of geomagnetic  
63 activity in the near-Earth space, and is responsible for the release of energy that drives a variety of space  
64 weather effects. We highlight the fact that plasma from the ionized upper atmosphere contributes a  
65 significant part of the density in the key regions where magnetic reconnection is at work, and that this  
66 contribution is larger when the geomagnetic activity is high.

### 67 68 **1 Introduction**

69 Magnetospheric plasma composition and circulation, as well as the sources and sinks of plasma  
70 populations in the magnetosphere, have been extensively studied since the beginning of the space era  
71 in the late 1950s. Magnetospheric ions of ionospheric origin, or ionospheric-originating ions, however,  
72 are difficult to characterize. Their initial low thermal and kinetic energies prevent them from reaching  
73 spacecraft particle detectors and therefore remain invisible until energized, usually far away from the  
74 ionosphere. Nevertheless, using various direct and indirect techniques, past and recent studies have  
75 demonstrated that these particles are important to the dynamics of the Earth's magnetosphere. These  
76 particles ( $H^+$ ), along with heavy ions species such as  $O^+$  and  $He^+$ , often dominate the magnetospheric  
77 mass-density. In the past years, several review works have addressed the current understanding of  
78 these ionospheric ions in the Earth's magnetosphere. Kronberg et al. (2014) reviewed the production  
79 and circulation of ionospheric heavy ions in the nightside and inner magnetosphere, highlighting their  
80 consequences for the plasma sheet, ring current and radiation belts. Chappell (2015) provided a  
81 historical review on the sources and transport of ionospheric ions towards the magnetosphere,  
82 highlighting their main role as a magnetospheric plasma source together with the solar wind. Welling et  
83 al. (2015) made a thorough review of the Earth's magnetosphere plasma sources, transport and losses.  
84 Kistler (2016) analyzed the effects of  $O^+$  coming from the ionosphere in magnetotail dynamics. Yamauchi  
85 (2019) reviewed the terrestrial ion escape and circulation in space using knowledge gained from the

86 Cluster space mission. Finally, Yau et al. (2020) and André et al. (2020) briefly reviewed the escape of  
87 ionospheric ions in the polar regions and their impact on magnetic reconnection.

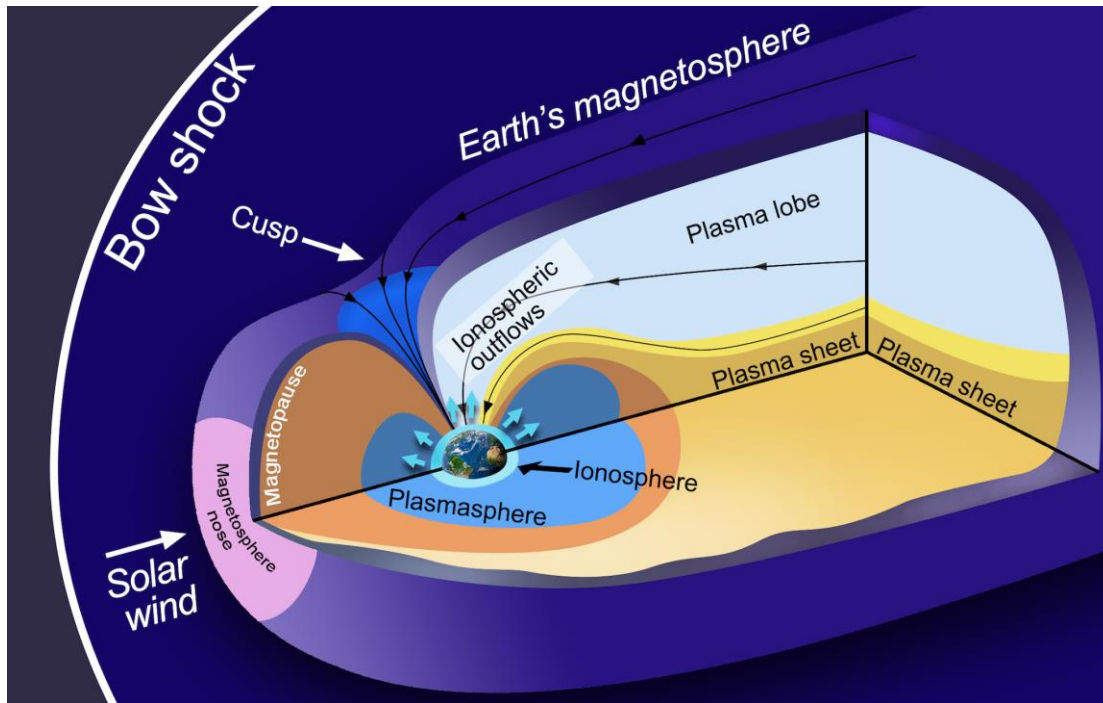
88 In this work, we discuss the implications of ionospheric ions for magnetic reconnection occurring in the  
89 magnetosphere. We focus on the two main regions where magnetic reconnection plays a major role: the  
90 dayside magnetopause and the Earth's magnetotail. In Section 2 we present a summary of the plasma  
91 sources and the transport mechanisms that are relevant for bringing ionospheric plasma to these outer  
92 magnetospheric regions where magnetic reconnection operates. Section 3 presents a review of  
93 observational works that attempted to quantify the amount of ionospheric ions that are present near  
94 the reconnecting regions. Section 4 focuses on how these changes in magnetospheric composition and  
95 plasma properties affect magnetic reconnection, both at the dayside and the tail. In this section, we  
96 review the most relevant numerical simulations and spacecraft observations of magnetic reconnection.  
97 In Section 5, we discuss the implications of having the ionospheric source of plasma in the  
98 magnetosphere, and compile a list of open questions on the subject. Finally, in section 6, we summarize  
99 and highlight the main points of this review.

## 100 **2 Sources and transport of ionospheric ions to the main reconnection regions**

### 101 **2.1 The ionosphere as a source of plasma**

102 The upper atmosphere is partially ionized, and is known as the ionosphere (Figure 1). Ionization occurs  
103 through photoionization by solar EUV emission and other radiation, and sometimes also by precipitating  
104 charged particles, such as accelerated electrons that generate auroras. At the altitudes where collisions  
105 with neutrals in the atmosphere dominate, the energy of charged particles in the ionosphere is of the  
106 order 0.1 eV (Kelley, 2009).

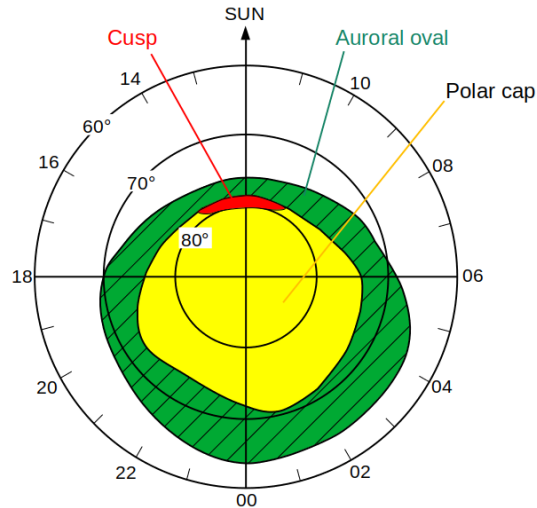
107 At higher altitudes (a few hundred km) the density is lower and the plasma becomes essentially  
108 collisionless. Here low-mass electrons can move to even higher altitudes and create an ambipolar  
109 electric field, pulling positive ions upward (cyan arrows in Figure 1). The typical dynamics of the  
110 ionosphere make ions flow upward along the geomagnetic field. While the heavier ions,  $O^+$ ,  $N^+$ ,  $NO^+$   
111 typically do not reach escape velocity and return to the ionosphere because of the gravitational force,  
112 light ions,  $H^+$  and  $He^+$  can escape upward into the magnetosphere and have been called the 'classical'  
113 polar wind (Banks and Holzer, 1969; Banks, et al., 1971; Schunk et al. 1975). The polar wind occurs from  
114 mid latitudes (above  $\sim 50^\circ$  latitude) all the way to the magnetic poles. Therefore, it supplies the  
115 plasmasphere, the outer magnetosphere and the plasma sheet (see colored regions of Figure 1).  
116 Ionospheric ions, including heavy ions, are also energized by other mechanisms than an ambipolar  
117 electric field, such as waves, which can also make them escape upward into the magnetosphere,  
118 constituting what is often called 'non-classical' polar wind or energetic polar wind. In contrast to the  
119 escape of a few neutral particles in the upper atmosphere, corresponding to the high energy tail of a  
120 Maxwellian velocity distribution in thermodynamic equilibrium, there is no need to heat the whole  
121 atmosphere in order for the charged particles to escape. A major part of the mass outflow from the  
122 Earth's atmosphere is in the form of charged particles.



123

124 **Figure 1.** Main regions of the Earth's magnetosphere. Ionospheric ions are continuously escaping along  
 125 magnetic field lines, and end up in different magnetospheric regions depending on their initial  
 126 geomagnetic location. Credit: J. M. Domínguez, adapted from Pollock et al. (2003).

127 What happens to each individual ion depends strongly on their initial location (latitude and longitude)  
 128 and the magnetospheric conditions at the time (e.g., Huddleston et al., 2005). Due to the configuration  
 129 of the Earth's magnetic field, it is convenient to separately discuss high latitudes and mid latitudes, i.e.,  
 130 roughly above or below the auroral zone (see Figure 2). At high latitudes (section 2.1.1), magnetic field  
 131 lines are open, i.e. connected to the interplanetary magnetic field (IMF) originating from the Sun. The  
 132 source region, i.e., the location where the ions leave the ionosphere, and their transport along the  
 133 continuously changing open magnetic field, connected to the solar wind, determines where the ions go,  
 134 how much they get energized, and where they contribute to the magnetospheric particle populations.  
 135 At mid latitudes (section 2.1.2), where the geomagnetic field lines close back to Earth, the ionospheric  
 136 ions accumulate and form the plasmasphere, see Figure 1.



137

138 **Figure 2.** Top view of the Earth's ionosphere in geomagnetic latitude and local magnetic  
 139 coordinates, indicating typical locations of the auroral oval (green color), the cusp (red)  
 140 cap (yellow). Poleward of the auroral oval, magnetic field lines are open, with the polar cap  
 141 mapping to the tail lobes, and the cusp mapping to the dayside. Adapted from Akasofu (2015).

### 142 2.1.1 High-latitude outflow

143 In the polar cap region, where magnetic field lines are open and connected to the IMF (see Figures 1 and  
 144 2), an ambipolar electric field starts the upflow of ions, above  $\sim 800$  km of altitude. This upflow is the  
 145 basis for the aforementioned "classical" polar wind at high latitudes (Axford, 1968; Banks & Holzer,  
 146 1969). These ions can be further energized by centrifugal acceleration (due to the drift caused by a  
 147 large-scale convection electric field in the curved geomagnetic field), the mirror force (e.g., Comfort,  
 148 1998) and waves. The ions are typically carried toward the magnetotail both by convection and a  
 149 parallel velocity depending on the magnetic field direction. The classical polar wind, or simply polar  
 150 wind, consists of the lighter  $H^+$  and  $He^+$  ions and electrons. A large fraction of these ions has low  
 151 energies, less than tens of eV, up to altitudes of several Earth radii ( $R_E = 6371$  km).

152 The auroral oval and the cusp constitute the regions at the boundary between open and closed  
 153 magnetic field lines. As in the polar cap, ion upflow can be initiated by an ambipolar electric field within  
 154 the dayside cusp and auroral oval. Here additional mechanisms like friction between the neutral  
 155 atmosphere and charged particles affected by a convection electric field in the collisional ionosphere  
 156 also initiate ion heating and upflow (e.g., Schunk 2007). In these regions upflowing ions typically reach  
 157 higher energies than those ions originating from the polar cap. At higher altitudes, collisions are  
 158 negligible, and electric fields in the form of waves or quasi-static structures can energize the ions. The  
 159 energy required to energize the ions can come in the form of waves (often Alfvén waves) generated far  
 160 away from the local upflowing ion population, or can be carried by particles locally producing waves (e.  
 161 g., lower-hybrid waves). The mass composition and energy of the outflow depends highly on the  
 162 ionospheric and magnetospheric conditions. Major ion species comprising ion outflow from the dayside  
 163 cusp and nightside auroral oval are typically  $H^+$ ,  $He^+$  and  $O^+$ , but with contributions also from  $N^+$ ,  $N^{++}$ ,  $O^{++}$   
 164 and  $NO^+$ . These outflows are often referred as "energetic outflows" and were the first indicators of an  
 165 ionospheric source of plasma in the magnetosphere (Shelley et al., 1972).

166 In the dayside cusp, energy often comes from waves or accelerated particles originating from magnetic  
 167 reconnection or other processes at the dayside magnetopause. Wave-particle interactions seen in this

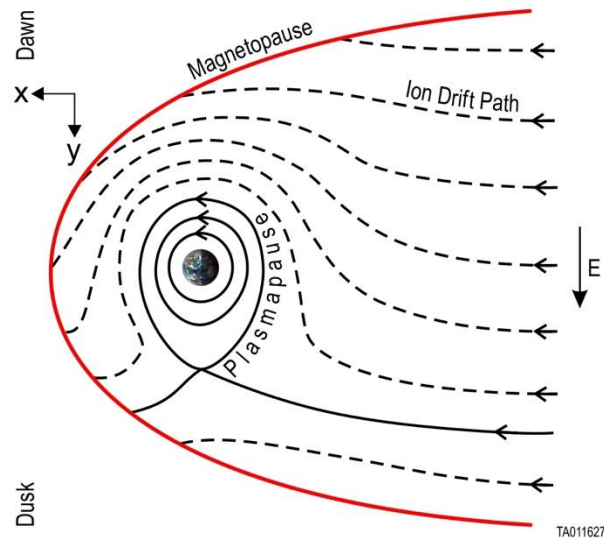
168 region of the ionosphere, particularly interaction with Alfvén waves, often results in ion heating in the  
 169 direction perpendicular to the geomagnetic field. Together with ion motion in a diverging magnetic field,  
 170 this interaction also provides a parallel velocity component, forming so-called conics in ion velocity  
 171 space. These energetic outflows typically move across the polar cap and the lobes of the magnetotail via  
 172 convection during southward IMF periods, with velocities depending on solar wind conditions.  
 173 Sometimes these ions are hard to distinguish from ions originating in the polar cap. Many of these ions  
 174 reach energies of at least one hundred eV at altitudes of several  $R_E$ .

175 In the nightside auroral region, energy can also come from waves or impinging particles originating at  
 176 higher altitudes. Similar to the dayside cusp region, wave-particle interactions often cause outflowing  
 177 ion conics. In addition, quasi-static parallel electric fields are common at altitudes of about one  $R_E$ ,  
 178 accelerating auroral electrons downward towards the Earth and ion beams upward. These energetic  
 179 outflows are typically transported to the inner plasma sheet and the ring current region. Many of these  
 180 outflowing ions reach keV energies at higher altitudes.

181 Ion energization and outflow mechanisms are discussed in several studies; for example, the polar wind is  
 182 discussed by Barakat and Schunk (2006) and Yau et al. (2007), and the dayside cusp and nightside  
 183 auroral region by, e.g., André and Yau (1997), Strangeway et al. (2005) and Moore and Horwitz (2007).  
 184 For the purpose of this review, estimates of typical ion outflow rates are needed, as discussed in several  
 185 papers (e.g., Yau and André, 1997; Su et al., 1998; Cully et al., 2003; Peterson et al., 2006; 2008; André  
 186 et al., 2015; Slapak et al., 2017; Yau et al., 2017; André et al., 2020; Yau et al., 2020). Overall a typical  
 187 outflow rate from the high-latitude region is  $10^{26}$  ions/s, including  $H^+$  and heavier ions such as  $O^+$ . Rates  
 188 vary by at least one order of magnitude, typically increasing with higher solar EUV and geophysical  
 189 activity. This trend is even more pronounced for heavier ions.

### 190 **2.1.2 Mid-latitude outflow: the plasmasphere**

191 The Earth's plasmasphere is a torus of cold ( $<1$  eV), dense ( $10$ 's to  $100$ 's  $cm^{-3}$ ) plasma that occupies the  
 192 inner magnetosphere, typically  $<3-6 R_E$  from the Earth, i.e., at magnetic latitudes up to  $\sim 60^\circ$  (up to L-  
 193 shells 4-5), confined within the near-Earth closed geomagnetic field lines. It is composed primarily of  $H^+$ ,  
 194 with a substantial (1-10%) amount of  $He^+$  and typically much less  $O^+$  (Berube et al., 2005), in addition to  
 195 electrons, originating from the low- to mid-latitude ionosphere. Mechanisms such as the ion outflows  
 196 described above are applicable as the source of plasma escape from the ionosphere towards the  
 197 plasmasphere. The low energy plasma of the plasmasphere approximately co-rotates around the Earth  
 198 on closed plasma drift paths. The outer edge of the plasmasphere, known as the plasmopause,  
 199 separates closed and open drift paths. Because of the interplay between the electric drift, which results  
 200 from the cross-tail electric field set up by the motion of the solar wind past the Earth, and the magnetic  
 201 gradient and curvature drifts due to the near dipolar magnetic field close to the Earth, plasma from the  
 202 magnetotail convects inward and around the duskside or the dawnside depending on the charge and  
 203 energy of the plasma (Figure 3). Ions with low energies, i.e., less than  $\sim 1$  keV, convect downward on  
 204 open drift paths and can encounter the magnetopause on the dawnside or duskside near noon local  
 205 time. By contrast, higher energy ions convect to the duskside on open drift paths that may also  
 206 encounter the magnetopause. At low energies, the convection paths set up a condition whereby the  
 207 plasmasphere has an elongation or bulge on the duskside (e.g., Carpenter et al., 1993). The convection  
 208 path in Figure 3 that separates open drift paths (dashed lines that intersect the magnetopause) from  
 209 closed drift paths (solid lines in the plasmasphere) is called the plasmopause.



210

211 **Figure 3.** Schematic of the open and closed drift paths in the magnetosphere. The cross-tail electric field  
 212 and the gradient and curvature drifts set up energy dependent, open drift paths to the dayside  
 213 magnetopause. The plasmopause is the boundary that separates these open drift paths from closed drift  
 214 paths in the plasmasphere. The Alfvén layer is the solid line that originates in the tail, connects to the  
 215 plasmopause, and extends to the dayside magnetopause. This layer separates open drift paths around  
 216 the dawnside from those on the duskside and indicates the location of the drainage region in the  
 217 dayside magnetopause.

## 218 2.2 Transport of ionospheric plasma in the Earth's magnetosphere

### 219 2.2.1 Plasmaspheric erosion, trough, and wind (mid-latitude outflows)

220 The diagram in Figure 3 illustrates the conditions for relatively quiet and quasi-static magnetospheric  
 221 conditions. These conditions rarely occur. Geomagnetic activity is typically either increasing or  
 222 decreasing as the coupling changes between the Earth's magnetosphere and the highly variable solar  
 223 wind. When geomagnetic activity increases, the plasmasphere contracts, a combined process that  
 224 includes earthward flow on the nightside with erosion of the outer plasmasphere on the duskside. This  
 225 is because, as it contracts, plasmaspheric plasma initially located on closed drift paths suddenly finds  
 226 itself on open drift paths so that the plasma may drain along the newly open drift paths towards the  
 227 magnetopause on the dayside. The plasma convects sunward approximately along the plasmopause  
 228 boundary at a rate of the order of 20 km/s (e.g., Denton et al., 2019). This sunward convection carries  
 229 the eroded plasmasphere material towards the dayside magnetopause. This erosion often produces  
 230 high-density ( $> \text{few cm}^{-3}$ ) clouds of plasma in the outer magnetosphere (Chappell, 1972), typically  
 231 referred to as plasmaspheric plumes or simply plumes. The cross-section of this eroded plasma can be  
 232 quite thin ( $< 1 R_E$ ) or very thick (many  $R_E$ ) (Borovsky and Denton, 2008). The thickness depends on the  
 233 time history of the plasmaspheric erosion and the location and motion of the magnetopause. Typically  
 234 the plasmaspheric plasma encounters the magnetopause on the duskside and late pre-noon sectors.  
 235 This region is commonly referred as the plasmaspheric drainage region.

236 The original plasmaspheric composition does not change as the plasma convects to the magnetopause  
 237 and observations at the magnetopause confirm the dominant  $\text{H}^+$  component, with lower amounts of  $\text{He}^+$   
 238 and  $\text{O}^+$  number densities (Fuselier et al., 2017). However, as the exiting plasmaspheric material  
 239 propagates toward the magnetopause, the magnetic flux tubes originating in and filled with plasma  
 240 from the plasmasphere expand and their density decreases. The magnitude of the decrease in density

241 depends on the convection path and the location of the magnetopause. The plasmaspheric plasma is  
 242 also heated as it expands in the magnetosphere (e.g., Genestreti et al., 2017), although the degree of  
 243 heating is variable and there are certainly times when very cold plasmaspheric material is observed at  
 244 the magnetopause. Finally, the density within the plasmaspheric material is quite variable. Detailed  
 245 density measurements across plumes show variations of an order of magnitude (e.g., Chappell, 1974;  
 246 Goldstein et al., 2004; Borovsky and Denton, 2008). These blobs, fingers and striations align along the  
 247 line that separates drift paths around the dawnside from those on the duskside in Figure 3, i.e., the  
 248 drainage region.

249 In addition to plasmasphere erosion by magnetospheric convection, there are other mechanisms that  
 250 facilitate ion escape from the plasmasphere to the outer magnetosphere: the plasmaspheric trough  
 251 (Chappell et al., 1971) and the plasmaspheric wind (Dandouras et al., 2013).

252 The plasmaspheric trough occurs at magnetic latitudes slightly above the plasmopause. The classical  
 253 polar wind lifts light ions ( $H^+$  and  $He^+$ ) and electrons in the same way as inside the plasmasphere, but this  
 254 plasma is located at open drift paths (see Figure 3), outside the corotating plasmasphere. Typical  
 255 densities of the plasmaspheric trough are  $\sim 10 \text{ cm}^{-3}$  at L-shell = 4 (Chappell, 1971), which drop to few  
 256 tenths of  $\text{cm}^{-3}$  when they reach the magnetopause at L-shells of 10 – 12, due to radial expansion.

257 The plasmaspheric wind is believed to continuously eject material in the radially outward direction, from  
 258 the plasmasphere to the outer magnetosphere, at all local times, as a consequence of diffusion  
 259 occurring at the plasmopause due to the sharp density gradient. This continuous wind was predicted by  
 260 Lemaire and Schunk (1992), and occurs as the result of instabilities at high latitudes that drive plasma  
 261 outwards. However, there is no evidence that the contribution of the plasmaspheric wind to  
 262 plasmasphere erosion is significant.

### 263 **2.2.2 Convection of high-latitude outflows and filter effects**

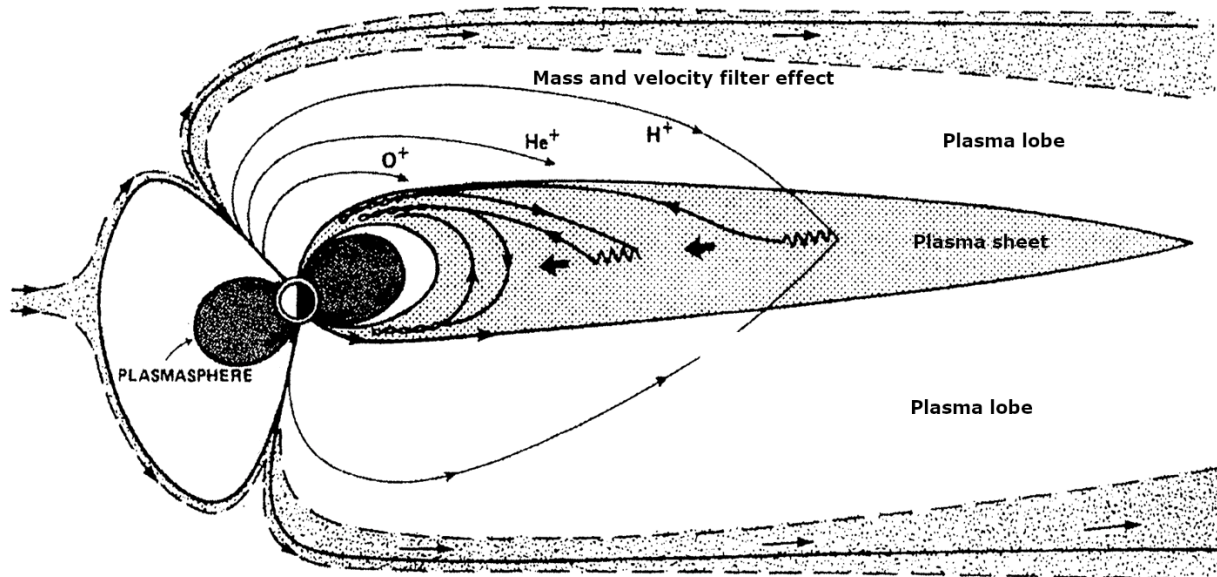
264 When outflowing ions from the ionosphere at high latitudes escape the gravity potential of the Earth  
 265 and reach altitudes above the exobase, collisions are no longer relevant. Plasma is tied to magnetic field  
 266 lines, but can move freely along these lines. Additional magnetic field-aligned (upward) acceleration  
 267 above the exobase takes place as a result of external forces, such as the magnetic mirror force (e.g.,  
 268 Comfort, 1998) or centrifugal acceleration (Cladis et al., 2000; Huddleston et al., 2005, Nilsson et al.,  
 269 2008, 2010). In addition, waves and parallel electric fields accelerate plasma to keV energies in the  
 270 auroral and cusp regions (e.g., André and Yau, 1997).

271 At the same time, the magnetic flux tubes connected to high latitudes move across the polar cap from  
 272 the dayside to the nightside plasma sheet, due to the interaction between the solar wind and the  
 273 magnetosphere at the dayside magnetopause, as described in the Dungey cycle (Dungey, 1963). The  
 274 effective transport of outflowing ions to the magnetosphere is thus the result of the combination of  
 275 magnetic field-aligned outflow and convection. For northward IMF, i.e., when magnetospheric  
 276 convection becomes negligible, escaping ions from the dayside ionosphere travel along reconnected  
 277 field lines directly to the dayside boundary layer (e.g., Fuselier et al., 1989, 2019b; Fuselier, 2020), while  
 278 outflows that originate on the nightside ionosphere will travel towards the magnetotail, following the  
 279 quasi-stagnant magnetic field lines. When magnetospheric convection is at work (typically for  
 280 southward IMF), both dayside and nightside ionospheric outflows are convected towards the  
 281 magnetotail. In situ observations have shown that the  $O^+$  content of the ring current increases during  
 282 geomagnetic storms (e.g., Hamilton et al., 1988, Moore et al., 2001, Grande et al., 2003). Kistler (2020)  
 283 shows that the ionospheric contribution to the near-Earth plasma sheet increases strongly when *Dst*  
 284 drops during the storm main phase.

285 For the same amount of parallel energization, lighter ions have larger parallel velocities than heavy ions.  
 286 On the other hand, magnetospheric convection acts in the same way for all species. As a consequence, a  
 287 mass filter effect arises when magnetospheric convection is non-negligible: lighter ions escaping the  
 288 polar cap region or nightside auroral zone travel further along the magnetic field line before reaching  
 289 the plasma sheet in the magnetotail than heavier ions (Figure 4). A velocity filter effect also applies  
 290 within a single species: the slowest, i.e., less energetic, ions being deposited close to Earth, and faster,  
 291 i.e., more energetic, ions further tailward. Some of the fast ions from this region will escape directly into  
 292 the solar wind and plasma mantle (Slapak et al., 2015, 2017; Schillings et al., 2019; Krcelic et al., 2020)  
 293 and do not contribute to the ionospheric plasma supply of the Earth's magnetosphere.

294 A fraction of escaping ions is able to travel very far down the magnetotail, beyond the distant neutral  
 295 line at around  $100 R_E$  downstream from Earth (Birn et al., 1992, Daly 1986, Nishida et al., 1996), before  
 296 the containing flux tube closes via magnetic reconnection near the neutral line, resulting in the plasma  
 297 being lost downtail (Haaland et al., 2012a). Other ions starting from the same location, but with a lower  
 298 parallel velocity, will not reach as far before the flux tube is convected to the equatorial plasma sheet,  
 299 resulting in the ions being deposited in the magnetotail closer to the Earth, where magnetotail magnetic  
 300 reconnection can take place.

301 During quiet conditions, typically associated with a northward IMF, escaping ions from the nightside  
 302 travel along open field lines that are more or less stagnant (e.g., Lavraud et al., 2002), due to the low  
 303 magnetospheric convection. These ions are more likely to be lost in the distant magnetotail region or  
 304 escape directly into the solar wind than during disturbed conditions. Interestingly, this scenario means  
 305 that ions from the high latitude ionosphere are deposited far downtail during quiet conditions, and  
 306 therefore will spend more time in the plasma sheet, where additional heating and acceleration can take  
 307 place.



308  
 309 **Figure 4.** Schematic illustration of transport paths for ions escaping from the polar cap regions. Owing to  
 310 magnetospheric convection, outflowing ions with the same energy will follow distinct paths depending  
 311 on their mass. In a similar way, outflowing ions of the same species will follow different paths depending  
 312 on their parallel velocity (energy). This is known as a velocity filter effect. Adapted from Chappell et al.  
 313 (1987).

314 In summary, the upward flowing ions from the high-latitude regions are subject to energization along  
315 their individual trajectories. These trajectories depend on the magnetic latitude and local time of their  
316 initial escape from the ionosphere, their initial energy and pitch angle, i.e., angle between their velocity  
317 and the magnetic field direction, and any energization along their path of travel. The energization along  
318 the trajectory depends on waves and parallel electric fields the particles may encounter, on the  
319 changing shape of the magnetosphere, as well as the variable cross tail convection electric field that is  
320 caused by coupling to the solar wind (Huddleston et al., 2005).

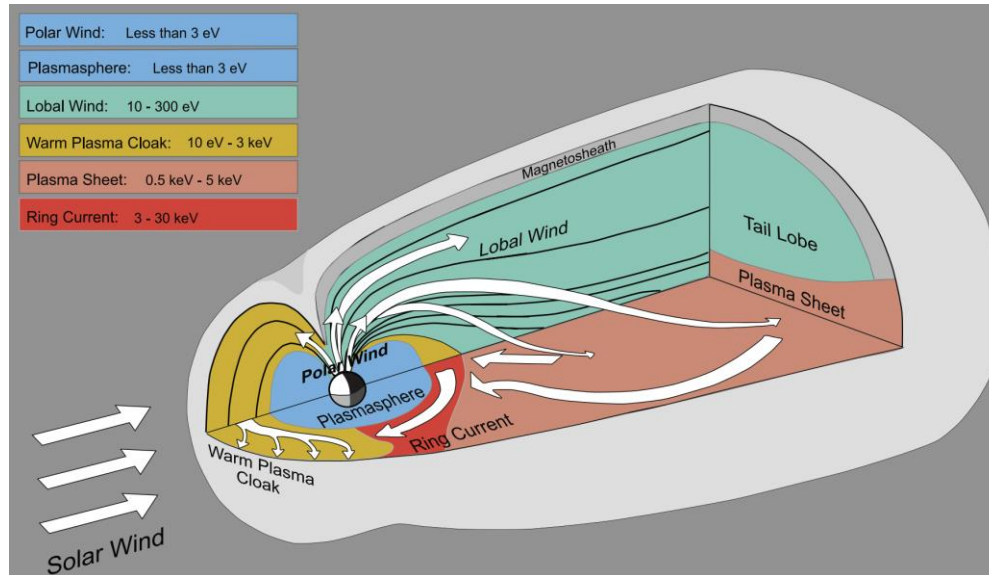
### 321 **2.2.3 Warm plasma cloak**

322 In the early conceptual understanding of the magnetospheric particle populations in the 1960's, there  
323 were three energy ranges of plasma to consider. The first measured was the radiation belts which had  
324 MeV energies and were trapped in two donut shaped regions in the inner magnetosphere, the Van Allen  
325 radiation belts. A second region of plasma, the plasmasphere, was roughly co-located with the radiation  
326 belts but with energies of only a few eV that were directly relatable to the ionospheric ions at lower  
327 altitudes. The third, inter-related regions of the plasma sheet and ring current, with energies of 1's to  
328 10's keV, were thought to be of solar wind origin.

329 As the instrumentation capability improved, an additional category of magnetospheric plasma emerged.  
330 Satellite observations made in the 1970's through 2000's (e.g., the ISEE, DE, Polar, and Cluster missions)  
331 measured the characteristics of a plasma population extending from the nightside through dawn up to  
332 the noon sector outside of the plasmasphere that appeared unrelated to the known magnetospheric  
333 plasma populations in the radiation belts, plasmasphere, magnetotail plasma sheet, and inner  
334 magnetospheric ring current. This plasma population had energies of 10's of eV to a few keV and was  
335 made up of both  $H^+$  and  $O^+$ , suggesting an ionospheric source (e.g., Jahn et al., 2017). These high  
336 energies indicated that this population was not a direct ionospheric upflow originated by classical polar  
337 wind. Because the cross tail convection electric field causes particles to flow from the tail in a sunward  
338 direction, and because lower energy ions drift dawnward, the new region comprising this plasma  
339 population was called the warm plasma cloak (WPC), as the plasma was being "blown" sunward through  
340 the dawn sector to the magnetopause (Chappell et al. 2008).

341 Extensive modeling of ion trajectories has been done by e.g., Delcourt et al. (1989, 1993) and  
342 Huddleston et al. (2005). This modeling shows how the original low energy ionospheric origin ions can  
343 move through the various regions of the Earth's magnetosphere, having their energy and pitch angle  
344 changed as they travel. The energization may be caused by centrifugal acceleration in the polar cap,  
345 initially, followed by the energy-changing effects of curvature and gradient drift in the presence of the  
346 cross-tail convection electric field, which have values of 50 to 100 kV across the magnetospheric tail. The  
347 results of doing statistical trajectory calculations suggest that these up-flowing ions are energized to 100  
348 eV, 1 keV, 20 keV as they move through the different regions. The study did not include acceleration by  
349 waves and parallel electric fields, which would add more energization to ions originating from the cusps  
350 and auroral regions. The net effect of the combination of these different up-flowing ions is to create  
351 both densities and energies that are actually observed in these different regions, indicating that the ion  
352 outflows constitute a primary source of plasma for the Earth's magnetosphere, see figure 5. It was  
353 shown that the source of the warm plasma cloak was indeed the ionosphere. However, unlike the  
354 ionospheric supply to the plasmasphere, where ionospheric ions with energies of a few eV move directly  
355 up the magnetic field line to fill flux tubes, the warm plasma cloak ions come from the ionosphere as  
356 polar wind and polar cusp outflows but follow different trajectories across the polar cap and into the  
357 near-Earth dawnside of the magnetotail where the ions are energized from 10's eV up to a few keV  
358 (Chappell et al, 2008). It was also shown that the ultimate energy of an ionospheric particle that flows

359 up into the magnetosphere is determined by where it enters the center plane of the magnetotail. The  
 360 farther a particle travels down the tail, the more the magnetic field lines are distended in the center  
 361 plane of the tail and the more curvature drift the particle will encounter when it enters this region.  
 362 Particles which become the warm plasma cloak enter the tail earthward of those which become the  
 363 plasma sheet and subsequently the ring current.



364

365 **Figure 5.** Schematic summarizing the particle tracing results from Delcourt et al. (1993) and Huddleston  
 366 et al. (2005). The ions of ionospheric origin are energized as they travel in the Earth's magnetosphere.  
 367 Adapted from Chappell et al. (2008).

368 Of direct significance to this review is the fact that the warm plasma cloak particles are convected past  
 369 dawn to the post-noon magnetopause where they enter the reconnection region at the nose of the  
 370 magnetosphere, changing the plasma characteristics both by energy and mass and thus affecting the  
 371 rate of reconnection on the dayside, see sections 3 and 4. A corollary to this, of course, is that the entry  
 372 of the ionospheric ions into the centerline of the magnetotail also affects the reconnection process  
 373 there. As the polar/lobal wind particles (10's to 100's of eV) enter the distended field lines of this region,  
 374 they will begin to be accelerated, thereby influencing the conditions conducive for magnetic  
 375 reconnection in the magnetotail.

376 In summary, the flow of ionization from the ionosphere through the lobes to the central plane of the  
 377 magnetosphere affects two different areas of reconnection, initially the neutral sheet area of the tail  
 378 and potentially, through the sunward flow of the warm plasma cloak to the dayside magnetopause.

### 379 **2.3 The ionospheric plasma source from a global modelling perspective**

380 While the magnetosphere is known to have two sources of plasma, the solar wind and the ionosphere,  
 381 global magnetospheric models have for many years only included the solar wind source. The first  
 382 models to include an explicit source of ionospheric plasma appeared more than 20 years ago (e.g.,  
 383 Winglee 1998), but the regular inclusion of ionospheric outflows into global models is a relatively recent  
 384 innovation. There are multiple approaches to modeling the source and impacts of ionospheric plasma in  
 385 the magnetosphere implemented in different studies, but these disparate approaches all demonstrate  
 386 that ion outflows can have a profound effect on the near-Earth space environment.

387 Tracking ionospheric plasma as it flows through the magnetosphere requires two critical components: 1)  
388 a model capable of following disparate plasma populations, and 2) a specification of the ionospheric  
389 source of plasma. One method of tracking the flow of ionospheric plasma through the magnetosphere  
390 involves tracking large numbers of test particles, launched from the ionosphere, through either static or  
391 dynamic fields using MHD (e.g., Perroomian et al., 2007, Moore et al., 2005). Such an approach has the  
392 advantage of allowing for kinetic effects and non-Maxwellian particle distributions as the full equation of  
393 motion is evolved for many particles. This test-particle method has the disadvantage is that the particles  
394 and fields do not evolve self-consistently. An alternative approach that has been more actively pursued  
395 in recent years is to track each source of plasma separately in its own fluid in a multi-fluid MHD model of  
396 the magnetosphere (e.g., Winglee et al., 2002, Glocer et al. 2009, 2018, 2020, Wiltberger et al., 2010).  
397 While this methodology does not allow for non-Maxwellian distributions, it does allow for the self-  
398 consistent evolution of both plasma and electromagnetic fields.

399 In terms of specification of the ionospheric source, three methods are commonly used. The simplest  
400 method is to specify an ionospheric boundary density which acts as a reservoir from which diffusion and  
401 MHD forces effectively pull ionospheric plasma into the magnetospheric simulation domain. This  
402 approach was studied extensively by Welling and Liemohn (2014) and found to roughly approximate the  
403 observed statistical pattern of ionospheric outflow. A more causally regulated method for representing  
404 the outflow is to apply a statistical relationship connecting magnetospheric energy inputs with escaping  
405 plasma developed from the FAST (Strangeway et al., 2005) or Polar (Zheng et al., 2005) spacecraft  
406 mission data. This approach has been applied in both test particle and multi-fluid MHD models (e.g.,  
407 Brambles et al., 2010, Moore et al., 2005). The applicability and uncertainties inherent in the underlying  
408 statistical models of outflow has led in recent years to the incorporation of physics-based first principles  
409 models of ion escape in to magnetospheric models to represent the ionospheric source (Glocher et al.,  
410 2009; Varney et al., 2016a; Welling et al., 2016).

411 Although the approaches to studying the influence of ionospheric plasma on magnetosphere dynamics  
412 differ, they have demonstrated that ion outflow has wide ranging influences on the broader space  
413 environment. Moore and Delcourt (1995) introduced the concept of the geopause as boundary inside of  
414 which the plasma is primarily of ionospheric origin. The location of the geopause is found to depend  
415 heavily on the solar wind IMF orientation (Winglee, 1998) and may have significant North-South  
416 asymmetries (Li et al., 2000). The different transport paths to the magnetosphere taken by disparate  
417 plasma sources are found to have a major influence on the ring current. For example, polar wind  
418 protons and solar wind protons contribute similarly to the ring current during a geomagnetic storm, but  
419 the solar wind-originating protons have a higher mean energy due to a longer inward travel path from  
420 the tail (Moore et al., 2005). The different plasma trajectories through the magnetosphere also result in  
421 local time-dependent injections of plasma of different species into the ring current (Welling et al., 2011).

422 In simulations, ion outflows are also found to have large scale consequences for the magnetosphere.  
423 Indeed, simulations that include outflow often have a lower cross polar cap potential, and hence  
424 reduced global convection (Glocher et al., 2009; Wiltberger et al., 2010; Welling & Zaharia, 2012).  
425 Simulations that include ionospheric outflow with self-consistent feedback between the particles and  
426 fields are better able to reproduce observed magnetic fields (Glocher et al., 2009). Intriguingly,  
427 simulations by Brambles et al. (2010) suggest a potential connection between the escape of ionospheric  
428 outflow and periodic sawtooth oscillations (one particular manifestation of geomagnetic activity). These  
429 simulations were later reproduced with a more physically realistic simulation (Varney et al., 2016b), but  
430 the proposed mechanism remains an actively debated topic in the magnetospheric and ionospheric  
431 communities (e.g., Liao et al., 2014; Lund et al., 2018). In addition to sawtooth events,  $O^+$  from the  
432 ionosphere is found to have a significant influence on dynamics in the magnetotail, such as bursty bulk

433 flows (Garcia et al., 2010, Garcia-Sage et al., 2015). Glocer et al. (2020) modeled separate  $H^+$  fluids from  
434 the ionosphere and the solar wind and showed a significant contribution of ionospheric  $H^+$  to both the  
435 plasma sheet and the ring current regions during times of southward IMF. The model also showed that  
436 the ring current contains both ionospheric  $O^+$  and  $H^+$  making the ionospheric contribution dominant over  
437 the solar wind  $H^+$  and  $He^{++}$ .

#### 438 **2.4 Final considerations on the role of the ionosphere as a source of magnetospheric plasma**

439 In the early years of magnetospheric physics, an important role for the ionosphere was recognized, but  
440 mainly as a region that was responding to the inflow of particle and wave energy from the energetic  
441 particle populations above. While the link between the plasma sheet and ring current regions to the  
442 auroral oval with particles, electromagnetic fields, and currents was accepted and studied, the role of  
443 the ionosphere as a source of the more energetic particles was neither fully realized nor understood  
444 (Chappell, 2015).

445 Advances in instrumentation that could measure the low (eV), medium (100 eV -1's keV) and higher  
446 energy (10 keV -100 keV) particles combined with the ability to separate masses were a critical new  
447 contribution. In the 1970's, 80's and 90's this improved instrumentation enabled the observation of a  
448 significant up-flow of ions from the ionosphere out into the magnetosphere (ISEE, Akebono, DE, Cluster,  
449 Polar). Early estimates of the contributions of these initially low energy particles showed that they were  
450 sufficient in terms of density to create the major observed plasma regions of the magnetosphere  
451 (Chappell et al., 1987). Later ion trajectory studies of these up-flowing cold ions showed that they not  
452 only moved through the different magnetospheric regions, but in so doing were energized to match the  
453 observed energies in these regions (plasmasphere, plasma sheet, warm plasma cloak, and ring current)  
454 (Delcourt et al., 1993, Huddleston et al., 2005). In addition, more recent studies show that the changing  
455 low energy plasma of the inner magnetosphere can have a significant effect on changing wave  
456 generation and propagation which can affect the creation and loss of the very energetic radiation belt  
457 electrons and ions (e.g., Thorne, 2010).

458 As discussed above, for the outflowing ions in the polar cap and lobes, the distance that they travel  
459 down the tail is controlled continuously by the changing solar wind magnetic field and velocity (Haaland  
460 et al., 2012b; Liemohn et al., 2007). The entry point of the ions from the lobe into the central plane of  
461 the magnetotail determines their subsequent trajectories and how much they will be energized (see also  
462 Figure 4). Huddleston et al. (2005) used a combination of data from the Thermal Plasma Dynamics  
463 Experiment (TIDE) on the Polar spacecraft combined with ion trajectories based on the work of Delcourt  
464 et al. (1993). Using TIDE measurement of the outflowing ions (2 eV - 400 eV) above the ionosphere as  
465 input to the trajectory models, Huddleston et al. (2005) showed that the sum of the outflowing  
466 ionospheric-originating ions, combined with the outflowing polar cusp ions and some nightside auroral  
467 zone upflowing ions, give enough flux to fill the plasma sheet to the densities that are observed.

468 One further consideration is the timing required for the two sources, solar wind and ionosphere, to add  
469 plasma to the plasma sheet. Sorathia et al. (2019) used particle tracing from the solar wind at the bow  
470 shock into the magnetosphere during northward IMF, which is the favorable condition to convect solar  
471 wind ions into the plasma sheet region by the Kelvin-Helmholtz instability between the magnetosheath  
472 and the flank magnetosphere. The solar wind ion access takes about 3 hours to move from the bow  
473 shock to the outer plasma sheet and add the particles. In contrast, when the IMF shifts to southward,  
474 the outflowing ions already in the tail lobes can be convected into the center of the plasma sheet in a  
475 matter of tens of minutes to an hour depending on their location in the lobe.

476 Finally, we want to emphasize an important consideration about basic nomenclature. For up-flowing  
 477 ionospheric ions, cold plasma and ionospheric plasma are not necessarily synonymous. There are  
 478 instances, particularly in the plasmasphere region where the outflowing ionospheric ions are not  
 479 energized as they fill up the dipolar flux tubes that are corotating, hence cold and ionospheric are the  
 480 same. At higher L-shells, however, where the ions are carried back into the tail, their energies can be  
 481 significantly changed by their particular trajectories, hence the ions are still from an ionospheric source  
 482 but can have total energies  $>1000$  eV (bulk acceleration plus thermalization). The extension of this  
 483 realization is that in the reconnection region of the magnetotail, there can be instances where lower  
 484 energy cold ions can enter the reconnection region, but it is also the case that the hotter plasmas that  
 485 are involved in the reconnection process are often ionospheric-originated.

### 486 **3 Quantification of ionospheric plasma near the reconnecting regions**

487 As described in Section 2, the escape and transport of ionospheric ions into the various regions of the  
 488 magnetosphere depends on multiple interrelated processes, including for instance energy deposition in  
 489 the ionosphere and magnetospheric convection. This section compiles all the statistical work that has  
 490 quantified the contributions of the ionospheric plasma source to the regions where magnetic  
 491 reconnection, the primary mechanism for coupling with the solar wind and driving energy in the Earth's  
 492 magnetosphere, occurs.

493 There have been recent global modelling efforts including the ionospheric source, which clearly indicate  
 494 their relevance for populating the Earth's magnetosphere, as discussed in section 2.3. The main  
 495 drawback of these models is that they need to couple many different physical processes occurring at  
 496 very different spatial scales and plasma regimes, from the highly collisional ionosphere, including  
 497 chemical processes to assess the plasma density and composition, to the collisionless magnetosphere  
 498 and convection of the magnetic field lines.

499 In the following subsections, we first describe the techniques for detecting cold ions (up to  $\sim 10$  eV),  
 500 corresponding to the initial energy of ionospheric ions when they escape to the magnetosphere. Then,  
 501 we review all the available statistical in-situ and remote observations near the two main reconnection  
 502 regions in the Earth's magnetosphere: the dayside magnetopause and the magnetotail. We describe and  
 503 put together the statistics of observations of cold ionospheric-originating ions in these two key regions.  
 504 As mentioned in section 2, not all ions of ionospheric origin are cold when they reach the reconnection  
 505 regions. However, from an observational perspective, it is not possible to distinguish the origin of hot  
 506 (keV) protons. The cold ions discussed in this section correspond to the young ionospheric plasma  
 507 supply, in the sense that they did not yet have time to be energized significantly, and correspond  
 508 unequivocally to the ionospheric source.

#### 509 **3.1 Techniques for cold ion measurements**

510 While ionospheric-originating ions are very important for understanding magnetospheric dynamics and  
 511 the coupling of the solar wind and magnetosphere to the ionosphere and underlying atmosphere, ions  
 512 with energies of less than  $\sim 10$  eV, such as those directly originating from ionospheric outflow and the  
 513 plasmasphere, are often hard to detect in space plasmas. A main source of this difficulty arises from the  
 514 fact that a sunlit spacecraft in a low-density plasma becomes positively charged up to tens of volts  
 515 (Grard, 1973; Garrett, 1981; Whipple, 1981). Hence, positively charged ions at very low energies will not  
 516 reach the spacecraft and cannot directly be detected. Various techniques have been developed to  
 517 overcome this challenge (André and Cully, 2012).

518 Remote sensing can be used to detect plasmas of both low and high energy. For example, actively  
 519 transmitting ground-based ionosondes and top-side sounding from a spacecraft has been used to

520 determine the plasma density at a specific altitude (Benson, 2010). With ground-based radars and  
521 incoherent scatter radars, several plasma parameters of the ionospheric plasma populations can be  
522 estimated (Ogawa et al., 2009). In the magnetosphere, passive remote sensing with instruments on  
523 spacecraft detect EUV solar photons resonantly scattered from He<sup>+</sup> ions (Spasojevic and Sandel, 2010).  
524 Also, energetic neutral atoms (ENAs) produced by charge-exchange between magnetospheric ions and  
525 hydrogen atoms in the exosphere travel in line-of-sight paths to a spacecraft and are detected at  
526 energies at least down to tens of eV (Sandel et al., 2003; Fuselier et al., 2020a), allowing for inference of  
527 the low-energy plasma populations in certain regions.

528 Observing plasma in situ with detectors onboard a spacecraft allows for direct measurements of local  
529 plasma properties, but adds uncertainties in the observations caused by interaction of the spacecraft  
530 itself with the plasma. In the source region of ionospheric outflow, the plasma density can be so high  
531 that the spacecraft potential becomes zero or slightly negative, due to many impacting electrons on the  
532 spacecraft surface, allowing for low-energy populations to be measured. At altitudes of a few hundred  
533 km ion detectors are used to study positive ions at low energies (Shen et al., 2018). Additionally,  
534 Langmuir probes are used to determine electron density and temperature in dense plasmas (Brace,  
535 2013; Knudsen et al., 2017).

536 At higher altitudes in a low-density plasma, low-energy ions are still able to be observed in situ, for  
537 instance when a satellite is in eclipse (i.e., in the Earth's shadow) during short periods, and hence  
538 become negatively charged (Seki et al., 2003). When a spacecraft is positively charged, an indirect  
539 method for measuring the cold ion density is to estimate the total plasma density from observations of  
540 electromagnetic wave emission at the electron plasma frequency or upper hybrid frequency, and  
541 subtract the ion density deduced from particle detectors (Sauvaud et al., 2001; Lee et al. 2012; Jahn et  
542 al., 2020; Fuselier et al., 2020b). In addition, the total plasma density is estimated from the spacecraft  
543 potential. This potential depends on the density and the electron temperature but can in many  
544 magnetospheric plasmas be calibrated and used to estimate the total density (e.g. Grard, 1973; Laakso  
545 and Pedersen, 1998; Lybekk et al., 2012; Jahn et al., 2020). To obtain particle distribution functions in  
546 velocity space, the positive charging of the spacecraft that repels the positive ions must be reduced. One  
547 method is to use a negatively charged aperture plane around the ion detector entrance, as was used for  
548 the RIMS instrument on Dynamics Explorer (Chappell et al. 1980). An alternative approach is to  
549 negatively bias the entire instrument or a large part of the spacecraft as done for the Magnetospheric  
550 Plasma Analyzers (MPAs) on certain geosynchronous spacecraft (Borovsky et al., 1998). Yet another  
551 alternative approach used by some missions is to reduce the charging of the whole spacecraft by  
552 emitting a plasma cloud (Moore et al., 1997; Su et al., 1998) or a beam of positive ions (Torkar et al.,  
553 2016), but often a spacecraft potential of a few volts remains. We note that several studies concentrate  
554 on initially cold ions that have been heated (i.e., larger thermal velocity than expected given the  
555 plasmaspheric or ionospheric source) or are drifting, e.g., due to  $\mathbf{E} \times \mathbf{B}$  motion, i.e., large enough bulk  
556 velocity to overcome the spacecraft charging (e.g., Lee and Angelopoulos, 2014). In these situations ion  
557 detectors on a positively charged spacecraft are still effective (e.g., Sauvaud et al., 2001; Lavraud et al.,  
558 2005), and accurate estimations of the densities of these cold populations requires moment calculations  
559 that properly account for the spacecraft potential (e.g., Lavraud & Larson, 2016).

560 An alternative method for determining the presence and properties of a cold ion population utilizes the  
561 fact that a supersonic flow of cold positive ions can create a large enhanced wake behind a positively  
562 charged spacecraft. The wake will be filled with electrons with a thermal energy that is higher than the  
563 ram kinetic energy, in contrast to that of the ions. This creates a local electric field which can be  
564 observed and then used to detect the presence of cold ions. Using multiple instruments to measure the  
565 geophysical electric field, magnetic field, and spacecraft potential in order to estimate the total plasma

566 density, the cold ion flux can be deduced (Engwall et al., 2009). This method requires one technique to  
 567 determine the local electric field, such as detecting the potential difference between probes on wire  
 568 booms in the spin-plane of a spinning spacecraft, and another to characterize the essentially  
 569 unperturbed geophysical electric field, such as detecting the drift of artificially emitted keV electrons  
 570 gyrating back to the spacecraft, as is done with an instrument onboard the Cluster and Magnetospheric  
 571 Multiscale (MMS) missions. Such observations from the Cluster satellites have been used for statistical  
 572 studies covering a major part of solar cycle (André et al., 2015). In addition, observations from the MMS  
 573 spacecraft have been used to show that charging of the individual wire booms affects observations, but  
 574 can also be used to obtain information on cold ions (Toledo-Redondo et al., 2019).

### 575 **3.2 Quantification of ionospheric-originating ions at the dayside magnetopause**

576 In this subsection, we summarize the findings of the statistical studies found in the literature which  
 577 attempted to infer the properties of ions of ionospheric origin present at the dayside magnetopause,  
 578 i.e., the region where the magnetosphere couples to the solar wind via magnetic reconnection. Most of  
 579 these studies are based on in-situ observations, which are local in nature and orbit dependent. Inferring  
 580 the global properties of the ionospheric component at the dayside magnetosphere by means of in-situ  
 581 observations can only be done from a statistical perspective, using from months to years of spacecraft  
 582 observations. Different missions have different orbits, including equatorial versus polar orbits, and  
 583 different or even varying apogee and perigee distances. In addition, the dayside magnetopause location  
 584 is dynamic, most of the time being located between 8 – 12  $R_E$  from Earth. Another important difference  
 585 between studies is the instruments and associated techniques they use for inferring the plasma  
 586 properties, in particular density, composition and temperature. We decided to group the studies by the  
 587 main technique they use for cold ion detection. Since the studies reviewed in this section use different  
 588 spacecraft, different techniques, and even different definitions of ionospheric plasma, one needs to be  
 589 careful when comparing their results. We tried to enunciate the main points to consider for each of  
 590 these studies when discussed together. At the end of this sub-section, we provide a table with the main  
 591 findings, compare the results of each of these studies and draw conclusions from putting all these  
 592 observations together.

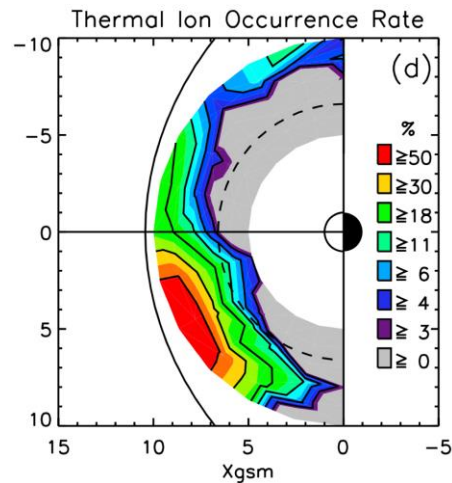
#### 593 **3.2.1 Studies based on in-situ ion detectors**

594 The most straightforward technique to infer the properties of cold ions in space plasmas is by using the  
 595 low-energy range (up to few tens or few hundred eV) of ion detectors onboard spacecraft. The main  
 596 problem of this approach is that any ion with total energy (bulk drift energy plus thermal energy) lower  
 597 than the spacecraft potential will not be detected, cf. Section 3.1. While this is not a problem for  
 598 detecting the WPC (typical thermal energies of few hundred eV), it poses a serious challenge for  
 599 detecting plasmaspheric material (typical thermal energies in the eV range).

600 Chappell (1974) performed a statistical analysis of the plasmaspheric plume properties using OGO 5  
 601 satellite (equatorial orbit). He reported 73 cases (orbits) of observations of exiting plasmasphere  
 602 material in the dayside magnetosphere, at L-shells  $> 4$ . He reports only peak densities and found an  
 603 average peak density of  $\sim 65 \text{ cm}^{-3}$ , and the observations being concentrated in 9:00 – 21:00 Local Time  
 604 (LT) sector, i.e., mainly in the drainage region.

605 Chen and Moore (2006) used 3.5 years (January 2000 - June 2003) of the Polar spacecraft (polar orbit)  
 606 data to infer the statistical probability of observing thermal ions (cold ions, i.e., eV temperature but any  
 607 drift velocity) as a function of local time in the dayside magnetosphere. This method allowed for  
 608 detection of the plasmaspheric material but disregarded WPC events, which are often not so cold.  
 609 Thermal ions were detected 50% of the time near the dusk side magnetopause, while the occurrence

610 near the dawn-side magnetopause was 30% (see Figure 6), considering as detection any flux above the  
 611 noise level of the instrument at the low energy range. Their occurrence probabilities are higher for  
 612 larger L-shells, and this is because the ion detector requires that the bulk plasma velocity has higher  
 613 energies than the equivalent spacecraft potential (typically few to several V). This occurs preferentially  
 614 near the magnetopause, where local motions of the boundary and ULF waves accelerate the cold  
 615 plasma to energies above the spacecraft potential. The dawn-dusk asymmetry is explained by the  
 616 location of the drainage region, which is predominantly in the dusk sector. Finally, they also compared  
 617 the statistical occurrence of thermal ions with the orientation of the solar wind magnetic field, or  
 618 Interplanetary Magnetic Field (IMF). They found a larger occurrence probability of thermal ions during  
 619 southward IMF periods, consistent with the picture of enhanced magnetic reconnection and  
 620 magnetospheric convection that facilitates erosion of the plasmasphere, including plume formation.

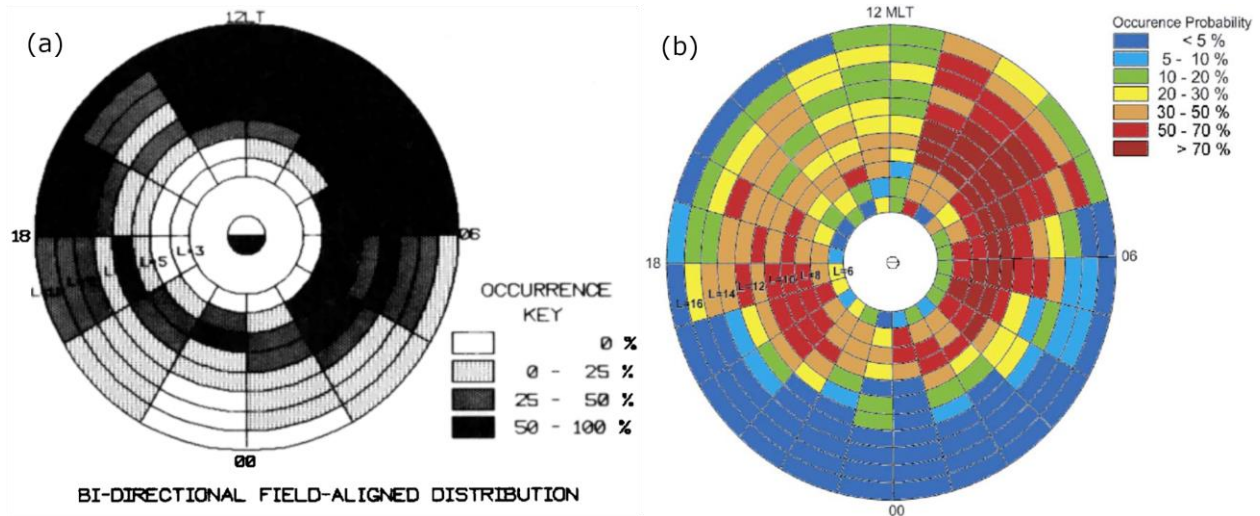


621  
 622 **Figure 6.** Occurrence probability of thermal ions, based on 3.5 years of POLAR spacecraft observations.  
 623 Adapted from Chen and Moore (2006).

624 Borovsky and Denton (2008) used 210 plasmaspheric plume events during geomagnetic storms,  
 625 observed at geosynchronous orbit ( $6.6 R_E$ ) by the MPA onboard Los Alamos satellites (equatorial orbit).  
 626 They found that plasmaspheric plumes are a persistent feature of geomagnetic storms, and that they  
 627 last for  $\sim 4$  days. Their typical flow velocities are  $\sim 15$  km/s towards dayside magnetopause. The average  
 628 mass flux is  $\sim 2 \times 10^{26}$  ions/s, and the average mass released per event is  $\sim 2 \times 10^{31}$  ions. These numbers  
 629 indicate that plumes constitute a primary escaping path of plasma. The plume plasma density, flow  
 630 velocity and width all decrease with the plume age. However, these observations are taken far away  
 631 from the Earth's magnetopause, which is typically situated at  $\sim 10 R_E$ . Assuming an effective area of the  
 632 drainage plume region at the magnetopause of  $\sim 9 \times 12 R_E$ , as in André and Cully (2012), and an average  
 633 outflow velocity of  $\sim 15$  km/s (Borovsky and Denton, 2008), the resulting ionospheric average density at  
 634 the magnetopause in the drainage region corresponds to  $\sim 3$  cm $^{-3}$  during storm times.

635 The previous studies discussed the presence of plasmaspheric material in the outer, dayside  
 636 magnetosphere. Another important population that brings ionospheric-originating ions to the dayside  
 637 magnetopause is the WPC (cf. section 2.2.3). Nagai et al. (1983) analyzed ISEE-1 (equatorial orbit,  $30^\circ$   
 638 inclination) data (June 1978 – December 1980) and searched for field-aligned bidirectional ion jets in the  
 639 energy range 10 – 100 eV, and found occurrences larger than 50% at the dawn side magnetopause (L-  
 640 shells  $\sim 10$ , see Figure 7a). Their search criteria match with the properties of the WPC. Similar results are  
 641 obtained by Chappell et al. (2008), who analyzed 1 year (March 2001 – March 2002) of Polar spacecraft  
 642 data (polar orbit) searching for the WPC population. Their criteria were to find bidirectional, field aligned

643 ions in the energy range 10 – 400 eV within 1 L-shell portion of the orbit. They did not impose a  
 644 minimum density threshold for the bidirectional jets. They found, for L-shells of 10 – 12, i.e., the region  
 645 where the magnetopause is located, WPC detections of 30 – 50 % in the dusk side and > 70 % in the  
 646 dawn side (see Figure 7b), with larger occurrence for latitudes < 30°.



647

648 **Figure 7.** (a) Statistical occurrence of warm plasma cloak observed from ISEE-1, June 1978 – December  
 649 1980, in the 1 – 100 eV energy range. Adapted from Nagai et al. (1983). (b) Polar statistical (March 2001  
 650 – March 2002) observations of the warm plasma cloak (bidirectional field aligned ion jets of less than  
 651 400 eV). The occurrence is larger than 70% in the dawn side, for L-Shells of 10 – 12, i.e., the region  
 652 where the magnetopause is located. Adapted from Chappell et al. (2008).

653 Lee et al. (2016) used Cluster data in the 2007 – 2009 period, to infer the occurrence and density of both  
 654 the plasmaspheric plume and the WPC near the magnetopause. They looked individually at each of the  
 655 442 magnetopause crossings of Cluster 3 spacecraft, and searched for fluxes  $>10^5$  keV/(cm<sup>2</sup> s sr keV)  
 656 lasting at least 2 min, in the energy range 10 – 1000 eV). Plasmaspheric material may be  
 657 underestimated, as in Chen and Moore (2006), because it often has energies below 10 eV, the  
 658 instrument threshold. They distinguish between the two populations based on the pitch angle of the  
 659 ions. The WPC typically exhibits field-aligned bidirectional jets, while the plasmaspheric material is  
 660 observed at pitch angles perpendicular to the magnetic field (owing to drift motion). Plasmaspheric  
 661 material was found in the dusk sector near the magnetopause for 41 events out of 221 crossings, i.e.,  
 662 19%. This number is lower than for other studies probably due to non-detections of cases with total  
 663 energies below 10 eV. With regards to the WPC, they find for the dawn sector 17 events out 221  
 664 featuring bidirectional jets for more than 2 min, corresponding to 8% occurrence. This value is again  
 665 lower than previous estimates by Nagai et al. (1983) and Chappell et al. (2008), and the reason is that  
 666 their threshold requirements for density and duration for considering detection were more restrictive  
 667 for this study. They estimate a median density of 5.4 cm<sup>-3</sup> for plasmasphere-originating ions, and a  
 668 median density of 5.2 cm<sup>-3</sup> for the WPC, indicating that they captured only very dense events.

### 669 3.2.2 Studies based on in-situ, mass-resolving, ion detectors

670 Some ion detectors measure the time of flight inside the instrument, allowing to discriminate their  
 671 mass. Fuselier et al. (2017, 2019a) statistically analyzed the properties of the plasmaspheric material and  
 672 the WPC in the dayside magnetosphere, using roughly 5 months of MMS data between September 2015  
 673 and March 2015. In their approach, they looked for observations with H<sup>+</sup> density above 1.5 cm<sup>-3</sup> in the

674 dayside magnetosphere (i.e., plasmaspheric plumes and dense WPC), at distances  $> 7 R_E$ , and within 1.5  
 675 h in time from the magnetopause crossing. They exclude the magnetosheath and the low-latitude  
 676 boundary layer by imposing the requirement that no significant  $\text{He}^{++}$  is present. They distinguished the  
 677 origin of the population depending on the relative amounts of heavy ( $\text{He}^+$  and  $\text{O}^+$ ) ions, which are  
 678 measured by the Hot Plasma Composition Analyzer (Young et al., 2016). They found that WPC intervals  
 679 have  $n_{\text{He}^+}/n_{\text{O}^+} < 1$  and plume intervals have  $n_{\text{He}^+}/n_{\text{O}^+} > 1$ . Outflow from the high-latitude ionosphere is  
 680 dominated by  $\text{O}^+$  with much less  $\text{He}^+$  (e.g., Collin et al., 1988); thus, it stands to reason that the WPC is  
 681 distinguishable from the plume by its  $\text{O}^+$  content. Since their observations rely on particle instruments,  
 682 they cannot measure populations with total energy below the spacecraft potential (several eV to few  
 683 tens of eV). Most of the plume observations occurred in the LLBL, where the convection flows are large  
 684 and the cold plume can reach energies above the spacecraft potential and be observed by HPCA.  
 685 Overall, they find that ionospheric  $\text{H}^+$  with number density  $> 1.5 \text{ cm}^{-3}$  was detected by HPCA  $\sim 14\%$  of  
 686 the time in the magnetospheric side of the magnetopause, 10% for the WPC and 4% for the plume  
 687 populations. This study shows the lowest occurrence percentages, with findings similar to those in Lee  
 688 et al. (2016). Their lower occurrences may be explained by the threshold density imposed (WPC) and the  
 689 hidden plume at energies below the spacecraft potential.

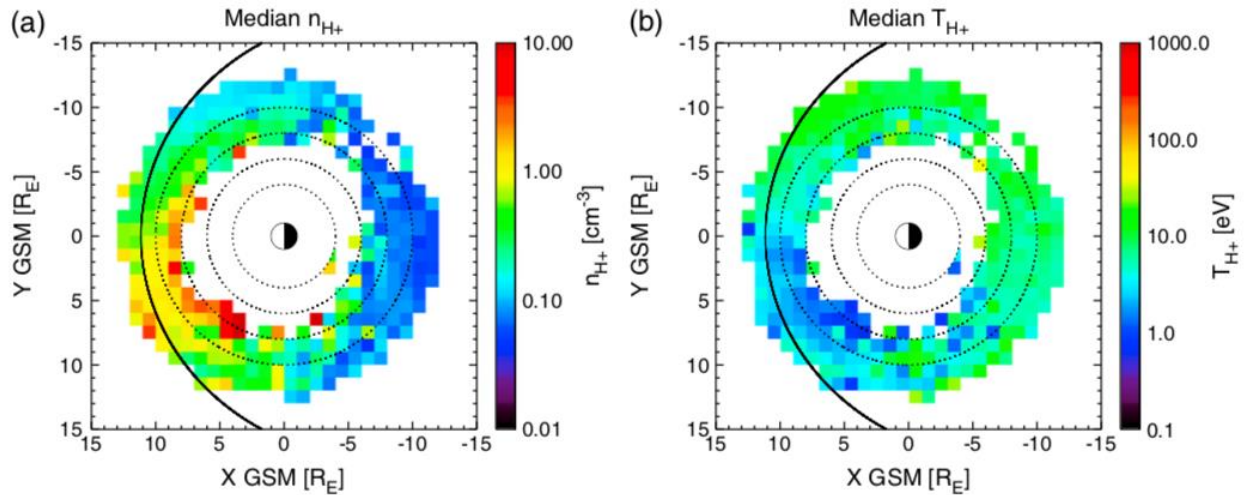
### 690 3.2.3 Studies using specific techniques aimed for cold ion detection

691 Walsh et al. (2013) examined all magnetopause crossings by the THEMIS constellation (equatorial orbit)  
 692 during the years 2008 – 2010 and searched for dense plasmaspheric plumes on the magnetospheric  
 693 side. Their criteria were that the total density was larger than twice the plasmasphere density expected  
 694 from a plasmaspheric model (Sheeley et al. 2001) inside the magnetosphere. The threshold for  
 695 considering plume detection at  $10 R_E$  was  $3.8 \text{ cm}^{-3}$  and therefore looked only for high-density plumes.  
 696 The density was inferred from the average spacecraft potential, during 2 min of observations in the  
 697 magnetosphere adjacent to the crossing. In principle, inferring the density from the spacecraft potential  
 698 has the advantage of accounting for typically ‘hidden’ low-energy ions, but this method has to be  
 699 carefully calibrated by comparing with other observations (cf. Section 3.1). They found that 137 out of  
 700 520 crossings (26%) contained the high-density plasmaspheric plume adjacent to the magnetopause in  
 701 the dusk sector, with most densities greater than  $5 \text{ cm}^{-3}$  and up to more than  $100 \text{ cm}^{-3}$ .

702 Lee and Angelopoulos (2014) used  $\sim 5$  years of data (January 2008 – May 2013) from 3 spacecraft of the  
 703 THEMIS constellation to infer the statistics of cold ions. Their observations are also based on the ion  
 704 detector onboard the spacecraft, which cannot detect cold ions with total energy below the equivalent  
 705 spacecraft potential ( $\sim 10 \text{ eV}$ ). To account for that, they normalize their dwell times to the times when  $E$   
 706  $\times \mathbf{B}$  energy exceeds the spacecraft potential, i.e. the times where the bulk drift energy exceeds the  
 707 equivalent spacecraft potential. By using this normalization, they ensure that their occurrence rates are  
 708 not biased by hidden, low-energy, plasmasphere material. They search for ions in the 5 – 120 eV range,  
 709 and impose that the number density measured by the ion detector and using the spacecraft potential  
 710 match within a factor of 2. They find that cold ions are most frequently seen in the late morning and  
 711 afternoon sector, i.e. the drainage region, with relative occurrences of 60 – 90 %. They also found  
 712 dependence with  $Kp$  index, an index that accounts for the level of geomagnetic disturbance at the  
 713 magnetosphere, with cold ions being more spread along all Magnetic Local Times (MLT) for  $Kp < 1$ , and  
 714 more concentrated in the late morning to afternoon sector for  $Kp > 1$ . Figure 8 shows the median  
 715 density and temperature of  $\text{H}^+$ . The densities are typically  $> 1 \text{ cm}^{-3}$  in the drainage region and  $< 1 \text{ cm}^{-3}$   
 716 in the other dayside regions. Typical temperatures are always below 50 eV. The ion instrument onboard  
 717 the THEMIS spacecraft cannot directly resolve the mass of ions. However, if the ions experience flows, it  
 718 is possible, under certain assumptions, to gain information on the multiple ion populations. For  $\text{He}^+$ ,  
 719 they found that the median number density ratio  $n_{\text{He}^+}/n_{\text{H}^+} < 0.1$  in the dusk sector, and  $\sim 0.5$  in the dawn

720 sector. For O<sup>+</sup>, they found roughly the same median ratios in the dayside, i.e.,  $n_{O^+}/n_{H^+} < 0.1$  in the dusk  
 721 sector, and  $\sim 0.5$  in the dawn sector. In their heavy ion calculations, they exclude detections with total  
 722 energies  $> 1$  keV.

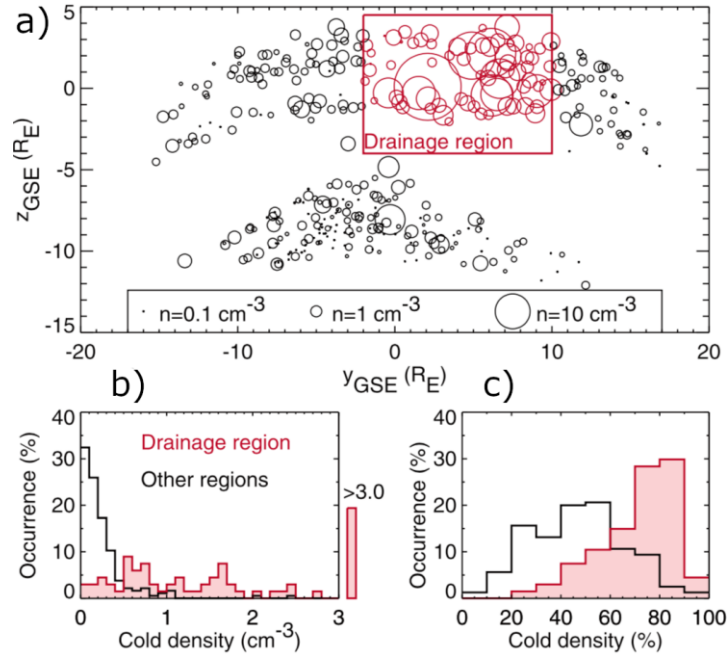
723



724

725 **Figure 8.** Median cold ( $< 120$  eV)  $H^+$  (a) density and (b) temperature, obtained from 5 years of THEMIS  
 726 data using 3 spacecraft. Adapted from Lee and Angelopoulos (2014).

727 André and Cully (2012) studied the statistical occurrence and characteristics of the cold ion component  
 728 (below a few tens of eV) in various regions of the Earth's magnetosphere using data from the Cluster  
 729 spacecraft (polar orbit), obtained during the period November 2006 to July 2009. They combined  
 730 various techniques for assessing the occurrence and density of the cold ions: direct measurements by  
 731 the ion detectors, inferred from the plasma frequency, inferred from the spacecraft potential, and using  
 732 the wake method, cf section 3.1 (Engwall et al. 2009). Figure 9 summarizes their statistics on cold ion  
 733 detections at the magnetopause. Panel a shows the location in the YZ GSE plane and the respective cold  
 734 ion density for each of the 370 Cluster 3 magnetopause crossings analyzed. The drainage region (red)  
 735 corresponds to the region where the plasmaspheric plumes are most likely to hit the magnetopause.  
 736 Figure 9b indicates that the inside the drainage region,  $\sim 20\%$  of the crossings showed cold ion densities  
 737 higher than  $3 cm^{-3}$ . Outside the drainage region, typical cold ion densities are usually below  $1 cm^{-3}$ .  
 738 These densities are obtained by subtracting the observed density by the ion detector (corresponding to  
 739 hot ions) to the total electron density ( $n$ ) inferred from the cutoff plasma frequency ( $\omega_p = ne^2/\epsilon_0 m$ ),  
 740 where  $e$  and  $m$  are the electron charge and mass, respectively. Finally, in Figure 9c a histogram of the  
 741 relative occurrence of cold ions present in the magnetopause is shown. Cold ions contribute a significant  
 742 fraction of the total number density ( $>40\%$ ) during more than 85% of the time inside the drainage  
 743 region, and 50 - 70% of the time in other regions of the dayside magnetopause.



744

745 **Figure 9.** Statistics of cold ionospheric-originating ions at the magnetopause from Cluster data. (a) Cold  
 746 ion density and location for each of the 370 magnetopause crossings identified during November 2006  
 747 to July 2009. The plasmaspheric drainage plume region is identified in red. (b) Histograms of cold ion  
 748 density in the drainage region (red) and other regions (black) of the magnetopause. (c) Histograms of  
 749 the fraction of the ion population not visible to the ion instrument in drainage (red) and other (black)  
 750 regions. Low-energy ions contribute a significant fraction of the density nearly all of the time (>85%) in  
 751 the drainage region, and 50–70% of the time outside of that region. Adapted from André and Cully  
 752 (2012).

### 753 3.2.4 Remote imaging of $\text{He}^+$

754 Spasojevic and Sandel (2010) used a different technique to infer the total ion escape via plasmaspheric  
 755 plumes. They used the Extreme Ultraviolet (EUV) imager instrument onboard the IMAGE mission (Sandel  
 756 et al. 2003), which is capable of imaging ( $0.1 R_E$  resolution) the amount of  $\text{He}^+$ , by resolving its resonance  
 757 line emission at 30.4 nm. They looked at 5 independent moderate disturbance events (Sym-H above -  
 758 100 nT), and found that the average loss rate to the dayside magnetopause was of  $\sim 0.38 - 2.1 \times 10^{27}$   
 759 ions/s during the events, i.e., somewhat higher than the results by Borovsky and Denton (2008). They  
 760 assumed a number density ratio  $n_{\text{He}^+}/n_{\text{H}^+} \sim 0.05 - 0.15$  (Craven et al. 1997) at L-shell distances 2 - 5, and  
 761 that on average 65% of the depleted  $\text{He}^+$  ions finally escape towards the dayside magnetopause.  
 762 Assuming an effective area of the drainage plume region of  $\sim 9 \times 12 R_E$ , and an average outflow velocity  
 763 of  $\sim 15 \text{ km/s}$ , the resulting ionospheric average density at the magnetopause in the drainage region  
 764 corresponds to  $6 - 32 \text{ cm}^{-3}$  during the plume events according to the results by Spasojevic and Sandel  
 765 (2010), i.e., a factor 2 – 10 larger than for the estimations of Borovsky and Denton (2008). This  
 766 discrepancy may be explained by the fact that the imaging method requires a minimum amount of  $\text{He}^+$   
 767 density in the integrated line of sight of the instrument, which would result in only detecting high-  
 768 density plumes.

769

### 770 3.2.5 Comparison between studies

771 We summarize, in Table 1, the statistics provided by the works described above, at the subsolar-to-dusk  
772 magnetopause (drainage region) and the subsolar-to-dawn magnetopause. Comparing the statistical  
773 studies presented in this section is not an easy task, owing to their different orbits, methods and criteria  
774 for cold ion detection. Nonetheless, several conclusions are drawn from Table 1.

775 Near the dayside magnetopause there are cold to warm (eV to few hundred eV) ions of ionospheric  
776 origin most of the time. These ions have approximately the same density, i.e., a few times  $0.1 \text{ cm}^{-3}$ , as  
777 keV magnetospheric ions (originally from the solar wind and the ionosphere). Cold ions in the dusk  
778 sector (drainage region) are found more frequently than in the dawn sector, and their density is higher.  
779 This is because the plasmaspheric material usually reaches the magnetopause in the dusk sector. By  
780 contrast, the WPC can be found in both sectors (Lee et al., 2016, Fuselier et al. 2017, 2019a).

		Density threshold for selection ( $\text{cm}^{-3}$ )	Relative occurrence (%)	Mean $n_{\text{H}^+}$ Observed ( $\text{cm}^{-3}$ )	Energy range (eV)	Observed $n_{\text{He}^+}/n_{\text{H}^+}$	Observed $n_{\text{O}^+}/n_{\text{H}^+}$
Dusk-side magnetopause	Chappell (1974)	~6 at L = 9 (decreasing with distance)	Convection dependent	6 – 310 (peak values)	Few <sup>(a)</sup> - few tens	0.1	-
	Chen and Moore (2006)	-	> 50	-	Few <sup>(a)</sup> – 400	-	-
	Borovsky and Denton (2008)	-	Whenever storm occurs	~ 3 (extrapolated to 10 $R_E$ )	-	-	-
	Lee et al (2016)	Flux >10 <sup>5</sup> keV/cm <sup>2</sup> s sr keV	19	5.4	10 <sup>(a)</sup> – 1000	-	-
	Fuselier et al. (2017)	1.5	4	5	Few <sup>(a)</sup> - several thousands	0.015 (assumed at L = ~10)	< 0.015
	Walsh et al. (2013)	~5.7 at L = 9 (decreasing with distance)	26 (high-density plumes)	> 5 - 10	-	-	-
	Lee and Angelopoulos (2014)	-	70 - 95	> 1	5 <sup>(a)</sup> - 120	< 0.1	< 0.1
	André and Cully (2012)	-	> 85 including 20	> 0.2 - 1 > 3	up to few tens	-	-
	Spasojevic and Sandel (2010)	-	Disturbed times considered	6 – 32 (extrapolated to 10 $R_E$ )	-	0.05 – 0.15 (assumed at L = 2 - 5)	-
Dawn-side magnetopause	Nagai et al. (1983)	-	> 50	-	10 <sup>(a)</sup> - 100	-	-
	Chappell et al. (2008)	-	>70	0.5 - 3	10 <sup>(a)</sup> - 400	-	-
	Lee et al. (2016)	Flux >10 <sup>5</sup> keV/cm <sup>2</sup> s sr keV	8	5.2	10 <sup>(a)</sup> – 1000	-	-
	Fuselier et al. (2017, 2019a)	1.5	10	3	Few <sup>(a)</sup> -several thousands	< 0.02	~0.02/0.04
	Lee and Angelopoulos (2014)	-	30 – 70	0.15 – 0.7	5 <sup>(a)</sup> - 120	~0.5	~0.5
	André and Cully (2012)	-	50 - 70	0.1 - 1	up to few tens	-	-

781 **Table 1.** Studies of ionospheric-originating ions near the Earth's magnetopause. The dusk side  
782 corresponds roughly to 12 - 18 LT, and the dawn side roughly to 06 – 12 UT.

783 *(a) The real lower energy threshold is defined by the spacecraft potential, which is variable depending on*  
784 *spacecraft and plasma conditions, in the range of few eV to tens of eV.*

### 785 **3.2.5.1 Dusk side**

786 The reported percent of time that plasmaspheric material is observed at the magnetopause, has a large  
787 variability in the literature. Except for Fuselier et al. (2017), the studies suggest that this number is >20 –  
788 25 % of the time, and some indicate that the percent is > 70 - 80%. This variation is mainly due to the  
789 following factors: the density threshold imposed for considering a detection, and the minimum energy  
790 that the method can detect. Different studies impose a more or less restrictive density threshold for  
791 considering detection of cold ions, which range from being above the noise of the method (typically less  
792 than 1 tenth  $\text{cm}^{-3}$ ), e.g., André and Cully (2012), Lee and Angelopoulos (2014), to more than  $5.7 \text{ cm}^{-3}$  for  
793 Walsh et al (2013). The second important factor is that for most of the studies, the plasmaspheric  
794 material can go undetected for a significant fraction of the time, because their methods do not allow to  
795 detect cold ions with total energy below the spacecraft potential. Only three studies tackle this  
796 shortcoming. André and Cully (2012) uses various indirect techniques that can detect ions below  $V_{sc}$ .  
797 They find that cold ions are present > 85%, with  $n_{H^+} \sim 0.2 - 1 \text{ cm}^{-3}$ , including a smaller fraction of time  
798 ( $\sim 20\%$ ) when the cold ion number density is >  $3 \text{ cm}^{-3}$  (plumes). Lee and Angelopoulos (2014) only  
799 consider times when the convection speed is larger than the spacecraft potential, and therefore the cold  
800 ions will be detected if they are present. They find occurrence times (70 – 95%) in accordance to André  
801 and Cully (2012), with similar density estimates ( $> 1 \text{ cm}^{-3}$ ). The other study that can detect ions below  
802 the spacecraft potential is Walsh et al. (2013), because it relies on estimating density from the  
803 spacecraft potential measurement rather than from particle measurements. However, they search only  
804 for high-density plumes, and impose density thresholds of  $\sim 5 \text{ cm}^{-3}$  (varying with radial distance to Earth).  
805 They find an occurrence probability of 26% and average densities of  $5 - 10 \text{ cm}^{-3}$ . Based on these results,  
806 we note that studies relying on particle detectors cannot provide accurate occurrence probabilities,  
807 because the cold ions often do not reach the detectors due to the positive spacecraft potential.

808 We conclude that cold ions are present at the dusk magnetopause > 80% of the time, with average  $H^+$   
809 densities of at least a few times  $0.1 \text{ cm}^{-3}$ . This includes 20 – 25 % of the time when the density is >  $3 \text{ cm}^{-3}$ .  
810 Periods of high density in the dusk region are often due to parts of the bulge region of the  
811 plasmasphere exiting and being sunward convected to the magnetopause, i.e., the so-called plumes.  
812 Plumes occur predominantly during storm times and up to few days later, while the lower density cold  
813 ions can come from various mechanisms, including the WPC, high-latitude outflows, the plasmaspheric  
814 trough and plasmaspheric wind.

815 It is difficult to draw significant conclusions from the composition measurements of ionospheric-  
816 originating ions near the magnetopause. There are too few studies using composition to determine if,  
817 for example, there is a composition change in the plume with L-shell.

### 818 **3.2.5.2 Dawn side**

819 With respect to the dawn sector, which is mainly affected by the warm plasma cloak and high-latitude  
820 outflows, Table 1 reveals that the studies provide different results depending mainly on the density  
821 threshold they imposed for the definition of cold ions. Lee et al. (2016) and Fuselier et al. (2017) were  
822 more restrictive, and therefore their results reflect the statistics of the high-density events. The WPC can  
823 be identified by its field aligned, bi-directional ion flows. Furthermore, it is more easily detected by  
824 particle instruments than the plasmaspheric material, owing to its larger total energy, and hence the

825 better agreement between studies than for the dusk side. Chappell et al. (2008) finds somewhat larger  
 826 occurrences (>70%) and densities ( $0.5 - 3 \text{ cm}^{-3}$ ) than Nagai et al. (1983), Lee and Angelopoulos (2014),  
 827 and André and Cully (2012). This is probably related to the higher upper energy limit they use (400 eV).  
 828 The WPC can be often be found at energies >100 eV, and these events would be missed by the other  
 829 studies. In addition, the ion detector used by Chappell et al. (2008) has a larger geometrical factor,  
 830 because it was specifically designed to measure cold to warm ion populations (few eV – 400 eV).

831 For the dawn side, we conclude that the probability of finding the WPC at the magnetopause in the  
 832 dawn side is > 50% – 70%, with average  $\text{H}^+$  densities of few tenths of  $\text{cm}^{-3}$  to few  $\text{cm}^{-3}$ . For ~10% of the  
 833 time, the average  $\text{H}^+$  density is  $\geq 3 \text{ cm}^{-3}$ . Similar to the duskside studies, there are too few studies using  
 834 composition to investigate composition differences with L-shell or local time.

### 835 **3.2.6 Relative importance of ionospheric-originating ions at the dayside magnetopause**

836 The other population that is always present on the magnetospheric side of the Earth's magnetopause is  
 837 made of the plasma sheet ions, with energies in the keV to tens of keV range and densities of few tenths  
 838 of  $\text{cm}^{-3}$ . The origin of this population is both the solar wind and the ionosphere (e.g., Huddleston et al.,  
 839 2005). For the dusk-side magnetopause, more than 80% of the time the density of cold ions is of the  
 840 same order of magnitude as hot magnetospheric ions. The cold ion density is one order of magnitude  
 841 larger than hot magnetospheric ions 20% – 25% of the time. For the dawn-side magnetopause, the  
 842 density of cold ions is of the same order of magnitude as hot magnetospheric ions > 50% - 70% of the  
 843 time. For 10% of the time, the cold ion density is one order of magnitude larger than hot  
 844 magnetospheric ions. Finally, on average, the plume (20% - 25% of the time) and high-density WPC  
 845 events (10% of the time) have number densities which are still ~one order of magnitude lower than the  
 846 magnetosheath (shocked solar wind) density, which is found at the other side of the magnetopause.

### 847 **3.3 Quantification of ionospheric-originating ions in the Earth's magnetotail**

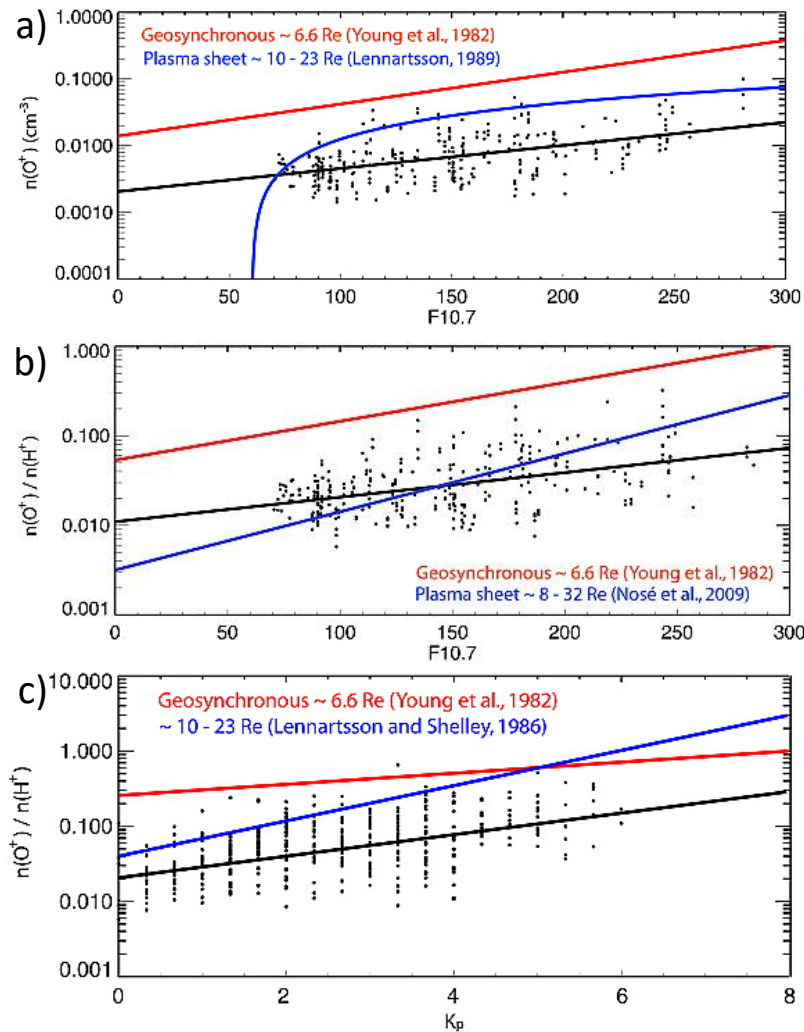
848 The other main region where magnetic reconnection takes place is the Earth's magnetotail, which is  
 849 divided into two main regions: the plasma sheet, a relatively thin layer (~6  $R_E$  thick on average,  
 850 depending on distance from Earth) which lies in the geomagnetic equatorial plane, and the lobes, i.e.  
 851 the regions that fill the space above and below the plasma sheet (see Figure 1). The particle populations  
 852 in these regions of the magnetotail are quite different. As magnetotail reconnection onset occurs in the  
 853 plasma sheet, its properties are important for controlling the initiation of reconnection. But once all the  
 854 plasma sheet material has reconnected, the lobes field lines are also brought into the reconnection  
 855 region and become the inflow material of the reconnection process. Therefore, plasma conditions on  
 856 lobe field lines are also important. We now examine the ionospheric contributions to the plasma  
 857 composition of the plasma sheet and the lobes.

#### 858 **3.3.1 Plasma Sheet**

859 The plasma sheet ion population is typically hot, and has temperatures in the range of few keV to few  
 860 tens of keV. The ionospheric contribution to the plasma sheet is best determined by its composition,  
 861 because ionospheric-originating ions have generally been energized and thermalized together with ions  
 862 of solar wind origin through various processes in the magnetotail. Since both the ionospheric outflows  
 863 and the solar wind contain significant  $\text{H}^+$ , they mix in the plasma sheet and their origin is thus difficult to  
 864 discern once energized. However,  $\text{O}^+$  can only come from the ionosphere, and so is often used as a  
 865 tracer for the ionospheric source.  $\text{He}^{++}$  in the plasma sheet is dominantly of solar wind origin, and high  
 866 charge state CNO species, such as  $\text{O}^{+6}$  are definitely of solar wind origin, and so these can be used to  
 867 trace the solar wind component. Lennartsson and Sharp (1985) used the energy distributions of the  $\text{He}^{++}$   
 868 and  $\text{O}^+$ , compared to the  $\text{H}^+$  to estimate the fraction of  $\text{H}^+$  from the ionosphere, and concluded that the

869 ionosphere may contribute 30%, even during quiet times. Gloeckler and Hamilton (1987) used  
870 measurements from the AMPTE mission to estimate the ionospheric contribution through comparisons  
871 of the plasma sheet composition with average solar wind composition, and concluded that the  
872 ionospheric contribution to the plasma sheet at 15  $R_E$  was 36% during quiet times and 65% during active  
873 times. However, these averages do not capture the variability of the ionospheric contribution with both  
874 solar EUV and geomagnetic activity.

875 Statistical studies of the mid-tail (distances of 10 - 30  $R_E$ ) plasma sheet meant to capture this variability  
876 have been performed using data from the ISEE satellites, Geotail, AMPTE and Cluster. Lennartsson and  
877 Shelley (1986) and Lennartsson (1989) performed a statistical study of the plasma sheet ion composition  
878 using the Plasma Composition Experiment on ISEE 1, covering energies from 0.1 - 16 keV/e and radial  
879 distances from 10 - 23  $R_E$ , during the rise of solar cycle 21, i.e., 1978 and 1979. They compared their  
880 observations to geomagnetic activity using the Auroral Electrojet (*AE*) index, which measures the  
881 perturbations of the magnetic field in the auroral regions typically associated to substorm activity. They  
882 found a strong increase in the  $O^+/H^+$  density ratio with increasing *AE*, from 0.01 at low *AE* up to 0.6 at *AE*  
883 of 1000 nT. This increase was predominantly due to an increase in the  $O^+$  density by a factor of 10, from  
884  $0.02 \text{ cm}^{-3}$  to  $0.2 \text{ cm}^{-3}$ . They also showed a distinct increase with solar EUV, with an increase of the  $O^+$   
885 density from  $0.02 \text{ cm}^{-3}$  to  $0.08 \text{ cm}^{-3}$  when the solar radio flux at 10.7 cm wavelength (F10.7 index, an  
886 excellent proxy for solar activity), increase from 50 sfu to >200 sfu. Baumjohann et al. (1989) reported  
887 ion number densities for the plasma sheet at 9 - 14  $R_E$  using AMPTE and found values consistent with  
888 Lennartsson (1989). Nose et al. (2009) used 16 years of data from the STICS instrument on Geotail  
889 (Energy range 9 - 212 keV) to examine the solar cycle variability. Their dataset covered a wider range of  
890 distances, from 8  $R_E$  to 100  $R_E$ . They showed clearly the increase in the  $O^+/H^+$  ratio from 0.01 to 0.06 as  
891 F10.7 increased from 70 sfu to 200 sfu. Mouikis et al. (2010) performed a statistical analysis of the  
892 densities of  $H^+$  and  $O^+$  inside the plasma sheet using a more limited range of radial distances, 15 - 19  $R_E$ ,  
893 using 5 years of data (2001 - 2005) from the CIS/CODIF instrument on the Cluster mission. The  
894 instrument operates in the range 40 eV - 40 keV. Comparing the  $O^+$  density as a function of F10.7 from  
895 Cluster with the results of Lennartsson (1989), Mouikis et al. (2010) find a similar increase with F10.7,  
896 although Lennartsson (1989) observed overall higher densities (Figure 10a). This is likely because the  
897 radial range extended to lower radial distances, where the density is higher (as will be discussed). Figure  
898 10b compares the  $O^+/H^+$  density ratio from the Cluster study as a function of F10.7 with the Nose et al.  
899 (2009) results (blue). While the ratio level is about the same, Nose et al. (2009) found a steeper slope  
900 with F10.7. This may be due to the higher energy range of the Nose study, or may be because the  
901 Geotail data accounted for all geomagnetic activity levels, while the Cluster data used are just for quiet  
902 times. Figure 10c compares the activity dependence found by the Cluster study with the results of  
903 Lennartsson and Shelley (1986) (blue). Again, the dependence is similar, but the ratio is higher in the  
904 ISEE study that covered closer radial distances. Clearly, all these studies agree that the density of  $O^+$  and  
905 the  $O^+/H^+$  density ratio increase both with solar EUV (as characterized by the F10.7 proxy), and with  
906 geomagnetic activity (characterized by *Kp* or *AE* indices) with approximately equal contributions. The  
907 solar EUV sets a baseline ratio for a given phase of the solar cycle, and then activity increases the  $O^+$   
908 content from there.



909

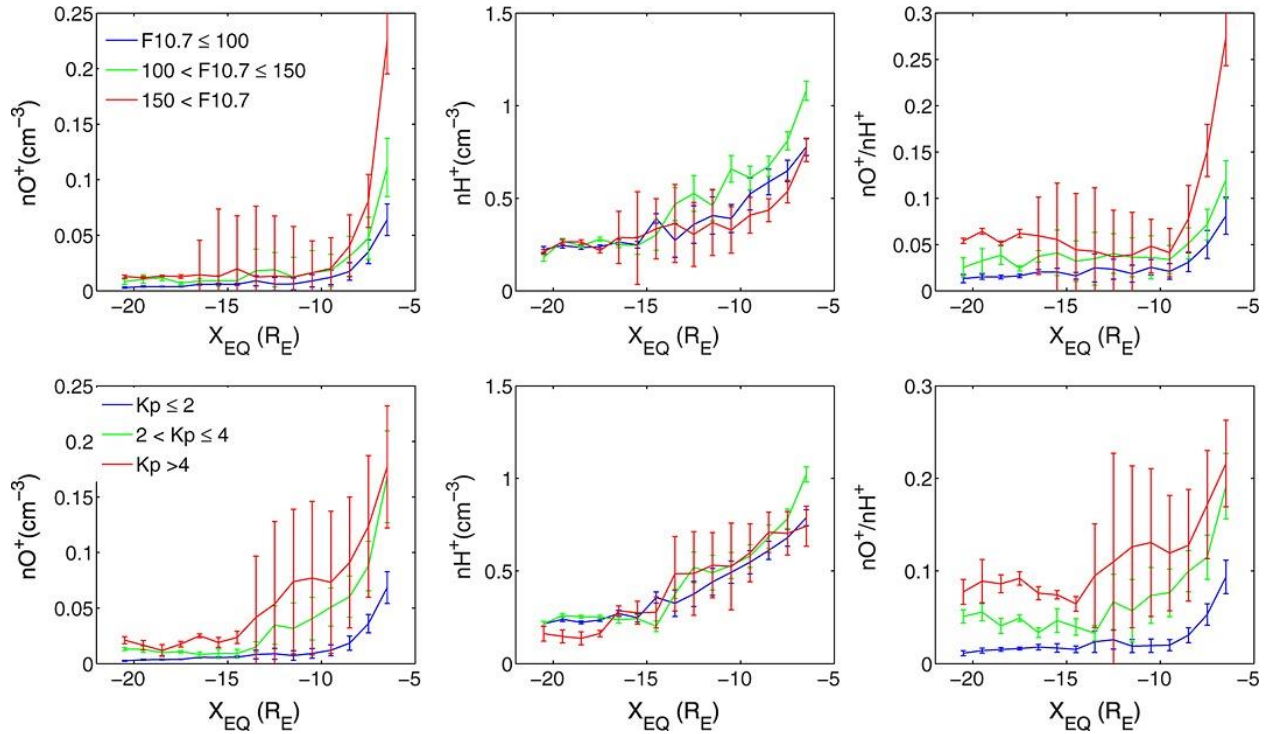
910 **Figure 10.** Variation in the  $O^+$  and  $H^+$  densities and the density ratio with a) and b) F10.7, and c)  $K_p$ .  
 911 Adapted from Moukiss et al. (2010).

912 The plasma sheet densities closer to the Earth, at  $\sim 6 - 7$ ,  $R_E$  were characterized by Young et al. (1982)  
 913 and Kistler and Moukiss (2016). Both studies cover the "hot" population, with Young et al. (1982)  
 914 covering the energy range from 0.9 - 17 keV using the GEOS data set (similar to the instrument on ISEE  
 915 1), and Kistler and Moukiss (2016) covering the energy range from 1 - 40 keV using Cluster/CODIF. While  
 916 GEOS measurements were near-equatorial, the Cluster/CODIF measurements were taken at about  $\sim 30$   
 917 degrees latitude for this L-range, so the distribution was mapped along the field line to the equator to  
 918 obtain comparable results. The  $O^+$  density and the  $O^+/H^+$  ratio in this region is about a factor of 10 higher  
 919 than in the 15 - 19  $R_E$  region, as shown by the red lines in Figure 10abc, but show similar F10.7 and  $K_p$   
 920 dependencies. As was observed further out, EUV alone will increase the  $O^+/H^+$  ratio by a factor of  $\sim 8$ ,  
 921 and then geomagnetic activity will increase it by another factor of 10.

922 Maggiolo and Kistler (2014) used the mapping technique to derive 2D maps of the  $H^+$  and  $O^+$  densities in  
 923 the X-Y equatorial plane using the Cluster/CODIF data. Figure 11 shows the densities and density ratios  
 924 as a function of the equatorial X position from this study. The  $O^+$  density and the  $O^+/H^+$  density ratios  
 925 increase strongly inside  $L = -10$ , while the  $H^+$  increases more gradually with decreasing distance. In the Y-  
 926 direction, they did not observe a strong dawn-dusk asymmetry, but found the density and density ratios

927 to be relatively flat from dawn to dusk across the magnetotail at distances of 15 - 20  $R_E$ . Closer to the  
 928 Earth, the densities peak close to midnight during quiet times, with the peak shifting downward for  
 929 higher activity. However, the  $O^+/H^+$  density ratio remains relatively uniform.

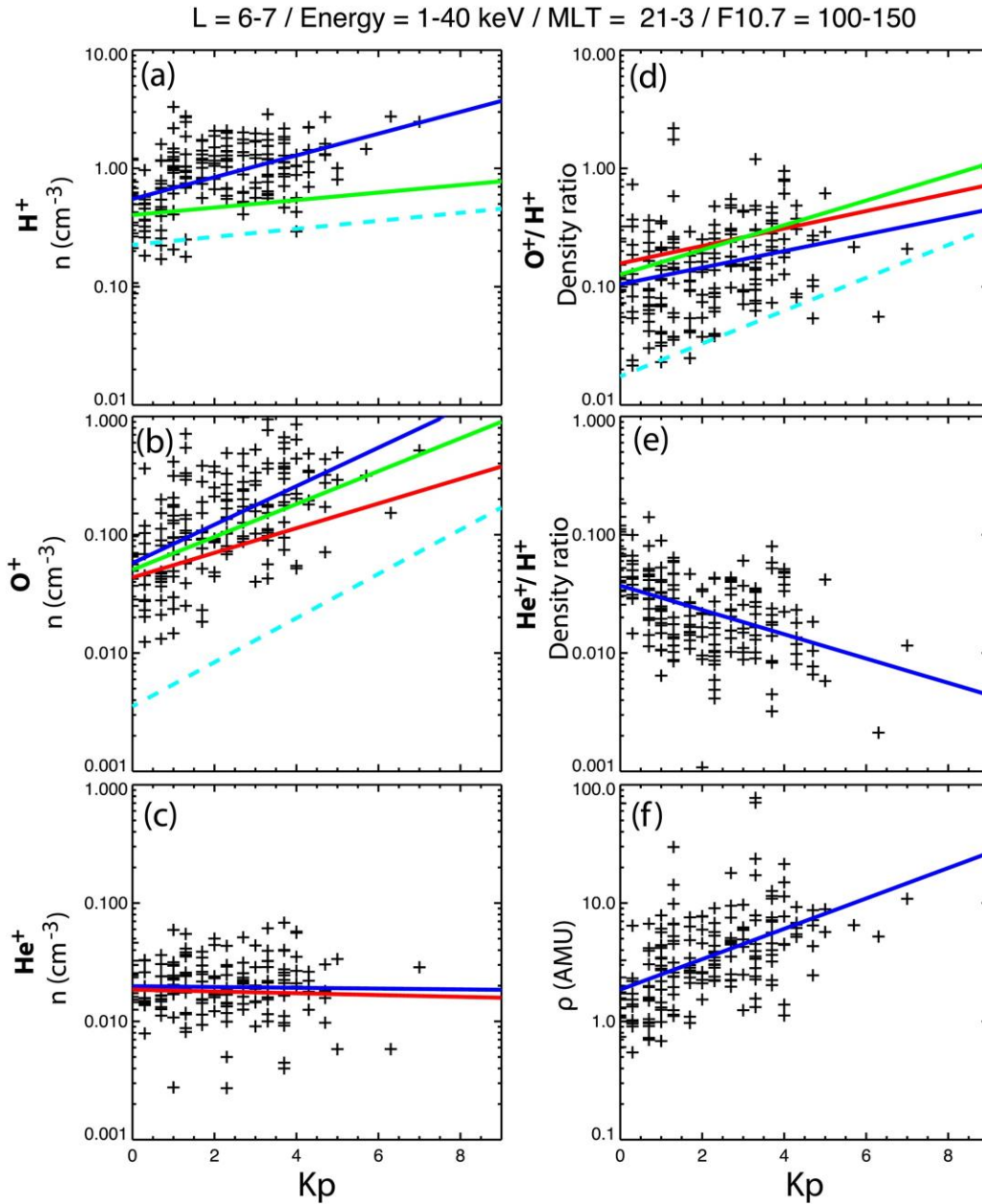
930



931

932 **Figure 11.** Radial dependence of the  $O^+$  and  $H^+$  densities in the plasma sheet, and their ratio. Adapted  
 933 from Maggiolo and Kistler (2014).

934 Figure 12, from Kistler and Moukik (2016), summarizes the  $Kp$  dependence found in the near-earth  
 935 plasma sheet from these studies. A medium range of F10.7, 100 - 150, is shown, but results for other  
 936 F10.7 values are similar. The black points are the L = 6 - 7 measurements from Kistler and Moukik  
 937 (2016), and the dark blue line is the fit to these points. The Maggiolo and Kistler (2014) fits for L = 7 - 8  
 938 are shown in green, while the Young et al. (1982) fits are in red, and the Moukik et al. (2010) results  
 939 from 15 - 19  $R_E$  are in light blue. The increase in  $O^+$  and in the  $O^+/H^+$  ratios with  $Kp$  agree very well  
 940 between the three near-Earth studies, with the 15 - 19  $R_E$  study showing lower values, as expected  
 941 because of the radial dependence. Surprisingly,  $He^+$  shows almost no variation with  $Kp$ , which leads to a  
 942 decreasing  $He^+/H^+$  ratio with  $Kp$ . The final panel shows the increase in the overall mass density with  $Kp$ .  
 943 This also increases by a factor of 10 with geomagnetic activity.



944

945 **Figure 12.** Ion composition as a function of  $Kp$ , comparing the studies of Kistler and Moukis (points, and  
 946 blue line fit), Maggiolo and Kistler (2014) (green) Young et al. (1982) (red) and Moukis et al. (2010)  
 947 (dashed light blue).

948 The studies described so far have analyzed the hot plasma sheet population, which is composed of a  
 949 mixture of heated ions of both solar wind and ionospheric origin. There is also evidence of a cold, low-  
 950 energy population of ionospheric origin in the plasma sheet, coexisting with the hot population. Seki et  
 951 al. (2003) presented observations from time periods when the Geotail spacecraft was in eclipse, which  
 952 causes the spacecraft to charge negatively. This negative potential attracts the positive cold ions, and  
 953 brings them up to an energy where they can be observed. Observations during these eclipse time  
 954 periods showed the existence of a cold population with density comparable to the hot population. This  
 955 cold ion population becomes also detectable by particle detectors when the bulk drift energy is larger  
 956 than the equivalent spacecraft potential but smaller than the thermal energy of the hot plasma sheet

957 population (e.g., Alm et al. 2018, 2019, Xu et al., 2019). André et al. (2015), using the wake method (cf.  
 958 section 3.1), conducted a statistical survey in the magnetotail and found this cold population only ~10%  
 959 of the time inside the plasma sheet. However, with their method it is difficult to detect cold ions in the  
 960 plasma sheet because to detect an extended wake, indicating the presence of cold ions, requires the  
 961 cold ion density to be at least about half of the total density, and the bulk drift energy to be less than  
 962 the equivalent spacecraft charging, both of which may often be violated in the plasma sheet. In addition,  
 963 to estimate also the cold ion flux, observations by the EDI instrument are needed, designed to operate  
 964 in a reasonably steady and strong magnetic field, also conditions often violated in the plasma sheet. Lee  
 965 and Angelopoulos (2014) also examined the number density of cold ions (energy below 1 keV) in the  
 966 near tail (distances of 6 – 12  $R_E$ ), using THEMIS observations during ~5 years of data (January 2008 – May  
 967 2013). They found occurrence rates in the night sectors varying between 5 – 35 % depending on  
 968 distance to Earth, with the largest occurrences at  $L = 4 - 6$ . They report average cold  $H^+$  densities in the  
 969 tail of  $\sim 0.05 - 0.1 \text{ cm}^{-3}$  (see Figure 8), with average temperatures of  $\sim 10 \text{ eV}$ . They also calculated the  
 970 average  $He^+$  and  $O^+$  densities and temperatures of the cold ions (below 1 keV). Interestingly, they find  
 971 higher number densities ( $\sim 0.1 \text{ cm}^{-3}$  for  $He^+$  and  $\sim 0.2 \text{ cm}^{-3}$  for  $O^+$ ) than for  $H^+$ , and also larger  
 972 temperatures ( $\sim 50 \text{ eV}$  for  $He^+$  and  $\sim 200 \text{ eV}$  for  $O^+$ ).

### 973 3.3.2 Lobes

974 Magnetic reconnection in the magnetotail occurs first in the plasma sheet, where the stretched  
 975 magnetic field lines from the North and South hemispheres form a thin current sheet. Magnetic  
 976 reconnection then proceeds with lobes field lines, above and below the plasma sheet, which are filled  
 977 only by high-latitude ionospheric outflows. These outflows either end up in the plasma sheet or are lost  
 978 in the distant tail. As discussed in section 2.2.2, ion outflow from the cusp and polar cap are accelerated  
 979 along the field line through centrifugal acceleration, and are dispersed by the velocity filter effect into  
 980 the lobes. Thus, the populations normally observed in the lobes are cold, field-aligned streams of ions.  
 981 Even if the source population has a broad energy range, the lobe population will have a narrow velocity  
 982 distribution because only a particular velocity reaches a particular location. Ion species with the same  
 983 velocity will have a different energy by their mass ratio. Thus in the 15 -20  $R_E$  region, where these cold  
 984 ions have been well-characterized by data from the Cluster mission, the lobe population consists of  
 985 protons with energies of 10's of eV (Engwall et al. 2009, André et al. 2015) while the  $O^+$  ions are in the 40  
 986 eV - 1 keV range (Liao et al. 2015). Svenes et al. (2008) inferred the electron number density indirectly  
 987 from the Cluster spacecraft potential using 7 years of data from the waning part of solar cycle 23, and  
 988 found that more than two thirds of the time the electron density,  $n_e$ , was between  $0.007 \text{ cm}^{-3}$  and  $0.092$   
 989  $\text{cm}^{-3}$ , with a mode of  $0.047 \text{ cm}^{-3}$ . These averages were independent of solar wind and geomagnetic  
 990 conditions, but for the high-density tail of the distribution ( $n_e > 0.2 \text{ cm}^{-3}$ ), a correlation with 10.7 cm  
 991 solar radio flux was present. André et al. (2015) performed an extensive study of the lobe ion population  
 992 over a solar cycle. Again the spacecraft potential was used to estimate the density and an extended  
 993 spacecraft wake was used to detect streaming cold ions and to estimate the ion flux. They find that a  
 994 cold population is present at least 64% of the time at distances of 5 - 20  $R_E$ , with average densities of 0.2  
 995 -  $0.4 \text{ cm}^{-3}$ , and average field-aligned velocities of 25 - 30 km/s. The outflow flux increases by a factor  $\sim 2$   
 996 with geomagnetic activity and with solar EUV over the solar cycle. The increase is mainly due to the  
 997 density increasing, while the velocity distribution remains about the same.  
 998 The  $O^+$  in the lobes was characterized by Liao et al. (2010, 2012, and 2015). During solar maximum, 2001  
 999 - 2002, the occurrence frequency of  $O^+$  beams in the lobes is almost 100% during storms, but even  
 1000 during non-storm times, the occurrence frequency is  $\sim 50\%$ . The location of the  $O^+$  ions in the lobes  
 1001 shows a dawn-dusk asymmetry that depends on IMF  $B_y$ . When IMF  $B_y$  is positive, the  $O^+$  in the northern  
 1002 lobe tends to be on the dawn side, while the  $O^+$  in the southern lobe tends to be on the dusk side. For  
 1003 negative  $B_y$ , the asymmetry reverses, but not as strongly. If there are different amounts of outflow in

1004 the northern and southern hemisphere, this could lead to dawn-dusk asymmetries in the plasma sheet,  
 1005 as well. The occurrence of the O<sup>+</sup> beams decreased significantly with solar cycle, with the decreases  
 1006 stronger in the tail lobes than in the polar cap. This decrease could be because the flux decreased below  
 1007 the threshold level for the instrument, or because the transport paths changed, due to changes during  
 1008 the minimum of the solar cycle, so the O<sup>+</sup> beams no longer reach the near-earth plasma sheet.

1009 The H<sup>+</sup> and O<sup>+</sup> populations in the lobes are clearly related, but a focused study comparing the two has  
 1010 not been done. Backwards modeling indicates that the proton population comes from the full range of  
 1011 the polar cap (Li et al. 2013), while the more energetic O<sup>+</sup> is thought to come from the cusp. Liao et al.  
 1012 (2015) showed that during quiet times, the O<sup>+</sup> beam fluxes observed were consistent with the outflow  
 1013 fluxes from the cusp, while during more active times, some additional acceleration of the cusp outflow  
 1014 population was required. The densities and velocities of the two populations during the solar maximum  
 1015 time period are compared in Kronberg et al., (2014). The H<sup>+</sup> density is significantly higher than the O<sup>+</sup>  
 1016 (average 0.14 cm<sup>-3</sup> for H<sup>+</sup>, versus 0.009 - 0.02 cm<sup>-3</sup> for O<sup>+</sup>). But the velocity range is similar (average 40  
 1017 km/s for H<sup>+</sup> versus 37.9 km/s for O<sup>+</sup>). Similar velocities would be expected from the velocity filter effect.

### 1018 3.3.3 Comparison between studies

1019 We summarize, in Table 2, the statistical observations of the H<sup>+</sup> number density ( $n_{H^+}$ ), H<sup>+</sup> percent of  
 1020 ionospheric origin when available, and O<sup>+</sup>/H<sup>+</sup> number density ratio ( $n_{O^+}/n_{H^+}$ ), for the various studies  
 1021 presented in the near-Earth plasma sheet (< 10 R<sub>E</sub>), distant plasma sheet (> 10 R<sub>E</sub>) and tail lobes.

1022 **Table 2.** Statistical studies of number density and plasma composition in the Earth's magnetotail.

		Distance to Earth (R <sub>E</sub> )	$n_{H^+}$ of ionospheric origin (%)	Mean $n_{H^+}$ Observed (cm <sup>-3</sup> )	Energy range (keV/e)	Observed $n_{O^+}/n_{H^+}$
Near-Earth Plasma sheet	<i>Young et al. (1982)</i>	6 - 7	-	0.3 - 0.4 <sup>b</sup> (Kp < 3) 0.4 - 0.5 <sup>b</sup> (3 < Kp < 6) 0.5 - 0.6 <sup>b</sup> (Kp > 6)	0.9 - 16	0.4 - 0.5 <sup>b</sup> (Kp < 3) 0.5 - 0.9 <sup>b</sup> (3 < Kp < 6) 0.9 - 1.4 <sup>b</sup> (Kp > 6)
	<i>Gloecker and Hamilton (1987)</i>	8 - 9	47	-	1.5 - 315	0.11 <sup>a</sup>
	<i>Lennartson (1989)</i>	< 10	-	0.8 <sup>b</sup> (F10.7 < 100) 0.68 <sup>b</sup> (100 < F10.7 < 150) 0.62 <sup>b</sup> (150 < F10.7 < 200) 0.58 <sup>b</sup> (F10.7 > 200)	0.1 - 16	0.1 <sup>b</sup> (F10.7 < 100) - - -
	<i>Lee and Angelopoulos (2014)</i>	5 - 10	-	< 0.1 <sup>d</sup>	< 1	> 1 <sup>d</sup>
	<i>Maggiolo and Kistler (2014)<sup>c</sup></i>	7 - 8	-	0.4 - 0.5 <sup>b</sup> (Kp < 3) 0.5 - 0.7 <sup>b</sup> (3 < Kp < 6) 0.7 - 0.8 <sup>b</sup> (Kp > 6)	1 - 40	0.2 - 0.3 <sup>b</sup> (Kp < 3) 0.3 - 0.6 <sup>b</sup> (3 < Kp < 6) 0.6 - 1.3 <sup>b</sup> (Kp > 6)
	<i>Kistler and Mouikis (2016)<sup>c</sup></i>	6 - 7	-	0.6 - 0.8 <sup>b</sup> (Kp < 2) 0.8 - 1.3 <sup>b</sup> (2 < Kp < 4) > 1.3 <sup>b</sup> (Kp > 4)		0.1 <sup>b</sup> (Kp < 2) 0.1 - 0.2 <sup>b</sup> (2 < Kp < 4) 0.2 - 0.5 <sup>b</sup> (Kp > 4)
Distant Plasma sheet	<i>Lennartson and Sharp (1985)</i>	10 - 23	20-30(AE < 100)	-	0.1 - 16	< 0.1 (AE < 100 nT) 0.2 - 0.7 (AE > 300 nT)
	<i>Lennartson and Shelley (1986)</i>	10 - 23	-	0.5 - 1 <sup>b</sup> (AE < 100) 0.2 - 0.3 <sup>b</sup> (AE > 700)		0.01 - 0.08 <sup>b</sup> (AE < 100 nT) 0.6 <sup>b</sup> (AE > 700 nT)

	<i>Gloecker and Hamilton (1987)</i>	15	37 (quiet) 65 (disturbed)	-	28 - 226	0.09 <sup>a</sup> 0.17 <sup>a</sup>	(quiet) (disturbed)
	<i>Baumjohann et al. (1989)</i>	9 - 14	-	0.5 (AE < 100) 0.4 (AE > 100)	0.02 - 40	-	-
	<i>Lennartson (1989)</i>	> 10	-	0.65 <sup>b</sup> (F10.7 < 100) 0.55 <sup>b</sup> (100 < F10.7 < 150) 0.4 <sup>b</sup> (150 < F10.7 < 200) 0.48 <sup>b</sup> (F10.7 > 200)	0.1 - 16	0.03 <sup>b</sup> (F10.7 < 100) 0.05 <sup>b</sup> (100 < F10.7 < 150) 0.15 <sup>b</sup> (150 < F10.7 < 200) 0.15 <sup>b</sup> (F10.7 > 200)	
	<i>Seki et al. (2003)</i>	9 - 18	~50 <sup>d</sup>	~0.2 <sup>d</sup>	< 1	< 0.5 <sup>d</sup>	
	<i>Mouikis et al. (2010)</i>	15 - 19	-	0.2 - 0.3 <sup>b</sup>	1 - 40	0.01 - 0.07 <sup>b</sup>	
	<i>Maggiolo and Kistler (2014)<sup>c</sup></i>	15 - 20	-	~0.3 <sup>b</sup>		0.01 - 0.05 <sup>b</sup> (Kp < 3) 0.05 - 0.2 <sup>b</sup> (3 < Kp < 6) 0.2 - 0.7 <sup>b</sup> (Kp > 6)	
Tail lobes	<i>Svenes et al. (2008)</i>	5 - 19	>90% <sup>f</sup>	0.047	N/A <sup>e</sup>	-	
	<i>André et al. (2015)</i>	5 - 10		~0.25 (Kp < 3) 0.3 - 0.7 (Kp > 3)	Up to tens of eV	-	
		10 - 15		0.1 - 0.2 (Kp < 3) 0.2 - 0.3 (Kp > 3)			
		15 - 20		<0.1 (Kp < 3) 0.1 - 0.2 (Kp > 3)			

1023 <sup>a</sup> Considers  $n_{H^+}$  of ionospheric origin only.

1024 <sup>b</sup> Considers total  $n_{H^+}$ , ionospheric plus solar wind origin.

1025 <sup>c</sup> The values reported in the table consider F10.7 = 100 - 150 sfu.

1026 <sup>d</sup> Accounts only for cold  $n_{H^+}$ .

1027 <sup>e</sup> The ion number density is inferred indirectly from the SC potential.

1028 <sup>f</sup> Plasma in the lobes is almost entirely of ionospheric origin, although the studies presented do not  
1029 attempt to quantify the origin.

1030

### 1031 3.3.3.1 Near-Earth Plasma Sheet (< 10 R<sub>E</sub>)

1032 The H<sup>+</sup> number density in the near-Earth plasma sheet (less than 10 R<sub>E</sub> from Earth) depends mainly on  
1033 the distance to Earth and geomagnetic activity, and to a lesser degree on solar EUV. It is estimated that  
1034 roughly half of H<sup>+</sup> ions are of ionospheric origin (Gloecker and Hamilton, 1989). For ions with total  
1035 energies above 1 keV,  $n_{H^+} \sim 0.3 - 0.8 \text{ cm}^{-3}$  for quiet magnetospheric conditions (Kp < 3), and  $n_{H^+} \sim 0.4 -$   
1036  $1.3 \text{ cm}^{-3}$  for disturbed conditions (Kp > 3). In addition, there is a cold ion component (total energy < 1  
1037 keV) with  $n_{H^+} < 0.1 \text{ cm}^{-3}$  (Lee and Angelopoulos, 2014), likely of ionospheric origin. The ratio of O<sup>+</sup>/H<sup>+</sup>  
1038 number densities strongly depends on geomagnetic activity, with  $n_{O^+}/n_{H^+} \sim 0.1 - 0.5$  for quiet conditions  
1039 (Kp < 3) and  $n_{O^+}/n_{H^+} 0.2 - 1.3$  for disturbed conditions (Kp > 3). Both H<sup>+</sup> and O<sup>+</sup> number densities increase  
1040 during disturbed conditions, but the increase in O<sup>+</sup> number density is larger. The number densities  
1041 reported vary up to half order of magnitude depending on the study, and this is attributable to multiple  
1042 factors including solar cycle, distance to Earth, other orbital biases (magnetic local time, latitude), and  
1043 ion energy range considered by each study.

1044

### 1045 3.3.3.2 Distant Plasma Sheet (> 10 R<sub>E</sub>)

1046 In the distant tail, the total H<sup>+</sup> number density does not depend that much on geomagnetic activity  
 1047 (Mouikis et al., 2010, Maggiolo and Kistler, 2014) as in the near-Earth tail. Lennartson and Shelley (1986)  
 1048 found an anti-correlation between geomagnetic activity and H<sup>+</sup> number density, as opposed to the near-  
 1049 Earth plasma sheet. However, the relative contributions of the ionosphere and the solar wind do  
 1050 depend on geomagnetic activity, with around one third of the H<sup>+</sup> ions coming from the ionosphere  
 1051 during quiet times, and around two thirds coming from the ionosphere during disturbed times. Overall,  
 1052 at distances of 15 – 20 R<sub>E</sub>,  $n_{H^+} \sim 0.2 - 0.3 \text{ cm}^{-3}$ , and is somewhat larger ( $n_{H^+} \sim 0.5 \text{ cm}^{-3}$ ) when distances at  
 1053 10 – 15 R<sub>E</sub> are included in the study. The dependence of  $n_{H^+}$  with solar EUV is also small. On the other  
 1054 hand, the amount of ionospheric O<sup>+</sup> in the distant plasma sheet depends largely on geomagnetic  
 1055 activity, as for the near-Earth plasma sheet. Typical O<sup>+</sup>/H<sup>+</sup> density ratios are  $n_{O^+}/n_{H^+} < 0.1$  for quiet times  
 1056 and  $n_{O^+}/n_{H^+} \sim 0.2 - 0.7$  for disturbed times. In addition, Seki et al. (2003) reported the existence of a  
 1057 cold, hidden plasma population of ionospheric origin (up to few eV) that was only visible during  
 1058 spacecraft eclipses, with number densities of  $\sim 0.2 \text{ cm}^{-3}$  and present < 50 % of the time.

### 1059 3.3.3.3 Lobes

1060 In the tail lobes, the main source of plasma is ionospheric outflows. The lobe populations are usually  
 1061 cold due to the cold nature of the classical polar wind and the velocity filter effect (cf. Section 2.2.2), and  
 1062 therefore they cannot be easily characterized using in-situ ion detectors. We report the results of two  
 1063 studies that used an indirect technique to infer the ion number density in the lobes using the Cluster  
 1064 spacecraft. The average densities reported (cf. Table 2) are roughly consistent but the estimates are  
 1065 somewhat larger in André et al. (2015) than in Svenes et al. (2008). This difference can be explained by  
 1066 the different datasets employed. Svenes et al. (2008) inferred the ion number density from the  
 1067 spacecraft potential, and found the most probable number density to be  $n = 0.047 \text{ cm}^{-3}$ . André et al.  
 1068 (2015) selected data when the spacecraft wake showed that a majority of the ions were cold, and also  
 1069 used the spacecraft potential to estimate the density. Only events with an observed wake (drifting cold  
 1070 ions) and reliable EDI observations were included in the density statistics. In addition, to avoid large  
 1071 errors, only events with  $n > 0.01 \text{ cm}^{-3}$  were included. These criteria select observations with mainly cold  
 1072 ions and exclude observations with low density, mainly at high altitudes. As a result, André et al. (2015)  
 1073 reported cold ion detections 64% of the time, and found  $n > 0.1 \text{ cm}^{-3}$  for most radial distances and  
 1074 geomagnetic conditions. The two methods showed correlation with geomagnetic activity (solar cycle or  
 1075 *K<sub>p</sub>* index) for the cases with large densities (above  $0.2 \text{ cm}^{-3}$ ).

### 1076 3.3.4 Relative importance of ionospheric-originating ions in the Earth's magnetotail

1077 It is well known that O<sup>+</sup>, and cold H<sup>+</sup> in the lobes and in the plasma sheet are of ionospheric origin.  
 1078 However, hot H<sup>+</sup> in the plasma sheet are from both the solar wind and the ionosphere. From inspection  
 1079 of Table 2, the conclusions are that the ionospheric source is the dominant H<sup>+</sup> source during disturbed  
 1080 magnetospheric conditions. During quiet times, the dominant H<sup>+</sup> source is the solar wind, and on  
 1081 average, i.e., quiet plus disturbed times, both H<sup>+</sup> sources are of the same order of magnitude. However,  
 1082 the number of statistical surveys that attempt to distinguish the two H<sup>+</sup> sources is small. In terms of  
 1083 mass density, the near-Earth plasma sheet is most of the time dominated by the ionospheric source,  
 1084 owing to the O<sup>+</sup> contributions. Various studies present the statistics as a function of geomagnetic activity  
 1085 or solar irradiance flux, but we also expect the correlation between plasma sheet parameters and IMF  
 1086 orientation to be large, because of increased convection of magnetic field lines from the lobes, favoring  
 1087 loading of the plasma sheet (e.g., Kistler, 2020).

#### 1088 **4 Effects of ionospheric-originating ions on magnetic reconnection**

1089 Magnetic reconnection is one of the most important transport and energy conversion process in  
 1090 collisionless plasmas. It causes the transport of mass, momentum and energy across topologically  
 1091 distinct plasma regions, initially separated by a thin current sheet. Reconnection regulates solar  
 1092 eruptions, plays a key role in determining the shape and dynamics of planetary magnetospheres, and is  
 1093 involved in major disruptions in astrophysical systems, such as magnetar flares. Even on the ground, in  
 1094 the laboratory, reconnection is an important, albeit undesirable, process in fusion machines, as it can  
 1095 destroy magnetic field confinement. At the Earth's dayside magnetopause, it facilitates the entry of solar  
 1096 wind particles and magnetic energy into the magnetosphere. On the nightside, magnetic reconnection  
 1097 dissipates the accumulated magnetic energy, leading to substorms, storms and auroras, and powers the  
 1098 majority of the deleterious space environment effects collectively referred to as Space Weather.

1099 Owing to its importance, magnetic reconnection has been studied for quite some time, see for instance  
 1100 the review by Yamada et al. (2010), and the review of observations of reconnection by Fuselier and  
 1101 Lewis (2011) and Cassak and Fuselier (2016). Decades of attempts to understand its inner machinery  
 1102 have recently culminated in breakthrough insights into how reconnection works, enabled by the  
 1103 combination of observations from the MMS spacecraft mission, theory and modeling. However, we still  
 1104 know very little about how it starts, and even less about how it stops.

1105 Magnetic reconnection is enabled through a local decoupling between the particles and the magnetic  
 1106 field, which occurs at the smallest spatial scales of the plasma, i.e., the electron inertial length and  
 1107 gyroradius, in the so-called Electron Diffusion Region (EDR). The coupling between the magnetic flux  
 1108 transport and the flow of ions and electrons is described by the equation of the electric field. A general  
 1109 way of looking for regions where this coupling is violated is by analyzing the generalized Ohm's law  
 1110 (Vasyliunas, 1975):

$$1111 \quad \mathbf{E} + \mathbf{v} \times \mathbf{B} = \eta \mathbf{J} + \frac{m_e}{e^2 n} \left[ \frac{\partial \mathbf{J}}{\partial t} + \nabla \cdot (\mathbf{J} \mathbf{v} + \mathbf{v} \mathbf{J}) \right] - \frac{\nabla \cdot \mathbf{P}_e}{en} + \frac{\mathbf{J} \times \mathbf{B}}{en} \quad (1)$$

1112 The different terms on the right-hand side correspond to effects that violate the frozen-in condition  
 1113 ( $\mathbf{E} + \mathbf{v} \times \mathbf{B} = 0$ ), a condition where the magnetic field is carried together with the average plasma  
 1114 flow. For magnetic reconnection, such effects must be present to support the necessary electric field  
 1115 which allows the magnetic field to dissipate and merge, changing the topology of magnetic field lines.

1116 The governing equation for ideal MHD ( $\mathbf{E} + \mathbf{v} \times \mathbf{B} = 0$ ) is scale invariant, meaning that it does not  
 1117 contain any spatial scales. However, the non-ideal terms (right-hand side terms of Equation 1) are  
 1118 characterized by characteristic time or spatial scales, related to the intrinsic properties of the plasma.  
 1119 Owing to the different mass of ions and electrons, they decouple at different scales. The largest of the  
 1120 characteristic scales in Equation 1 correspond to the Hall term,  $\mathbf{J} \times \mathbf{B}/(en)$ , which describes when the  
 1121 ion motion differs from the electron motion and two-fluid effects are in play. This occurs in the Ion  
 1122 Diffusion Region (IDR), with a characteristic spatial scale corresponding the ion inertial length.

1123 The rest of the right-hand side terms of Equation 1 become non-negligible at electron scales, i.e., in the  
 1124 Electron Diffusion Region (EDR). Space plasmas are very dilute and collisions between particles are often  
 1125 negligible. Therefore, dissipation of the magnetic field (positive  $\mathbf{J} \cdot \mathbf{E}$ ) inside the EDR must occur in an  
 1126 unconventional way, since the collisional resistivity is too weak to explain the observations. One of the  
 1127 primary objectives of the MMS mission is to unravel which processes generate sufficient anomalous  
 1128 resistivity for the magnetic field to diffuse and reconfigure inside the EDR in collisionless plasmas. Wave-  
 1129 particle interactions are a strong candidate for the generation of anomalous resistivity (e.g., Graham et  
 1130 al., 2017b, Burch et al., 2018, Li et al., 2020).

1131 The presence of additional plasma populations, e.g. ions of ionospheric origin, with different  
 1132 temperature or mass, has an impact on the different characteristic time and spatial scales associated  
 1133 with the diffusion regions, and affects how the process converts magnetic energy into thermal and  
 1134 kinetic particle energy. Understanding how different plasma populations couple to the reconnection  
 1135 process is what renders the physical process elusive and challenging. The characteristics of the plasma  
 1136 particle gyro orbits around the magnetic field lines can be quantified by the Larmor radius or gyroradius  
 1137 ( $R_{gs}$ ) and the cyclotron frequency ( $\omega_{cs}$ )

$$1138 \quad R_{gs} = \frac{m_s v_{Ts}}{q_s B}, \quad \omega_{cs} = \frac{q_s B}{m_s}, \quad (2)$$

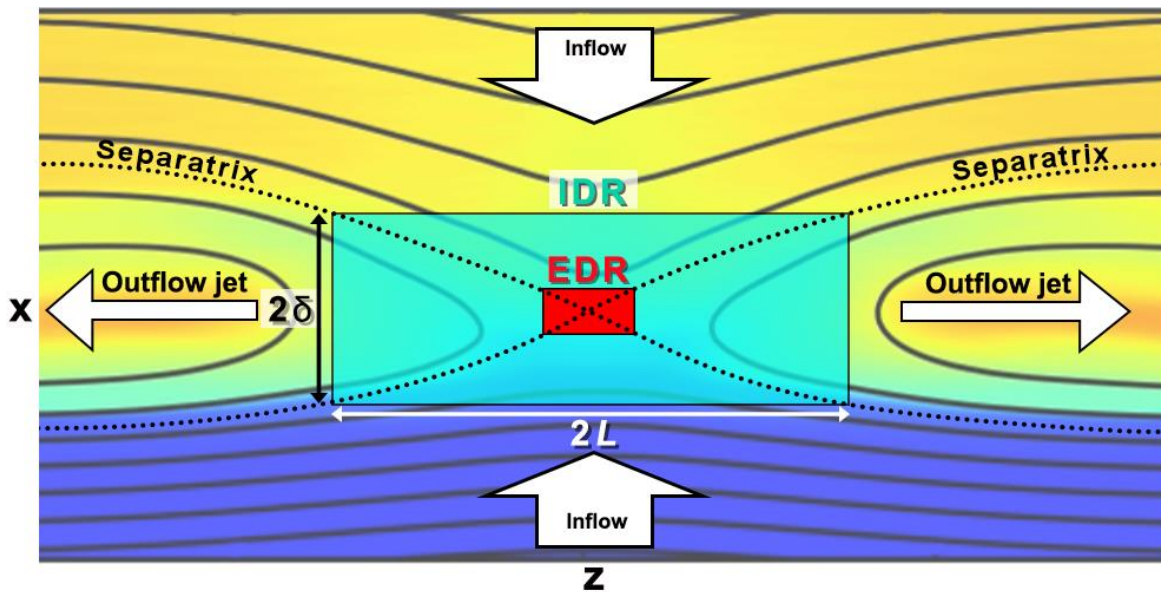
1139  
 1140 where subscript  $s$  denotes the particle species,  $v_T$  is the thermal speed,  $q$  is the particle charge,  $m$  is the  
 1141 particle mass and  $B$  is the magnetic field magnitude. A colder plasma population will, for instance, have  
 1142 a smaller Larmor radius, while the cyclotron frequency remains unchanged, as it does not depend on the  
 1143 thermal speed. If the plasma contains a heavier plasma population (e.g.  $\text{He}^+$ ,  $\text{O}^+$ ), the cyclotron  
 1144 frequency will be smaller (assuming a comparable thermal speed), which has a profound influence on  
 1145 the time evolution of the reconnection process, as discussed in section 4.2.

1146 The ion inertial length is, by definition, equal to the Larmor radius when  $v_{Ti} = v_A$ , i.e., the thermal velocity  
 1147 and Alfvén velocity ( $v_A^2 = B^2 / \mu_0 \rho_i$ ) are equal. For a species  $s$ , the inertial length ( $d_s$ ) and the plasma  
 1148 frequency ( $\omega_{ps}$ ) are defined as

$$1149 \quad d_s = \frac{c}{\omega_{ps}}, \quad \omega_{ps} = \left( \frac{n_s q_s^2}{\epsilon_0 m_s} \right)^{1/2}, \quad (3)$$

1150 where  $c$  is the speed of light,  $\epsilon_0$  is the vacuum dielectric permittivity, and  $n_s$  is the species number  
 1151 density. The height of the IDR and EDR are more precisely described by the particles bounce width,  
 1152 which involves the thermal velocity of the particles and therefore scales approximately as the Larmor  
 1153 radius.

1154 Figure 13 shows a 2D particle-in-cell simulation of asymmetric magnetic reconnection (Dargent et al.  
 1155 2017) that mimics the conditions of coupling between the solar wind (top) and the magnetosphere  
 1156 (bottom). The main regions, namely the EDR, IDR, inflow regions, outflow regions, and separatrices, are  
 1157 sketched. Once the magnetic field reconnects at the EDR, its new topology consists of highly bended  
 1158 magnetic field lines that accelerate to reduce their magnetic tension, generating the so-called  
 1159 reconnection jets, which accelerate and heat the particles, and can extend to spatial scales much larger  
 1160 than the EDR. The center of the EDR is known as the X-point in two dimensions, and extends out of the  
 1161 reconnection plane (XZ plane in Figure 13) forming an X-line in the Y direction in the realistic three-  
 1162 dimensional case. Magnetic reconnection initiates and is maintained at the EDR, but its consequences  
 1163 extend to meso- and system-scales. For instance, in the Earth's magnetosphere, it mediates solar wind  
 1164 plasma entry which drives the global magnetospheric convection cycle.



1165  
 1166 **Figure 13.** Particle-in-cell simulation of magnetic reconnection. The magnetic field lines (solid black lines)  
 1167 break and reconnect at the EDR, generating reconnection outflow jets. In this 2D simulation, the two  
 1168 topological regions that reconnect, have different magnetic field strength and electron density (color-  
 1169 coded), imitating solar wind (top region) – magnetosphere (bottom region) magnetic reconnection.  
 1170 Credit: J. M. Domínguez, adapted from Dargent et al. (2017).

1171  
 1172 As we have seen in section 3.2 and 3.3, plasma of ionospheric origin can dominate the mass density on  
 1173 the magnetospheric side of the magnetopause and in the tail. The system is mass-loaded and the  
 1174 characteristic Alfvén speed is modified, resulting into modified reconnection efficiency. This effect is  
 1175 investigated further in section 4.1. Additional plasma populations also modify the structure and  
 1176 dynamics of the reconnection region, owing to the introduction of multiple time and spatial scales. In  
 1177 section 4.2, we discuss recent modelling and observational works focusing on these effects. The energy  
 1178 conversion due to magnetic reconnection occurs on scales much larger than the tiny electron diffusion

1179 region, involving the ion diffusion region, the separatrices and the exhausts, where the bulk of magnetic  
 1180 energy is converted to particle energy, including the energy of incoming cold ions. We review recent  
 1181 works on the energy balance of magnetic reconnection involving ionospheric-originating ions in section  
 1182 4.3. In section 4.4, we discuss how the presence of heavy ions (mainly  $O^+$ ) in the magnetotail changes its  
 1183 effective thickness and stability, and how this affects reconnection onset. Section 4.5 discusses about  
 1184 the capability of ionospheric populations to suppress magnetic reconnection at the dayside  
 1185 magnetopause.

#### 1186 **4.1 Reconnection rate and mass-loading (macroscopic view)**

1187 Observations over the past decades have shown that the plasma composition in the magnetosphere is a  
 1188 function of both time and location, cf. Sections 2 and 3. The magnetospheric composition usually  
 1189 consists of ion species originating from the solar wind, from H to Fe, e.g., Haaland et al. (2020), and from  
 1190 the ionosphere, consisting of mainly  $H^+$ ,  $He^+$  and  $O^+$ .

1191 To quantify the reconnection rate, i.e. the amount of magnetic flux that is reconnected per unit time, we  
 1192 proceed with a scaling analysis of the quantities involved in the reconnection process. This scaling  
 1193 analysis will allow us to quantify the rate based on quantities measured in the inflow region alone. The  
 1194 aspect ratio ( $\delta/L$ ) of the ion diffusion region (see Figure 13) follows from the mass continuity equation,  
 1195 and can be related to the rate at which magnetic reconnection proceeds, i.e., the amount of magnetic  
 1196 flux that is reconnected per unit time. Assuming the system is in steady-state, the evolutionary equation  
 1197 for mass is

$$1198 \quad \oint_{\mathcal{S}} d\mathbf{S} \cdot (\rho \mathbf{v}) = 0, \quad (4)$$

1199 where  $\mathbf{v}$  is the flow velocity,  $\rho$  is the mass density and  $d\mathbf{S}$  is the outward directed area element of the  
 1200 surface  $\mathcal{S}$ . By considering one quarter of the ion diffusion region in Figure 13, mass continuity relates the  
 1201 mass transport across in inflow surface and outflow surface:

$$1202 \quad \rho_{in} v_{in} L \sim \rho_{out} v_{out} \delta. \quad (5)$$

1203 By evaluating the energy equation (assuming pressure does not contribute to the energy conversion), or  
 1204 by the momentum equation under the assumption that the outflow advection is driven by pressure  
 1205 (Sweet-Parker scheme), an expression for the outflow velocity is found:

$$1206 \quad v_{out}^2 = \frac{B_0^2}{\mu_0 \rho} = v_A^2, \quad (6)$$

1207 where  $\rho$  is the average mass density flowing into the diffusion region from both sides, and  $B_0$  is the  
 1208 magnetic field magnitude adjacent to the diffusion region, which is assumed to be approximately equal  
 1209 to  $B$  anywhere outside the field reversal region. Thus, the advection speed out of the diffusion region,  
 1210 and consequently the inflow speed, is approximately limited to the Alfvén speed just outside the  
 1211 diffusion region. For details, see Vasyliunas (1975).

1212 The normalized reconnection rate is then readily defined as the ratio between the inflow and the  
 1213 outflow velocity, which can be related to the aspect ratio of the diffusion region

$$1214 \quad M_A = \frac{v_{in}}{v_A} \sim \frac{\delta}{L}, \quad (7)$$

1215 where we have assumed an incompressible flow ( $\nabla \cdot \mathbf{v} = 0$ ), and an outflow velocity equal to the Alfvén  
 1216 speed. The reconnection rate is directly related to the out of plane electric field in the diffusion region  
 1217 for 2D geometries ( $E_y$  in the coordinates of Figure 13, also known as reconnection electric field). We

1218 assume that  $\mathbf{E} = -\mathbf{v} \times \mathbf{B}$  holds at the edges of the diffusion region, i.e., the ions are frozen-in to the  
 1219 magnetic field outside the diffusion region, leading to  $v_{in}B_x = v_{out}B_z$ . Taking advantage of  $\nabla \cdot \mathbf{B} = 0$ ,  
 1220 we find

$$1221 \quad E \sim v_A B_z = v_A B_x \frac{\delta}{L}. \quad (8)$$

1222 In steady-state reconnection, the aspect ratio is typically  $\delta/L \sim 0.1$ , found consistently in numerical  
 1223 simulations, spacecraft observations and laboratory experiments (e.g., Yamada et al., 2010, Cassak et al.,  
 1224 2017). As part of the Geospace Environment Modeling (GEM) challenge (Birn et al., 2001), different  
 1225 models of simulations were tested and all the models including the Hall term (multi-fluid, hybrid and full  
 1226 Particle-In-Cell) showed normalized reconnection rates comparable to the 0.1 value. Therefore, many  
 1227 concluded that the Hall term was the cause of the normalized reconnection rate having a rate of 0.1.  
 1228 However, subsequent works questioned this conclusion, see Cassak et al. (2017) and references therein.  
 1229 Liu et al. (2017), recently proposed that this specific value of the reconnection rate likely arises from  
 1230 MHD scale physics. They showed that by maximizing the reconnection rate within MHD-scale  
 1231 constraints, one obtains a maximum reconnection rate around 0.1 - 0.2. Furthermore, they showed that  
 1232 the weakening of the upstream reconnecting field as it extends towards the X-line is more important to  
 1233 the reconnection rate than the weakening of the outflow speed. This is another clue that the MHD-scale  
 1234 play a more important role in this problem compared to the kinetic scales, that were of prior importance  
 1235 in the previous assumption of a Hall term dependence. Liu et al. (2018) generalized those results for  
 1236 asymmetric magnetic reconnection, obtaining similar results.

1237 The reconnection electric field value depends, therefore, on the plasma conditions (magnetic field and  
 1238 number density) upstream of the diffusion region. Varying plasma properties in the inflow region can  
 1239 directly be related to the reconnection electric field through the Alfvén velocity. As we have seen in  
 1240 sections 2 and 3, ionospheric plasma contributions to the mass density in the reconnection regions are  
 1241 often significant. The additional mass lowers the Alfvén speed, resulting in a reduced reconnection  
 1242 electric field and reconnection rate. This effect is termed the "mass-loading effect". Intuitively,  
 1243 additional mass means that the flux tubes have more inertia, making it harder to push the reconnected  
 1244 flux tubes out of the way in the outflow region.

1245 In a symmetric configuration, where the mass-density and the magnetic field of the two inflow regions is  
 1246 equal, the relation between the reconnection electric field, Alfvén velocity and aspect ratio is  
 1247 straightforward and given in Equation 8. For asymmetric reconnection, where both the density and  
 1248 magnetic field strength are different between the two inflow regions, the scaling must include the  
 1249 appropriate contributions from the two inflow regions (1 and 2) to find the effective Alfvén speed  
 1250 (Cassak and Shay, 2007):

$$1251 \quad E \sim \left( \frac{\rho_{out} B_1 B_2}{\rho_1 B_1 + \rho_2 B_2} \right) v_{out} \frac{2\delta}{L}, \quad (9)$$

1252 which reduces to Equation 8 if the density at both inflow regions are the same and equal to the outflow  
 1253 density ( $\rho_1 = \rho_2 = \rho_{out}$ ), and the magnetic field is symmetric ( $B_1 = B_2$ ).

#### 1254 **4.1.1 Local, in-situ observations of the mass-loading effect of ionospheric plasma**

1255 Various works have attempted to measure the mass-loading effect on the reconnection rate at the  
 1256 dayside magnetopause, using local, in-situ spacecraft observations. Su et al. (2000) provided the first  
 1257 observational evidence of the plasmaspheric plume participating in dayside magnetic reconnection.  
 1258 Their observations were made from satellites at geosynchronous orbit ( $6.6 R_E$ ), and therefore their  
 1259 magnetopause observations correspond to times when the magnetosphere is highly compressed by the

1260 solar wind. They observed magnetosheath and plume plasma simultaneously in the same flux tube,  
 1261 concluding that the plume participated in reconnection instead of being convected towards the tail in  
 1262 closed field lines, indicating that the ionospheric-originating ions can potentially mass-load the  
 1263 reconnecting magnetopause.

1264 Walsh et al. (2013), performed a statistical study of reconnecting magnetopause observations with and  
 1265 without a plasmaspheric plume using the THEMIS mission (cf. Section 3.2.2). They found that the  
 1266 outflow velocity resulting from magnetic reconnection was on average smaller for the events with the  
 1267 plume, and attributed this behavior to mass-loading of the magnetopause by plasmaspheric ions.

1268 Wang et al. (2015) measured the reconnection electric field of 8 magnetopause crossings by the Cluster  
 1269 mission, and normalized them to the magnetosheath and magnetosphere upstream conditions, where  
 1270 some of them included cold protons and heavy ions ( $O^+$ ) on the magnetospheric side. Comparing their  
 1271 measurements to the scaling law in Equation 9, they estimated an average aspect ratio of  $\sim 0.07$ . Slightly  
 1272 better correlation was obtained when using only magnetosheath upstream parameters, providing an  
 1273 aspect ratio of 0.09. Overall, the reconnection rate mainly depends on magnetosheath parameters,  
 1274 although significant changes ( $\sim 20\%$ ) on the reconnection rate may be produced by ionospheric ion  
 1275 mass-loading. However, direct measures of the reconnection rate based on local in-situ measurements  
 1276 are challenging and require a number of assumptions and approximations. These include the  
 1277 dependence on distance to the X line, the ability to determine the reconnection plane, and the  $E$  field  
 1278 measurement itself, since the typical reconnection electric field values in the dayside magnetopause are  
 1279 of few mV/m (Genestreti et al., 2018).

1280 Fuselier et al. (2017, 2019a), conducted a statistical survey using 5 months of MMS observations (phase  
 1281 1a) and inferred the mass-loading capabilities of the ionospheric ions. More details on this study are  
 1282 found in section 3.2. In contrast to Walsh et al. (2013) and Wang et al. (2015), the reconnection  $E$  field is  
 1283 not directly measured, it is inferred from Equation 9. They concluded that, for nominal magnetospheric  
 1284 activity, the warm plasma cloak and the plasmaspheric plume can reduce the reconnection electric field  
 1285 by more than 20% only a few percent of the time. They also found that during geomagnetic storms the  
 1286 warm plasma cloak is rich in  $O^+$ , resulting in denser number density. During disturbed conditions, they  
 1287 found that the warm plasma cloak would reduce the reconnection electric field, due to mass-loading, by  
 1288 more than 20% about 25% of the time. By rewriting Equation 9 it is straight-forward to show that the  
 1289 reduction of the reconnection electric field due to magnetospheric mass-loading (ML) can be rewritten  
 1290 as:

1291 
$$R = \frac{E_{ML}}{E_s} = \frac{1}{\sqrt{1 + \frac{n_m B_s}{n_s B_m}}} \quad (10)$$

1292 where subscripts  $m$  and  $s$  correspond to magnetosphere and magnetosheath, respectively (Borovsky et  
 1293 al., 2013). If the magnetospheric number density  $n_m = 0$ , then  $R = 1$  and there is no reduction due to  
 1294 magnetospheric mass-loading. On the other hand, if  $n_m \gg n_s$ ,  $R \sim 0$ . Using typical values for  
 1295 magnetospheric and magnetosheath B field ( $B_m = 50$  nT,  $B_s = 20$  nT) and for magnetosheath number  
 1296 density ( $n_s = 20$   $cm^{-3}$ ), one finds that the magnetosphere density has to be  $n_m = 28$   $cm^{-3}$  to produce a  
 1297 reduction of 20% in the reconnection rate due to magnetospheric mass-loading. Based on the results of  
 1298 section 3.2, this number density at the magnetopause has been reported but it is rare. Very dense  
 1299 plasmaspheric material, rich  $O^+$  warm plasma cloak or a highly compressed magnetosphere ( $n_m \sim 30$   $cm^{-3}$   
 1300 at L-shell = 5, Sheeley et al. (2001)) can lead to densities of  $\sim 28$   $cm^{-3}$  at the magnetopause. Such high-  
 1301 density magnetospheric plasma near the magnetopause occurs mainly during geomagnetic storms. For  
 1302 instance, Fuselier et al. (2020b) compiled a database of magnetopause crossings on the dayside with the  
 1303 highest  $He^+$  densities. These events consisted of high density plasmaspheric plume material. These

1304 extreme events showed that the magnetospheric mass density can reach values above  $50 \text{ amu/cm}^{-3}$ ,  
 1305 which would cause a reduction of the reconnection rate of about 40%.

1306 During periods of Northward IMF,  $\text{O}^+$  escapes from high latitudes directly to the dayside magnetopause,  
 1307 where it can be accumulated until the IMF turns southward and reconnection initiates. Fuselier et al.  
 1308 (2019b), studied a case in such a situation and predicted a transient reduction of the reconnection rate  
 1309 by ionospheric  $\text{O}^+$  of 32%.

#### 1310 **4.1.2 Global measurements of the mass-loading effect of ionospheric plasma**

1311 The mass-loading effect of ionospheric plasma at the dayside magnetopause, and subsequent reduction  
 1312 of the reconnection rate, has also been studied by monitoring the magnetosphere activity using  
 1313 geomagnetic indices. The plasmaspheric drainage plume is a major source of cold plasma at the dayside  
 1314 magnetopause (cf. section 3.2). Borovsky and Denton (2006) used four decades of data from various  
 1315 sources to study the effect of the of the plume on geomagnetic activity. They found a statistically  
 1316 significant reduction of the geomagnetic indices when plasmaspheric plumes were detected in the  
 1317 magnetosphere, for  $Kp > 3$ . They parametrized the solar wind as a function of  $-vB_z$ . The coupling  
 1318 reduction is observed for  $-vB_z > 3000 \text{ nT km/s}$ , i.e., strong flows and/or large southward IMF. Borovsky  
 1319 (2008, 2013) derived an empirical formula relating the solar wind main parameters (magnetic field,  
 1320 velocity and pressure) to the global reconnection rate, inferred from geomagnetic indices. They found  
 1321 that ionospheric plasma starts influencing the reconnection rate (they use the term *plasmasphere*  
 1322 *effect*) when  $\rho_m > M_A^{0.87} \rho_{sw}$ , where  $\rho_m$  is the magnetospheric number density,  $M_A$  is the solar wind  
 1323 Alfvén Mach number, and  $\rho_{sw}$  is the solar wind number density. Coronal Mass Ejections (CMEs) have  
 1324 low  $M_A$ , and therefore the plasmasphere effect is more likely to play a role during the impact of CMEs at  
 1325 the magnetopause (Lavraud and Borovsky, 2008).

#### 1326 **4.1.3 Local versus global control of the integrated reconnection rate**

1327 There has been some debate on whether the integrated dayside reconnection rate, i.e., total amount of  
 1328 magnetic flux merged per unit time, between the solar wind and the Earth's magnetosphere is set by  
 1329 local parameters near the X line, e.g., Borovsky and Birn (2014) (local control), or by the forcing exerted  
 1330 due to upstream conditions of the solar wind, e.g., Lopez (2016) (global control). The local control  
 1331 hypothesis is implied in the works described in section 4.1.2. The global control hypothesis argues that  
 1332 the merging magnetopause reconfigures itself to accommodate eventual magnetospheric mass-loading  
 1333 produced by ionospheric ions, and that there is no net effect over the integrated coupling across the  
 1334 magnetopause. Recent MHD multi-fluid modelling (Zhang 2016, 2017) suggests that for a moderate  
 1335 amount of mass-loading (plasmaspheric plumes with  $\rho_m < 8 \text{ cm}^{-3}$ ), the magnetosheath pressure remains  
 1336 unchanged and the integrated reconnection rate is not significantly affected (global control). On the  
 1337 other hand, for plumes impacting the magnetopause with  $\rho_m \geq 16 \text{ cm}^{-3}$ , the magnetosheath pressure in  
 1338 the inflow region increases owing to pile up of the plasma, leading to more solar wind flux diverted  
 1339 around the magnetosphere (local control). Based on these studies, the two hypotheses (local control  
 1340 versus global control) seem to be complementary.

#### 1341 **4.2 Kinetic effects on magnetic reconnection (microscopic view)**

1342 The most studied effect of ionospheric-originating ions on magnetic reconnection is the mass loading  
 1343 effect (cf. section 4.1). This effect is considered as macroscopic, as its effect are based on fluid  
 1344 arguments. In this subsection, we focus on the kinetic consequences at the smallest scales of the plasma  
 1345 (microscopic view), and the modification of the plasma dynamics under the presence of cold or heavy  
 1346 ionospheric-originating ions. The behavior of the different plasma populations on kinetic scales depends  
 1347 on their characteristics, such as the Larmor radius and cyclotron frequencies (see Equations 2 and 3).

1348 The corresponding characteristic temporal and spatial scales determine which electromagnetic field  
 1349 fluctuations can be followed by the plasma population. Compared to warm protons, a cold proton  
 1350 population will have a smaller Larmor radius, and hence, will decouple at smaller spatial scales, leading  
 1351 to a new scale length in the system. Heavy ions (e.g., He<sup>+</sup>, O<sup>+</sup>) have a larger Larmor radii, and smaller  
 1352 gyrofrequency, compared to protons with the same thermal velocity. This would lead to an additional  
 1353 larger scale length of the system. In addition, these heavier species require that the timescales of the  
 1354 reconnection process to be large enough so that the heavy ions can keep up with the evolution. The  
 1355 inclusion of additional scales results in a multi-scale reconnection process, where the properties of the  
 1356 different plasma populations introduce various competing dynamics.

#### 1357 4.2.1 Multiple ion scales

##### 1358 4.2.1.1 Multi-scale separatrices

1359 Magnetic reconnection is initiated and maintained owing to magnetic field dissipation inside the EDR,  
 1360 with a characteristic spatial scale of a few electron inertial lengths. The EDR is surrounded by the IDR,  
 1361 where the ions become demagnetized. The IDR extends in the form of separatrices, i.e., the boundary  
 1362 that separates the inflow from the outflow regions (see Figure 13). Most of the particles involved in  
 1363 reconnection do not cross the EDR or the IDR, and their energization occurs in the separatrices and in  
 1364 the outflow jet. The separatrices are characterized by a Hall  $\mathbf{E}$  field region of widths comparable to the  
 1365 ion scales, sustained mainly by the  $\mathbf{J} \times \mathbf{B} / en$  term of the Ohm's law.

1366 Wygant et al. (2005) investigated H<sup>+</sup> and O<sup>+</sup> ion energization across the normal electric field layer  
 1367 present in the separatrices of magnetotail reconnection. The observed normal electric field layer  
 1368 thickness was of a few to several H<sup>+</sup> Larmor radius, allowing the H<sup>+</sup> and electron populations to  $\mathbf{E} \times \mathbf{B}$  drift  
 1369 inside the layer and not being significantly energized, while the O<sup>+</sup> was ballistically accelerated by the  
 1370 electric field, resulting into an O<sup>+</sup> energization consistent with the equivalent potential drop observed  
 1371 across the layer. Lindstedt et al. (2010) observed a similar situation at the magnetopause near the cusps,  
 1372 where the normal  $\mathbf{E}$  field near the separatrix of magnetic reconnection accelerated H<sup>+</sup> and O<sup>+</sup> to  
 1373 different energy levels, and attributed it to the different degree of demagnetization of the H<sup>+</sup> and the O<sup>+</sup>  
 1374 inside the layer.

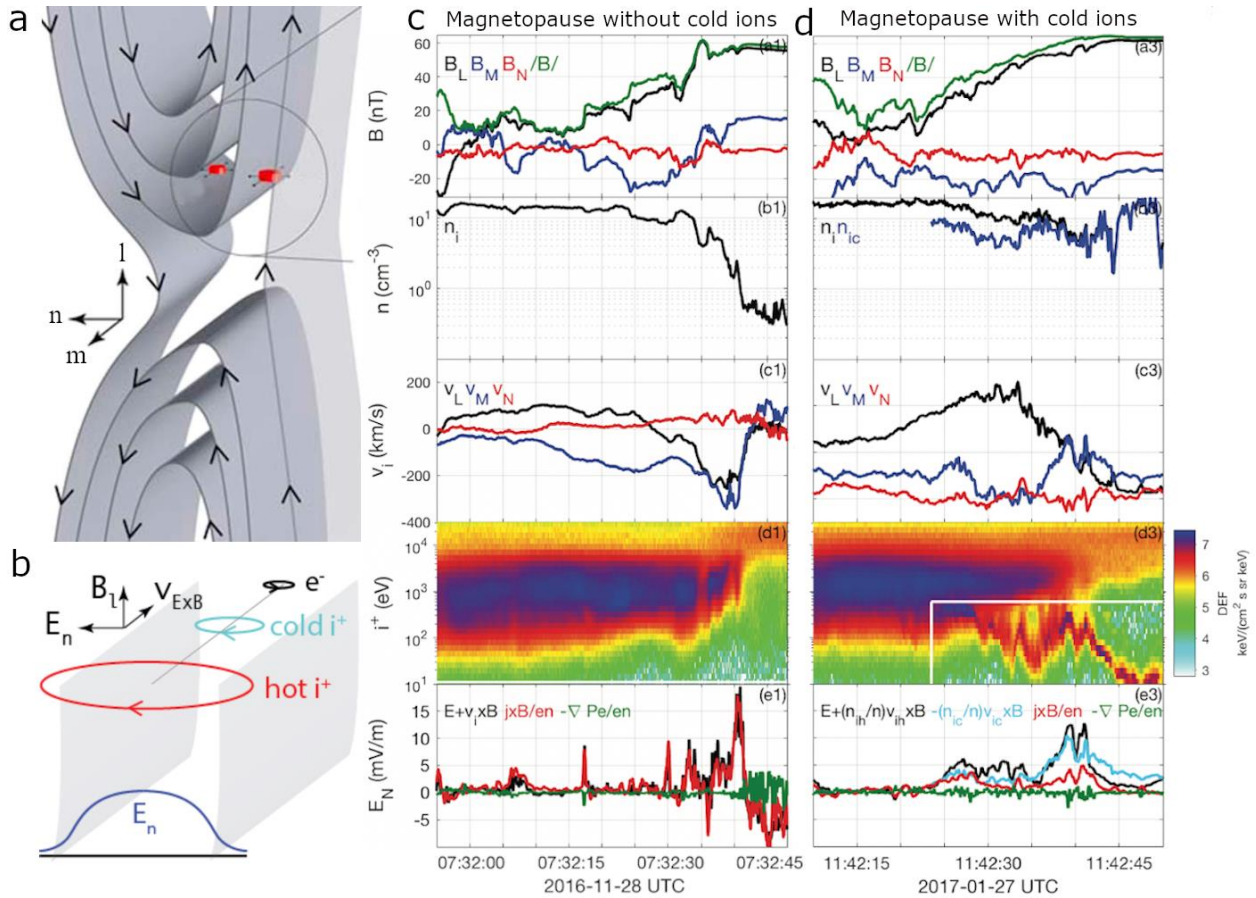
1375 André et al. (2010) and Toledo-Redondo et al. (2015) used Cluster spacecraft measurements to study  
 1376 the behavior of cold ions in the separatrix region of dayside magnetic reconnection. Figure 14a  
 1377 illustrates a 2-spacecraft crossing of the separatrix region, where a 2D, laminar model of magnetic  
 1378 reconnection is assumed. They found that cold ions, owing to their smaller Larmor radius, were able to  
 1379 remain magnetized inside the separatrix region,  $\mathbf{E} \times \mathbf{B}$  drifting together with electrons and therefore  
 1380 reducing the perpendicular currents associated to the Hall effect ( $\mathbf{J} \times \mathbf{B} / en$  term). This situation is  
 1381 sketched in Figure 14b. They accounted for the reduction of the Hall effect by rewriting the steady state  
 1382 Ohm's law in a three-fluid form, including electrons (subscript e), cold ions (subscript c) and hot ions  
 1383 (subscript h):

$$1384 \quad \mathbf{E} = \frac{1}{en} \mathbf{J} \times \mathbf{B} - \frac{n_c}{n} \mathbf{v}_c \times \mathbf{B} - \frac{n_h}{n} \mathbf{v}_h \times \mathbf{B} - \frac{1}{en} \nabla \cdot \mathbf{P}_e \quad (11)$$

1385 where the electron inertia is neglected and  $\mathbf{J} = q(n_h \mathbf{v}_h + n_c \mathbf{v}_c - n_e \mathbf{v}_e)$  is the current density.

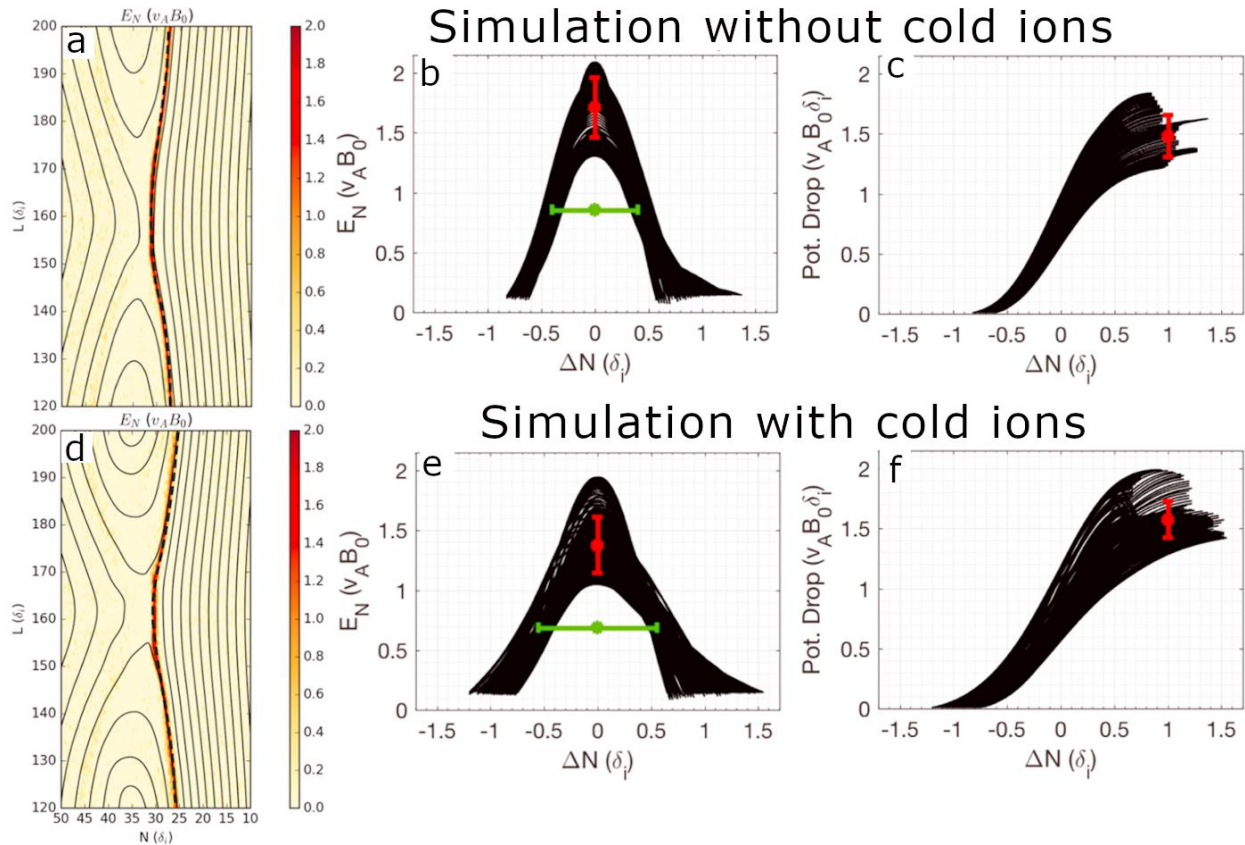
1386 More recently, several works have confirmed quantitatively, using high-resolution MMS measurements,  
 1387 the differential ion behavior between cold and hot ions in the separatrices of magnetic reconnection,  
 1388 both at the dayside magnetopause (André et al., 2016, Toledo-Redondo et al., 2018) and in the  
 1389 magnetotail (Alm et al., 2018, 2019). Figures 14c and 14d show MMS crossings of the separatrix region,  
 1390 without and with cold ions, respectively. One can see that the Hall term of the Ohm's law,  $\mathbf{J} \times \mathbf{B} / en$  (red

1391 curves in bottom panels of Figures 14c and 14d), is smaller in the case with cold ions, because they  
 1392 remain magnetized and  $\mathbf{E} \times \mathbf{B}$  together with electrons (cyan curve in bottom panel of Figure 14d).



1393  
 1394 **Figure 14.** (a) Sketch of multiple spacecraft crossing the separatrix at the dayside magnetopause.  
 1395 Adapted from Toledo-Redondo et al. (2015). (b) Illustration comparing the width of the separatrix layer  
 1396 and its Hall electric field with the gyroradii of electrons, cold ions and hot ions. Adapted from Toledo-  
 1397 Redondo et al. (2015). (c) MMS observations of the separatrix region without cold ions. (e) MMS  
 1398 observations of the separatrix region with cold ions. Adapted from Toledo-Redondo et al. (2018).

1399  
 1400 The Hall  $\mathbf{E}$  field in the separatrices energizes the demagnetized ions that cross it, and therefore one  
 1401 could think that a reduction in the  $\mathbf{J} \times \mathbf{B}/en$  term should end up in a reduction of the ion energization  
 1402 across the separatrices. Toledo-Redondo et al. (2018) investigated that, using PIC simulations. They ran  
 1403 two simulations, where one of them included both hot and cold ions in the magnetosphere side. The  
 1404 two simulations had identical asymptotic conditions, that is, magnetic field magnitude, and total particle  
 1405 density and temperature. They found that the maximum Hall  $\mathbf{E}$  field (Figures 15a and 15d) was reduced  
 1406 in the separatrices for the simulations with cold ions, but that at the same time the Hall  $\mathbf{E}$  field layer was  
 1407 wider (Figures 15b and 15e), resulting into very similar integrated potential drops across the separatrix  
 1408 (Figures 15c and 15f).



1409

1410 **Figure 15.** PIC simulations of dayside reconnection with and without cold ions. (a) Hall electric field for  
 1411 the run without cold ions. (b) Hall electric field statistics for the run without cold ions. (c) Potential drop  
 1412 statistics for the run without cold ions. (d-f) Same as a-c for the run with cold ions. Adapted from  
 1413 Toledo-Redondo et al. (2018).

1414 Dargent et al. (2017) ran two kinetic simulations of magnetic reconnection, with and without cold ions,  
 1415 and noticed the presence of a new electric field layer along the magnetospheric separatrices, adjacent  
 1416 to the Hall  $E$  field layer, but weaker and wider, and with an opposite sign. They argue that this new field  
 1417 results from cold ions being frozen-in at scales where hot ions begin to demagnetize with the proximity  
 1418 of the asymmetric layer. This field is also observable in other simulations (e.g., Dargent et al., 2020),  
 1419 although its relevance for energy conversion from the fields to the particles by reconnection remains  
 1420 unexplored.

#### 1421 4.2.1.2 Multi-scale ion diffusion regions

1422 The presence of multiple ion populations in magnetic reconnection also affects the topology of the IDR.  
 1423 Each ion population has its own characteristic spatial scales, namely the ion inertial length and the  
 1424 Larmor radius, which depend on the atomic mass and temperature of the population. Therefore, each  
 1425 ion population sets its own ion diffusion region, resulting in a multi-scale ion diffusion region (two or  
 1426 more layers). This behavior in magnetic reconnection has been observed both using PIC simulations and  
 1427 spacecraft observations at the Earth's magnetopause and in the magnetotail.

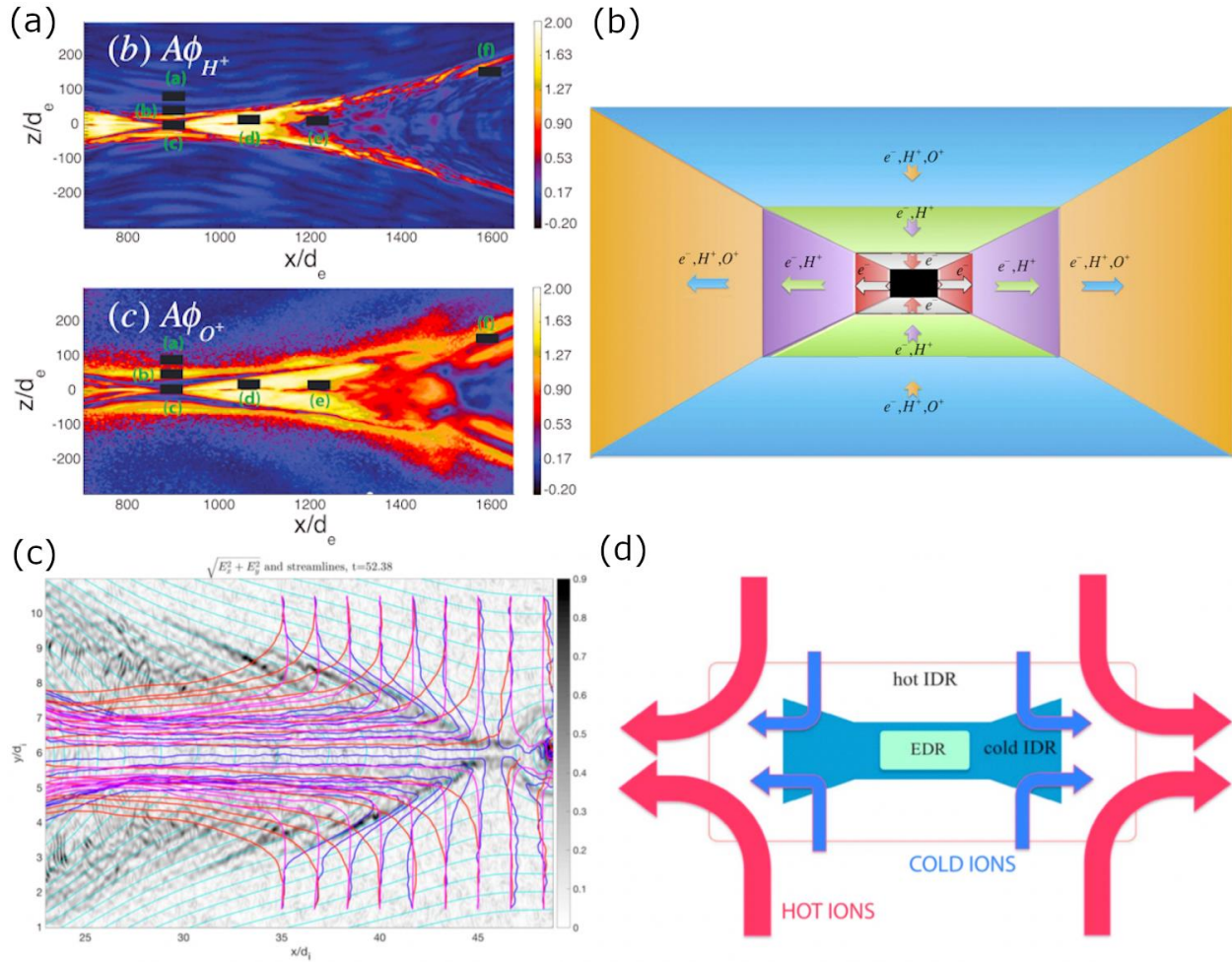
1428 Liu et al. (2015) run 2.5D PIC simulations of symmetric magnetic reconnection, including electrons,  $H^+$   
 1429 and  $O^+$ . They found that, in the steady-state regime, the  $O^+$  demagnetize at a larger scale than  $H^+$ ,  
 1430 measured through the agyrotropy of the populations (Figure 16a). This results in a three-scale diffusion

1431 region, one for each population, as sketched in Figure 16b. They compared the ion velocity distributions  
1432 functions of their simulation to real observations made by Cluster in the Earth's magnetotail, and  
1433 confirmed the multi-scale nature of the diffusion region when  $O^+$  is present.

1434 Divin et al. (2016) also run 2.5D PIC simulations of symmetric magnetic reconnection, and included cold  
1435  $H^+$  in addition to hot  $H^+$  and electrons. They also found a multi-scale diffusion region, where the cold ions  
1436 remain magnetized down to smaller scales than the hot  $H^+$ , owing to their different Larmor radius.  
1437 Figure 16c shows particle trajectories for hot  $H^+$  (red), cold  $H^+$  (pink), and electrons (blue) in the vicinity  
1438 of the X line. Electrons remain frozen-in to the inflowing magnetic field and reach the inner part of the  
1439 current sheet, while hot ions are demagnetized upstream in the inflow region and follow distinct  
1440 trajectories. Cold ions are demagnetized at intermediate distances between the center of the current  
1441 sheet and the region where the hot ions are demagnetized. Figure 16d corresponds to a diagram of the  
1442 multi-scale diffusion region due to electrons, cold  $H^+$  and hot  $H^+$ .

1443 A multi-scale ion diffusion region created by cold and hot  $H^+$  was also reported at the dayside  
1444 magnetopause, using MMS observations (Toledo-Redondo et al., 2016a). MMS crossed near the EDR of  
1445 magnetic reconnection, with both Northward and Southward ion jets observed in the vicinity of the  
1446 magnetopause crossing. The spacecraft separation was of only  $\sim 15$  km, i.e., comparable to the cold  $H^+$   
1447 gyroradius and much shorter than the hot  $H^+$  gyroradius ( $\sim 200$  km). One of the spacecraft observed the  
1448 cold  $H^+$  being accelerated parallel to  $\mathbf{E}$  in a thin region of  $\sim 15$  km width, while the other spacecraft  
1449 observed that cold  $H^+$  was  $\mathbf{E} \times \mathbf{B}$  drifting, in a region where the hot ions were already demagnetized.  
1450 These regions were identified as the cold IDR and the hot IDR, respectively. At the Earth's  
1451 magnetopause, the cold ions are of ionospheric origin and can be present only in the magnetospheric  
1452 inflow region. Therefore, the topology of the multi-scale IDR must be asymmetric. A subjacent question  
1453 that arises from the observation of multi-scale diffusion regions, both symmetric and asymmetric, is  
1454 whether this results into an effective modification of the aspect ratio, i.e., the normalized reconnection  
1455 rate. This question is addressed in Section 4.2.2. Finally, it is known that cold plasma escaping from the  
1456 ionosphere is composed of both cold electrons and cold ions. The effects of multiple electron  
1457 populations (cold and hot) on magnetic reconnection have not been addressed in the literature, to our  
1458 knowledge.

1459



1460  
1461  
1462  
1463  
1464  
1465  
1466  
1467

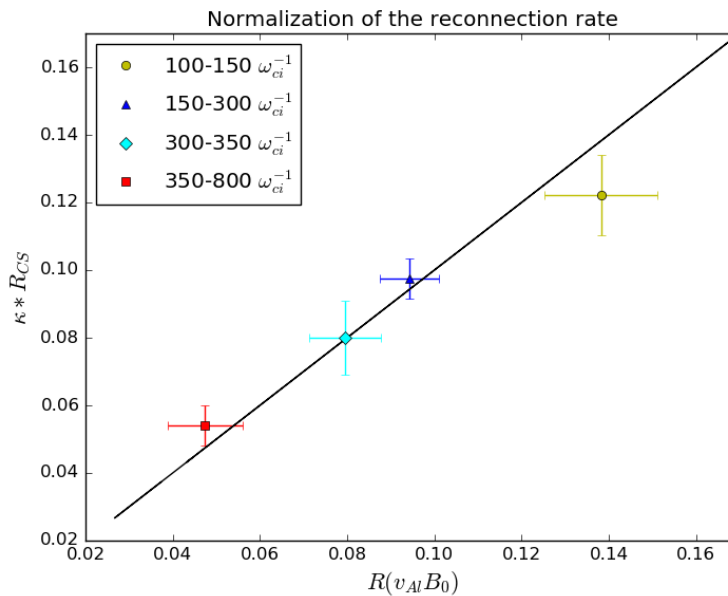
**Figure 16.** PIC simulations of symmetric magnetic reconnection including  $O^+$  (top panels) and cold protons (bottom panels). (a) Agyrotropy of  $H^+$  and  $O^+$ . Adapted from Liu et al. (2015). (b) Sketch of a multi-scale diffusion region including electrons, protons and oxygen. Adapted from Liu et al. (2015). (c) Trajectories of electrons (blue), cold ions (pink) and hot ions (red) inside the diffusion region of symmetric magnetic reconnection. Adapted from Divin et al. (2016). (d) Sketch of a multi-scale diffusion region including electrons, cold protons and hot protons. Adapted from Divin et al. (2016).

1468 **4.2.2 Kinetic effects on reconnection rate**

1469 **4.2.2.1 Cold ions and reconnection rate**

1470 We have already seen in section 4.1 that ions of ionospheric origin have a mass loading effect on the  
 1471 magnetic reconnection rate. However, based on the scaling analysis (see Equations 8 and 9) there is no  
 1472 direct dependence on temperature. For instance, a cold plasma population should not affect the  
 1473 reconnection rate as long as the total mass density remains constant. However, a cold population  
 1474 introduces a new length-scale and therefore should lead to a reconfiguration of the diffusion region. In  
 1475 particular, a cold ion population is expected to reduce the average height of the ion diffusion region ( $\delta$ ).  
 1476 According to Equation 8 (Equation 9 for asymmetric magnetic reconnection), maintaining a constant  
 1477 reconnection rate would then imply that the diffusion region configures itself so that the length  $L$  is  
 1478 reduced in order to keep constant the aspect ratio  $\delta/L$ .

1479 Numerical simulations have shown that the inclusion of multiple ion populations with different  
 1480 temperatures has a negligible effect on the reconnection rate if the mass density is constant, both for  
 1481 symmetric reconnection (Divin et al., 2016, Tenfjord et al., 2020), and for asymmetric reconnection  
 1482 (Dargent et al., 2017, 2020).



1483

1484 **Figure 17.** Scatter plot for all times of the observed reconnection rate versus the calculated one (i.e.  
 1485 Equation 9 assuming  $\delta/L = 0.1$ ). The factor  $\kappa = 0.127$  is calculated such as  $\kappa R_{CS}/R$  scales along a slope of 1.  
 1486 Each point corresponds to the mean value of the reconnection rate on a time interval and the bars  
 1487 associated with them provides one standard deviation. The given time intervals correspond to the  
 1488 different phases of the simulation: yellow, early unsteady magnetic reconnection; blue, steady magnetic  
 1489 reconnection without the plasmaspheric plume; light blue, transition phase with the impact of the  
 1490 plume; red, steady magnetic reconnection with the plasmaspheric plume. Adapted from Dargent et al.  
 1491 (2020).

1492

1493 All these works observe a ratio  $\delta/L \sim 0.1$ , as expected by Liu et al. (2017,2018). In particular, Dargent et  
 1494 al. (2020) studied how the reconnection rate evolves during the impact of a dense, cold, plasmaspheric  
 1495 plume at the reconnecting magnetopause. Figure 17, shows the observed reconnection rate  $R$  versus  
 1496 the expected one, using for calculation Equation 9, assuming  $\delta/L = 0.1$ . The yellow dot represents the  
 1497 average value of the measured versus the expected reconnection rate during the early stage of the

1498 simulation. The observed reconnection rate is larger than the expected using Equation 9 and assuming  
 1499  $\delta/L = 0.1$  in this early stage of the simulation. This is a well-known feature of PIC simulations, often  
 1500 called the overshoot period, that occurs before the simulation reaches steady state (Shay et al., 2007).  
 1501 The blue, cyan, and red dots correspond to the simulation time prior to the arrival of the plasmaspheric  
 1502 plume to the reconnection region (blue), the transition time during the impact of the plume (cyan), and  
 1503 the new steady state reached by magnetic reconnection under the presence of the plume in the  
 1504 magnetospheric inflow region (red). The observed reconnection rate diminishes owing to the mass-  
 1505 loading effect of the plume (cyan and red dots). However, for any of the three phases, the observed  
 1506 reconnection rate matches in average the calculated one using upstream conditions and assuming  $\delta/L \sim$   
 1507  $0.1$ . Despite the dynamic evolution of magnetic reconnection when the plume impacts the layer, this  
 1508 figure confirms that the aspect ratio remains roughly constant in average, with a value of  $\delta/L \sim 0.1$ . A  
 1509 simulation study by Spinnangr et al. (2020) investigated how the reconnection process reorganizes itself  
 1510 on kinetic scales when cold protons get involved in the reconnection process. The authors found, as  
 1511 expected from arguments presented above, a significant reduction of  $\delta$ . From our scaling arguments we  
 1512 would then expect  $L$  to be reduced by the same factor for the ratio to be kept at a constant  $\delta/L \sim 0.1$ .  
 1513 However, the length ( $L$ ) was found to decrease less, which corresponded to a small discrepancy between  
 1514 the rescaled reconnection rate in a simulation with cold ions, and a run without. This suggests that, on  
 1515 ion-scales, some of the assumptions made in the scaling do not always hold. The reorganization of the  
 1516 aspect ratio was found to be enabled by temporal inertia of the cold population during a transition  
 1517 period. This result suggests that the process indeed reconfigures itself to account for the inclusion of an  
 1518 additional ion population with a lower temperature, resulting in a lower reconnection efficiency.

#### 1519 **4.2.2.2 Heavy ions and reconnection rate**

1520 The ion outflow from the high-latitude ionosphere is often composed of  $\text{He}^+$  and  $\text{O}^+$ , in addition to  $\text{H}^+$ ,  
 1521 and is believed to be a significant source of plasma for the terrestrial magnetosphere, and in particular  
 1522 for the tail, cf. Sections 2 and 3. This additional composition leads to an increased total mass density  
 1523 which affects fundamental plasma properties such as the Alfvén speed, plasma pressure and plasma  
 1524 beta. Under geomagnetically active times,  $\text{O}^+$  can even dominate the number density in the  
 1525 magnetotail (e.g., Kistler et al., 2005, Wygant et al., 2005). Similar to cold protons, the presence of  
 1526 heavier species also leads to multiple scales in the reconnection process. Heavier ion populations will  
 1527 have a larger diffusion region compared to that of protons with the same thermal velocity. Additionally,  
 1528 the presence of heavy ions can lead to different Hall dynamics (see Section 4.2.1.1) and also influence  
 1529 the dynamics of dipolarization fronts (Liang et al., 2017, Markidis et al., 2011). Heavier species such as  
 1530  $\text{O}^+$  can also, if magnetized for the spatiotemporal scales of interest, lead to a significant mass-loading of  
 1531 the reconnection process (Hesse and Birn, 2004; Shay and Swisdak, 2004; Borovsky, 2013). Additional  
 1532 effects of heavier ion species also include an impact on the tearing growth rate (Karimabadi et al., 2011),  
 1533 induced charge separation effects, i.e., ambipolar electric fields (Liang et al., 2016) and may contribute  
 1534 to the generation of bifurcated current sheets (George and Jahn, 2020). Wang et al. (2014) investigated  
 1535 the role of  $\text{O}^+$  and  $\text{H}^+$  in a reconnection event using Cluster, and found that the  $\text{O}^+$  energization depends  
 1536 on the location at which the  $\text{O}^+$  enters the exhaust. If the  $\text{O}^+$  enters close to the diffusion region they  
 1537 behave like pick-up ions (Drake, 2009b), whereas further downstream they retained their adiabatic  
 1538 motion and follow the rest of the plasma in the outflow region (Drake, 2009a). Because of the  
 1539 significantly larger inertia of these heavy ions, they also introduce an additional time scale because of  
 1540 the cyclotron frequency dependence on ion mass. The evolutionary timescale of the system must evolve  
 1541 slowly enough for the heavy ions to remain magnetized.

1542 Assuming a magnetic field of  $B_0 = 20$  nT in the magnetotail lobes, the cyclotron period of  $\text{H}^+$  is  $\sim 3$  s, while  
 1543 for  $\text{O}^+$  the cyclotron period is  $\sim 50$  s (since the  $\text{O}^+$  mass is 16 times that of  $\text{H}^+$ ). Magnetic reconnection in

1544 the tail occurs in the plasma sheet, which is emptied by reconnection jets and refilled by plasma in the  
 1545 lobes. If we assume that a reconnection event in the tail (e.g., a Bursty Bulk Flow) lasts for about 200  
 1546 proton cyclotron periods, i.e., about 10 minutes, the heavy, sluggish  $O^+$  has only had time to gyrate  
 1547 about the magnetic field 12 times. This affects the ability of the  $O^+$  to stay magnetized, since in its frame  
 1548 of reference the evolutionary timescale of the reconnection process can be comparable or even faster  
 1549 than its own cyclotron period, preventing the real system to reach steady state (Markidis 2011, Tenfjord  
 1550 et al., 2018, 2019, Kolstø et al., 2020). The effect is that in the frame of the  $O^+$ , the frozen-in  
 1551 approximation no longer holds, and they lose the ability to add inertia to the flux tube. The consequence  
 1552 being that the role of  $O^+$  on the reconnection process can no longer adequately be described as a simple  
 1553 mass-loading process. Using PIC simulations, Tenfjord et al. (2018) investigated the behavior of  $O^+$  as it  
 1554 was captured by reconnection in the tail. They found that  $O^+$ , as a consequence of being demagnetized,  
 1555 was ballistically accelerated, primarily by the Hall electric field. Simulations by Tenfjord et al., 2019 and  
 1556 Kolstø et al., 2020, show that both for symmetrically and asymmetrically distributed  $O^+$ , the  
 1557 reconnection rate is significantly reduced, but not as much as predicted by mass-loading. The authors  
 1558 describe a mechanism where the  $O^+$  population (and the accompanying electrons) acts as an energy sink  
 1559 on the system, altering the energy partitioning. Even though  $O^+$  ions do not directly influence the  
 1560 reconnection process through mass-loading, they do extract energy from the fields that would  
 1561 otherwise be available for accelerating protons and electrons. Based on a scaling analysis the authors  
 1562 find a scaling based on the energy extracted by the unmagnetized species which describes the reduced  
 1563 reconnection rate.

1564 While measurements of the variations in the local rate of reconnection in the tail with heavy ions are  
 1565 still elusive, the global effects of the reconnection rate can be determined by studying the substorm  
 1566 unloading. After substorm onset, reconnection occurs in the magnetotail, reducing the magnetic flux  
 1567 that has built up in the tail lobes during the growth phase. Therefore, the rate of unloading is related to  
 1568 the tail reconnection rate. Liu et al. (2013) studied the global effect of heavy ions on the substorm  
 1569 unloading rate using data from the Cluster mission, by correlating the rate of unloading with the mass  
 1570 density and  $O^+/H^+$  ratio in the tail prior to substorm onset. They found that unloading rate is in fact  
 1571 faster when the  $O^+$  density and  $O^+/H^+$  ratios are higher. This faster rate is contrary to the naïve  
 1572 expectation that increased  $O^+$  should decrease the reconnection rate. Further, the faster rate indicates  
 1573 that other parameters, such as the generally higher activity that usually is associated with high  $O^+$ , or the  
 1574 width of the tail over which the reconnection is occurring may be playing a larger role in determining the  
 1575 unloading than the reconnection rate itself.

1576 At the dayside magnetopause, magnetic reconnection is thought to occur more steadily, due to the  
 1577 dominant effect of the dense inflowing solar wind. In this scenario, the reconnection process can reach  
 1578 steady-state relative to the  $O^+$  characteristic timescale. In this case,  $O^+$  would have sufficient time to  
 1579 remain magnetized, and the reduction of the reconnection rate may be estimated based on mass-  
 1580 loading scaling (Fuselier et al., 2019a, Karimabadi et al., 2011; Kistler et al., 2005; Liu et al., 2015).

#### 1581 **4.2.2.3 Effect of streaming ions (suppression of rate)**

1582 An additional effect beyond the previous described slowdown scenarios is the involvement of a moving  
 1583 cold ion population in the inflow region. Ions originating from the ionosphere stream parallel to the  
 1584 magnetic field (e.g., Bouhram et al., 2004; Fuselier et al., 2019b). The outward velocity is typically  
 1585 observed to be up to  $\sim 50$  km/s (Haaland et al., 2012c; André et al., 2015). Consequently, this additional  
 1586 plasma population adds net, tailward directed momentum to the reconnection process. At the dayside  
 1587 magnetopause, as we move away from the subsolar point, the differential motion between the draped

1588 solar wind and the magnetospheric convection also causes differential ion streams on both sides of the  
1589 reconnection region.

1590 As soon as streaming ions become involved, they contribute to the overall momentum balance, altering  
1591 the reconnection dynamics. Tenfjord et al. (2020) investigated the effect of a streaming cold proton  
1592 population on the reconnection process using PIC-simulations. In the magnetotail, this results in a  
1593 tailward propagation of the reconnection X line. The inclusion of streaming particles influenced the  
1594 initially symmetric outflow regions, producing asymmetries in outflow velocities and temperatures. In a  
1595 similar study, Kolstø et al. (2020) investigated the effect of a streaming oxygen population. As already  
1596 discussed,  $O^+$  remains demagnetized because the cyclotron period is much longer than the evolutionary  
1597 timescale of the reconnection process. Even though  $O^+$  did not exhibit a magnetized behavior they still  
1598 impart their tailward directed momentum through electrostatic coupling. In addition, the authors  
1599 observe the formation of an oxygen wave (Tenfjord et al., 2018) which becomes significantly altered by  
1600 the added momentum.

1601 For cold protons, this additional momentum does not appear to cause any additional reduction of the  
1602 reconnection rate, after correcting for the additional mass. For streaming  $O^+$ , the reduced rate  
1603 corresponds to the scaling described in Tenfjord et al. (2019). However, both in the magnetotail and on  
1604 the dayside, streaming ions can cause drift of the reconnection X line into regions where the plasma  
1605 conditions are different, which could result in an effective change or even suppression of the  
1606 reconnection process.

#### 1607 **4.2.3 Additional consequences of multiple ion populations**

##### 1608 **4.2.3.1 Cold ion crescents**

1609 In weak guide field configurations, the dynamics of the ion populations inside the diffusion region are  
1610 deeply affected. The magnetic field reversal in the center of the reconnecting current sheet implies a  
1611 large B field gradient over less than an ion inertial length, and that the direction of a particle gyration is  
1612 changing through the layer. Thus, the particles will be bouncing between the magnetic field lines on  
1613 either side of the X-line instead of gyrating around one magnetic field line. The bounce-width of a  
1614 population is therefore where the local thermal Larmor radius is equal to the distance to the center of  
1615 the layer (Hesse et al., 2011). This bounce motion produces crescent-shaped distribution functions along  
1616 the boundary of the bounce width. Such a signature in electron distribution functions has been proven  
1617 to be a signature of magnetic reconnection (Hesse et al., 2014, Burch et al., 2016, Bessho et al., 2016),  
1618 and is also expected for ions (Shay et al., 2016, Dargent et al., 2017). Dargent et al. (2019) showed  
1619 another mechanism than can lead to the formation of such crescent-shaped distribution functions for  
1620 cold ions. Cold ion distribution functions take a crescent shape along the magnetospheric separatrixes,  
1621 without magnetic field reversal. In this case, the driver of the signature is the Hall electric field, which  
1622 accelerates and then decelerates the cold ions during one Larmor gyration.

##### 1623 **4.2.3.2 Cold ion beams and lower hybrid instabilities**

1624 In collisionless plasmas, waves play an important role in coupling the various particle populations.  
1625 Graham et al. (2017a) showed, using both spacecraft observations and linear theory modelling, that the  
1626 presence of cold ion beams (ionospheric origin) near the ion diffusion region of magnetic reconnection  
1627 at the Earth's magnetopause can be a free source of energy for the lower hybrid instability, when the  
1628 cold ion beam interacts via an ion-ion instability with the solar wind population. The generated lower  
1629 hybrid waves near the ion diffusion region heat the cold ions, acting as a preconditioner of the  
1630 population in the magnetospheric inflow region.

#### 1631 **4.3 Cold ion energization and energy budget of magnetic reconnection**

1632 One of the most important consequences of magnetic reconnection is the efficient conversion of  
 1633 magnetic energy into kinetic and thermal energies. Ionospheric ions, like any other particle, are  
 1634 energized by magnetic reconnection, in the form of bulk drift acceleration to form the outflow jets plus  
 1635 thermalization. Bulk acceleration is believed to occur in a similar way to pickup processes (e.g., Drake et  
 1636 al. 2009b) when the ionospheric ions enter the outflow jet. From the fluid description given in section  
 1637 4.1, one can see that the outflow velocity, i.e. the Alfvén velocity, scales with the mass density in the  
 1638 inflow regions, and the energy conversion rate from magnetic fields into bulk drift acceleration is  
 1639 balanced.

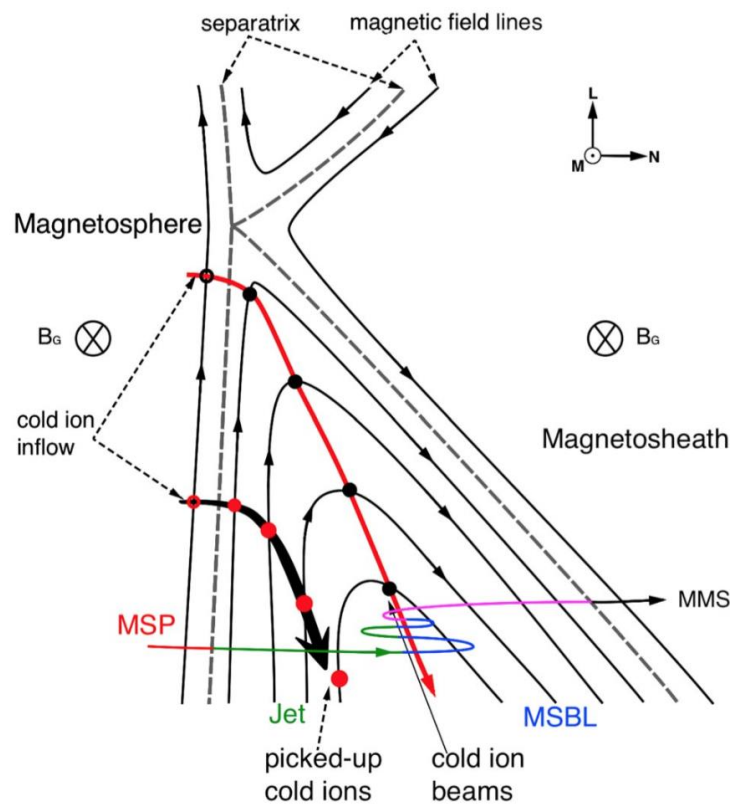
1640 However, magnetic reconnection also produces heating of the particle populations. This heating is  
 1641 accomplished by reconnection by means of various mechanisms, including the reconnection electric  
 1642 field, the Hall electric fields, or wave-particle interactions. These mechanisms occur at kinetic scales of  
 1643 the particles, and the level of turbulence achieved in the outflow jet may condition the amount of net  
 1644 heating.

#### 1645 **4.3.1 Cold ion energization at the Earth's magnetopause**

1646 The typical temperature of the magnetosheath ions is approximately 100 - 200 eV, while the typical  
 1647 temperature of ionospheric cold ions reaching the magnetopause ranges from few eV for plasmaspheric  
 1648 material to several hundred eV for the warm plasma cloak, in addition to the keV plasma sheet ions that  
 1649 can originate in the solar wind or in the ionosphere. Cold ions are accelerated and heated when entering  
 1650 the diffusion region, separatrices, and reconnection outflow region. In those regions, cold ions are  
 1651 mostly mixed together with the magnetosheath ions, and it becomes difficult to distinguish between the  
 1652 two populations. Li et al. (2017) presented an MMS study of a magnetopause crossing with high-density  
 1653 ( $10 - 60 \text{ cm}^{-3}$ ) cold ions and on-going reconnection. Near the magnetospheric edge of the ion jet, they  
 1654 observed a mixture of plasma sheet ions, magnetosheath ions and heated cold ions (Figure 18, black  
 1655 arrow). On the magnetosheath edge of the ion jet, two distinct ion populations were observed. One  
 1656 population with high parallel velocities (200-300 km/s) but rather low temperature ( $\sim 90$  eV) was  
 1657 identified to be a cold ion beam, while the other population was the magnetosheath ions. They  
 1658 separated the distribution functions of the cold ion beams from the entire distribution functions, and  
 1659 computed the partial moments of the cold ion beams. The cold ion beams are hotter than the cold ions  
 1660 in the inflow region, but are still  $\sim 30\%$  colder than the hot magnetosheath ions. In the deHoffman-Teller  
 1661 frame, the field-aligned magnetosheath ions are nearly Alfvénic and move toward the jet region, while  
 1662 the field-aligned cold ions move toward the magnetosheath boundary layer, with much lower speeds.  
 1663 The results suggest that the cold ion beams are accelerated close to the X line (Figure 18, red arrow).  
 1664 The study illustrates that the cold ion heating by reconnection is not homogeneous along the separatrix  
 1665 and suggests it may be lower close to the X line.

1666 Toledo-Redondo et al. (2016b, 2017) reported Cluster and MMS spacecraft observations of cold ion  
 1667 heating in the separatrix region of magnetic reconnection, and showed that both waves near the ion  
 1668 cyclotron frequency and gradients of the Hall electric field were consistent with the amount of heating  
 1669 observed. They estimated, for the four events investigated, that cold ion heating took 10 – 25 % of the  
 1670 energy that went into ion heating, while the other 75 – 90 % went into heating the more abundant  
 1671 magnetosheath ions. Graham et al. (2017a) showed MMS observations of lower hybrid drift waves  
 1672 inside the separatrix region, formed owing to the presence of a cold ion beam, cf section 4.2.3. All these  
 1673 findings indicate that the presence of cold ions modifies the energy partition that is converted from the  
 1674 fields into particle kinetic energy by magnetic reconnection, although quantification of the energy taken  
 1675 by cold ions in the form of bulk kinetic acceleration and heating from a statistical perspective remains  
 1676 unknown.  
 1677

1678 Vines et al. (2017) studied the energization mechanisms of ionospheric ions, including  $H^+$ ,  $He^+$  and  $O^+$ , at  
 1679 the separatrix of magnetopause reconnection, and concluded that the energization mechanisms at play  
 1680 act in a different way depending on the atomic mass unit of the population. They observed two different  
 1681 energization mechanisms. The first energization mechanism was observed inside the outflow jet, and  
 1682 corresponds to the pickup process by the jet, identified by the characteristic velocity-space ring  
 1683 distributions of the ions in the plasma frame. For cold  $H^+$ , the pickup process resulted mainly in bulk drift  
 1684 acceleration. However, they noted that for heavy ions ( $He^+$  and  $O^+$ ) the pickup process occurred non-  
 1685 adiabatically, due to their larger characteristic spatial and time scales (Larmor radius and  
 1686 gyrofrequency), leading to less well-organized ring distributions which included ion heating and velocity  
 1687 and temperature anisotropy. The second energization mechanism was observed near the  
 1688 magnetospheric separatrix region, where the cold  $H^+$  was preferentially heated, and did not affect much  
 1689 the heavy ions. The  $H^+$  heating in the separatrix region is associated with fluctuations generated by a  
 1690 two-stream instability and the lower-hybrid instability (cf. section 4.2.3).



1691  
 1692  
 1693 **Figure 18.** Diagram of the MMS observations during a magnetopause crossing with ongoing magnetic  
 1694 reconnection. Near the magnetospheric edge of the ion outflow jet, heated cold ions are observed  
 1695 (black arrow). Near the magnetosheath edge of the ion outflow jet, cold ions with lower temperature  
 1696 are observed, indicating that the amount of cold ion heating imparted by reconnection depends on the  
 1697 distance to the X line where the cold ions cross the magnetopause boundary. Adapted from Li et al.  
 1698 (2017).

1699  
 1700 **4.3.2 Cold ion energization in the plasma sheet**  
 1701 The plasma sheet boundary layer (PSBL) and the lobe region always contain certain amounts of cold ions  
 1702 of ionospheric origin. The amount of ionospheric plasma present in the magnetotail is variable, depends

1703 on magnetospheric activity (cf. section 3.3), and can affect magnetic reconnection in the magnetotail.  
1704 One prominent feature is that cold ions can create highly structured ion distribution functions including  
1705 ion beams that deviate from a Maxwellian distribution. Among these distributions, counter-streaming  
1706 cold-ion beams along the direction normal to the current sheet were frequently observed in the ion  
1707 diffusion region (e.g., Nagai et al., 1998; Shay et al., 1998; Wygant et al., 2005, Divin et al., 2016). The  
1708 counter-streaming cold ion beams are accelerated to several keV, but are still much colder than the  
1709 plasma sheet hot ions. Using measurements from the Cluster spacecraft, Wygant et al. (2005) showed  
1710 that the counter-streaming cold ions are accelerated by the large-amplitude Hall electric field in the ion  
1711 diffusion region, and numerical simulations from Aunai et al. (2011) and Divin et al. (2016) showed a  
1712 similar acceleration process of cold ions across the current sheet. Combining the THEMIS observations  
1713 and the particle-in-cell simulations, Eastwood et al. (2015) illustrated that the ion beams originate from  
1714 the thermal component of the preexisting plasma sheet hot ion, and are accelerated by the  
1715 reconnection electric field and rotated from out-of-plane direction to the outflow direction by the  
1716 Lorentz force. Some other studies argue that the Fermi effect is the main acceleration mechanism for  
1717 the counter-streaming cold-ion beams (e.g., Runov et al., 2017, Birn et al., 2017; Xu et al., 2019).  
1718 Quantitative and statistical analysis of the cold-ion beams are needed to assess the contribution from  
1719 each acceleration mechanism.

1720

#### 1721 **4.4 Heavy ion effects on reconnection onset and efficiency**

1722 Baker et al. (1982) proposed that  $O^+$  would enhance the linear ion tearing instability in the plasma sheet,  
 1723 and so decrease the stability of the tail to reconnection. Multiple studies since then have attempted to  
 1724 test this. One way to test it is to determine if  $O^+$  is generally enhanced prior to substorm onset. Daglis et  
 1725 al. (1990) found that  $O^+$  was enhanced in the near-earth plasma sheet, but studies further down the tail  
 1726 closer to the reconnection region did not find that  $O^+$  is enhanced prior to onset except during storm-  
 1727 time sawtooth events (Lennartsson et al., 1993, Kistler et al., 2006, Liao et al., 2014). Another method to  
 1728 test this is to determine whether there are more substorm onsets when there is more  $O^+$ . Lennartsson  
 1729 et al. (1993) and Nose et al. (2009) performed long-term studies, and they both showed the well-known  
 1730 correlation between  $O^+/H^+$  and F10.7, but found no correlation between  $O^+/H^+$  ratio and the frequency  
 1731 of substorms over a solar cycle. A final method is to examine the effect of  $O^+$  on loading during  
 1732 substorms. The amount of loading that occurs before substorm onset gives an indication of how  
 1733 unstable the tail is to reconnection onset. If the plasma sheet is more unstable, we would expect there  
 1734 to be less loading before reconnection is triggered. Liu et al., (2013) used Cluster data to determine the  
 1735 correlation between the amount of loading and the  $O^+$  in tail. The amount of loading was positively  
 1736 correlated with the amount of  $O^+$  in the tail, which would indicate that the  $O^+$  in fact makes it harder to  
 1737 trigger substorm onset. They also found that, once reconnection was triggered, the magnetic flux was  
 1738 dissipated faster when  $O^+$  was present, suggesting either an increased reconnection rate or an increased  
 1739 length of the X line in the dawn-dusk direction. Using observations and multi-fluid simulation, Winglee  
 1740 and Harnett (2011) found that  $O^+$  can play a role in the development of substorms, as  $O^+$ -enriched  
 1741 reconnected flux tubes can influence the energy dissipation and modify the plasma distribution in the  
 1742 plasma sheet. Various numerical studies indicate that the ionospheric outflow favors the creation and  
 1743 enhancement of substorms, moves the X line earthward and may be responsible for sawtooth events  
 1744 (e.g., Wiltberger et al., 2010; Brambles et al., 2010, 2013; Zhang et al., 2020). On the contrary, the  
 1745 results by Lund et al. (2018), using cluster observations, seem to indicate that sawtooth events are not  
 1746 produced by the ionospheric outflow.

#### 1747 **4.5 Change of plasma beta and reconnection suppression**

1748 For asymmetric reconnection, where the plasma density and temperature vary greatly across the  
 1749 reconnection region, the net diamagnetic drift of the plasma in the reconnection exhaust can influence,  
 1750 and even suppress, the progression and efficiency of reconnection (Swisdak et al., 2003, 2010, Phan et  
 1751 al. 2013, Cassak and Fuselier, 2016). Diamagnetic drift arises from a thermal plasma pressure gradient as  
 1752 the result of ions and electrons effectively gyrating in opposite directions about the magnetic field. An  
 1753 apparent flow is created if there is a gradient in temperature (gradient in average particle thermal  
 1754 speeds), density (gradient in the number of gyrocenters) or both. During magnetic reconnection this  
 1755 leads to the reconnection X-line moving along the direction of the electron diamagnetic drift due to the  
 1756 ability of electrons to remain magnetized down to smaller scales. When the diamagnetic drift velocity  
 1757 exceeds the Alfvén speed, reconnection can no longer continue, as the force due to the outflowing  
 1758 reconnected magnetic field is unable to overcome the force arising from the effective net plasma drift  
 1759 induced by the pressure gradient (Swisdak et al., 2003). The suppression mechanism may be altered  
 1760 when there is a gradient in temperature but no substantial density gradients present, as demonstrated  
 1761 by Liu et al. (2016) using PIC simulations.

1762 The conditions that may suppress reconnection via diamagnetic drift can be expressed in terms of the  
 1763 difference in plasma  $\beta$  (the ratio of thermal plasma pressure to magnetic pressure) on either side of the  
 1764 current sheet ( $\Delta\beta$ ) and the magnetic shear angle ( $\theta$ ), i.e., the change in magnetic field orientation across  
 1765 the reconnection site:

$$1766 \quad \Delta\beta > 2 \left( \frac{L}{d_i} \right) \tan(\theta/2), \quad (12)$$

1767 where  $L$  is the current sheet width and  $d_i$  is the ion inertial length (Swisdak et al. 2010). For small values  
 1768 of  $\Delta\beta$ , where the plasma populations and magnetic field strength are similar on both sides of the  
 1769 reconnection site, the effect of diamagnetic drift is not substantial, and so reconnection can proceed for  
 1770 a wide range of magnetic field orientations. It is important to note, however, that Equation 12 is a  
 1771 necessary, but not sufficient condition for reconnection to proceed (e.g., Vernisse et al., 2020). As the  
 1772 difference in plasma beta increases, the locations of reconnection sites become increasingly confined to  
 1773 regions of anti-parallel magnetic fields (i.e., regions where magnetic shear angles are closer to  $180^\circ$ )  
 1774 (Swisdak et al., 2003; 2010; Cassak and Fuselier, 2016).

1775 When ionospheric plasma is present on one side of the reconnection site, as is often the case for the  
 1776 Earth's magnetopause, the diamagnetic drift relationship can be altered locally. Through changes in  $\Delta\beta$   
 1777 due to the plasma temperature and density on one side of the reconnection region, the ionospheric-  
 1778 originating plasma reaching the magnetopause may affect reconnection beyond mass-loading the  
 1779 reconnection site, as discussed in sections 4.1 to 4.3. Taking, for instance, typical plasma conditions in  
 1780 the Earth's magnetosheath and normal magnetic field strengths in the magnetosheath and outer  
 1781 magnetosphere, listed in Table 3 and in Cassak and Fuselier (2016), the largest values of  $\Delta\beta$  (and so the  
 1782 most restrictive conditions for reconnection to proceed with regards to the diamagnetic drift effect)  
 1783 occur when the magnetospheric population consists of the plasma sheet population alone, which is  
 1784 always present.

1785 For dense and cold plasma reaching the magnetopause, as when the plume extends to the outer  
 1786 magnetosphere during geomagnetic storms, the resulting  $\Delta\beta$  using typical magnetosheath conditions is  
 1787 very similar to the  $\Delta\beta$  observed for nominal magnetospheric plasma conditions when no dense, cold  
 1788 populations are present, because the plume population does not contribute significantly to the plasma  
 1789 pressure. When the warm plasma cloak population reaches the magnetopause, it contributes to the  
 1790 magnetospheric plasma  $\beta$  (i.e., increasing the temperature and density), resulting in smaller  $\Delta\beta$  across  
 1791 the magnetopause. Therefore, the presence of the warm plasma cloak or, equivalently, heated  
 1792 plasmaspheric material (e.g., Toledo-Redondo et al. 2017) can increase the range of magnetic field  
 1793 orientations across the magnetopause at which magnetic reconnection can proceed, relaxing the  
 1794 condition for the diamagnetic drift suppression mechanism.

1795 The varying plasma conditions under which reconnection suppression due to diamagnetic drift occur  
 1796 hold implications for where reconnection regions at the magnetopause are expected to be located, both  
 1797 for Earth and for other planets like Jupiter and Saturn. The moons of Jupiter and Saturn produce very  
 1798 large amounts of cold, dense plasma, and the very fast rotation of those planets confines the plasma to  
 1799 low-latitudes (Bagenal and Delamere, 2011, Vasylunas, 1983, Louarn et al., 2015 and references  
 1800 therein). Coupled with a much weaker interplanetary magnetic field in the outer solar system and a  
 1801 much stronger planetary magnetic field of these planets, reconnection is thought to be generally  
 1802 suppressed across most of the magnetopause at Jupiter and Saturn via this mechanism of diamagnetic  
 1803 drift (e.g., Desroche et al., 2013). While the diamagnetic drift-induced suppression is just one possible  
 1804 mechanism that may control the continuation after onset and efficiency of reconnection, the simple  
 1805 example above of how an inner plasma source may alter the plasma  $\beta$  at Earth's magnetopause, as well  
 1806 as observations of Saturn's magnetopause (Masters et al., 2012, Fuselier et al., 2014), show the complex  
 1807 effect that cold plasma populations can have on reconnection dynamics.

1808 Unlike the magnetopause, in the Earth's magnetotail, the diamagnetic drift suppression mechanism is  
 1809 not expected to be important because the  $\beta$  magnitude in the plasma sheet is typically smaller than in  
 1810 the magnetosheath. In addition, reconnection in the magnetotail is typically symmetric and involves the

1811 plasma sheet populations in both sides, and therefore no substantial  $\Delta\beta$  is expected across the current  
1812 sheet.

1813 **Table 3.** Representative plasma conditions for different populations and effect on  $\Delta\beta$  at the Earth's  
1814 magnetopause

Plasma Population	Density ( $\text{cm}^{-3}$ )	Temperature (keV)	$B^a$ (nT)	$\beta$	$\Delta\beta =$ $ \beta_{\text{sh}} - \beta_{\text{sp}} $	Presence at Earth's Magnetopause
Magnetosheath	$\sim 20$	0.05 – 0.10	$\sim 20$	$0.80^b$	-	Always
Plasma sheet	$< 1$	10's	50	0.16	0.64	Always
Plasma sheet plus warm plasma cloak / heated plasmaspheric material	$\sim 1$ 's	$\sim 0.1 - 1.0$	50	0.016 – 0.16	0.48 – 0.62	50 – 70% of the time in the dawn sector
Plasma sheet plus plasmaspheric plume	$\sim 10$ 's	$\sim 0.001 - 0.01$	50	$1.6 \times 10^{-3}$	0.64	20 - 25% of the time in the dusk sector
Plasma sheet plus detached plasmaspheric material	$\sim 1$	$\sim 0.001 - 0.01$	50	$1.6 \times 10^{-5}$	0.64	$> 80\%$ of the time in the dusk sector

1815 <sup>a</sup>Nominal magnetic field strength observed in the subsolar magnetosheath and in the Earth's outer  
1816 magnetosphere near the subsolar magnetopause

1817 <sup>b</sup>Most probable magnetosheath  $\beta$  given typical magnetosheath conditions (*Cassak and Fuselier,*  
1818 *2016*)

1819 <sup>c</sup>For calculating  $\beta$  in the magnetosphere, 50 nT is used for the magnetic field strength. Values used  
1820 for "cold", "warm", and "hot" temperatures are 1 eV, 100 eV to 1 keV, and 10 keV, respectively.  
1821 Values used for "dense", "moderately dense", and "tenuous" densities are  $10 \text{ cm}^{-3}$ ,  $1 \text{ cm}^{-3}$ , and  $0.1$   
1822  $\text{cm}^{-3}$ , respectively.

1823

#### 1824 4.6 Summary of cold and heavy ionospheric ions effects on magnetic reconnection

1825 Plasma sheet ions (mainly  $\text{H}^+$ , with number densities  $< 1 \text{ cm}^{-3}$  and temperatures of ones to tens of keV)  
1826 are present both at the dayside magnetopause and in the magnetotail, and their origin is both the solar  
1827 wind and the ionosphere, with variable contributions depending on solar and geomagnetic activity. The  
1828 contribution of each source to the plasma sheet is still subject of debate and we discuss it in Section 5.  
1829 In addition to plasma sheet ions, cold and heavy ionospheric outflows, detached plasmaspheric material  
1830 and the WPC populations can also be present at the reconnection regions (cf. Sections 2.1 and 2.2).  
1831 Section 4 has focused on reviewing the effects of these cold and heavy ionospheric-originating  
1832 populations in magnetic reconnection.

1833 Cold and heavy ionospheric ions are often present and have non-negligible contributions to the mass  
1834 density in the two key reconnecting regions: the dayside magnetopause and the magnetotail. These  
1835 ionospheric ions mass-load the reconnecting flux tubes, and locally reduce the reconnection efficiency.  
1836 This reduction is estimated to be significant ( $>20\%$ ) mainly during storm times, when the production of  
1837 detached plasmasphere material and WPC is larger (Fuselier et al., 2017, 2019a, 2020b). There is also  
1838 indirect evidence, using geomagnetic indices, of global reduction of the coupling to the solar wind when  
1839 large amounts of ionospheric ions are present at the magnetopause, i.e., during storm times (Borovsky  
1840 et al. 2013).

1841 In addition, cold and heavy ionospheric ions introduce multiple spatial and time scales into the  
 1842 reconnection process, owing to the dependence of gyroradius and gyrofrequency on temperature and  
 1843 particle mass. A large set of microphysical effects, including multiple-scale IDRs, wave-particle  
 1844 interactions, etc. are enabled by these multiple ion populations. One then may think that the effective  
 1845 aspect ratio of the diffusion region and the energy conversion mechanisms are changed, resulting in  
 1846 modified reconnection efficiencies. However, according to recent PIC simulations, cold ions do not  
 1847 significantly modify the normalized reconnection rate once a steady state has been reached (Divin et al.,  
 1848 2016, Dargent et al. 2017, 2020). The reconnection rate, on average, may be set by MHD constraints, as  
 1849 suggested by Liu et al. (2017), when no other large-scale forcing acts over the process. A key question is  
 1850 when and for how long magnetic reconnection reaches steady state at the magnetopause. On the other  
 1851 hand,  $O^+$  may not have time to reach steady state in magnetotail reconnection, resulting in a modified  
 1852 reconnection efficiency (Tenfjord et al. 2019). Another key question is to what extent the local  
 1853 properties (MHD and microphysics) of the reconnecting boundary can control the global efficiency of  
 1854 solar wind - magnetosphere coupling versus the global forcing driven by the solar wind (cf. Section  
 1855 4.1.3).

1856 There is direct evidence that cold and heavy ions are heated and accelerated by reconnection in the tail  
 1857 and the dayside magnetopause, and therefore they take a portion of the energy budget of reconnection.  
 1858 Toledo-Redondo et al. (2017), based on four case studies, found that cold ions take 10 – 25 % of the  
 1859 energy that goes into ion heating. However, statistical studies of the energy budget at the  
 1860 magnetopause and magnetotail accounting for ionospheric ions have not been conducted.

1861 Along with effects on the local microphysics of magnetic reconnection, the presence of cold and heavy  
 1862 ionospheric-originating ions can affect dynamics on a more global scale in the magnetosphere. In the  
 1863 magnetotail, it was predicted that the tearing instability threshold should be reduced by the presence of  
 1864  $O^+$  (Baker et al., 1982), favoring the onset of magnetic reconnection. However, spacecraft observations  
 1865 have found that fewer substorms are observed when the magnetotail is loaded with  $O^+$  (Liu et al., 2013).

1866 For the dayside, ionospheric-originating ions can alter local, and possibly global, conditions required for  
 1867 reconnection to occur. The dayside magnetopause is typically asymmetric, with shocked solar wind on  
 1868 one side and magnetospheric plasma on the other. If  $\Delta\beta$  is large across the reconnecting boundary, then  
 1869 magnetic reconnection can be suppressed by the diamagnetic drift. Based on theoretical computations  
 1870 using average magnetosheath conditions, it is expected that the WPC ions will facilitate magnetic  
 1871 reconnection to proceed at the dayside magnetopause at smaller IMF clock angles by reducing  $\Delta\beta$ . More  
 1872 work and observations are needed to further our understanding of the complex cross-scale dynamics  
 1873 resulting from the presence of ionospheric-originating ion populations at reconnection sites.

## 1874 **5 Remaining issues and open questions**

1875 We list below what we consider the most outstanding open questions inferred from this review work,  
 1876 related to ionospheric-originating ions in the magnetosphere and their effects on magnetic  
 1877 reconnection. Table 4 summarizes these open questions, grouped in two categories.

### 1878 **5.1 What is the relative contribution of solar wind versus ionospheric-originating $H^+$ to the** 1879 **magnetosphere?**

1880 The sources of magnetospheric plasma at all energies are the ionosphere and the solar wind. Because  
 1881 the dominant ion population in the magnetosphere is  $H^+$ , and  $H^+$  comes from both the ionosphere and  
 1882 the solar wind, we cannot directly determine the origin of the  $H^+$  in the magnetosphere: it all looks the  
 1883 same. Separating the sources can be done using the minor ion composition (e.g., Kistler, 2020), or using  
 1884 modeling (e.g., Gloer et al., 2020). It is well documented that the ionospheric source becomes

1885 dominant during southward IMF periods associated with increased geomagnetic activity. Overall, the  
 1886 relative contributions of the ionosphere and the solar wind are estimated to be of the same order of  
 1887 magnitude, but precise quantitative knowledge of the relative contributions is missing. Global modelling  
 1888 is the most straightforward method to discriminate the origin of  $H^+$ , but these models are challenging  
 1889 because they need to account for many processes occurring at very different scales.

## 1890 **5.2 How is the plasma sheet formed?**

1891 The plasma sheet boundary layer is a key transition region in which the inflowing lobe ions from the  
 1892 ionosphere enter the plasma sheet region and are energized to become part of it. The lobe ions (eV to  
 1893 hundreds of eV) are energized to the 1 - 10 keV energies typically observed in the plasma sheet, which  
 1894 contains remnants of solar wind and energized polar wind ions from earlier time periods, as well as from  
 1895 more distant places down the magnetotail. It is this changing mix that sets the stage for the  
 1896 reconnection that is observed. MMS measurements across the plasma sheet boundary layer between  
 1897 the lobes and the neutral sheet can show us how this takes place. Model trajectories combined with  
 1898 differential measurement capabilities can show how the plasma sheet is created.

## 1899 **5.3 Does the variable magnetospheric density affect the global coupling with the solar wind efficiency?**

1901 Solar wind - magnetosphere coupling via magnetic reconnection depends mostly on solar wind  
 1902 parameters, in particular the orientation of the IMF, but mass density and magnetic field magnitude also  
 1903 affect the efficiency of the coupling. The magnetospheric mass density at the magnetopause depends on  
 1904 the time history of the magnetosphere. It is not clear to what extent the magnetospheric forcing in  
 1905 general, and the ionospheric source in particular, can exert control of the efficiency of the coupling.  
 1906 Recent modelling (cf. Section 4.1.3) suggests that for a moderate variation of magnetospheric conditions  
 1907 at the magnetopause the system can respond and the efficiency is defined by solar wind parameters. On  
 1908 the other hand, for large mass density changes on the magnetospheric side of the magnetopause, the  
 1909 coupled system efficiency can be modified. Further modelling in this direction, in connection with large  
 1910 statistical surveys of available space and ground datasets may help improving our understanding of what  
 1911 controls the reconnection efficiency between the solar wind and the magnetosphere.

## 1912 **5.4 How do the microphysics introduced by multiple ion populations change magnetic reconnection at MHD scales?**

1914 Recent spacecraft observations have shown that several changes are produced at kinetic scales of  
 1915 magnetic reconnection when multiple ion populations are present. These changes include for instance  
 1916 the generation of ion-ion instabilities or modification of the ion diffusion region. However, recent  
 1917 simulations indicate that these changes by themselves seem not to affect the reconnection efficiency,  
 1918 once a steady-state is reached. How magnetic reconnection self-arranges at fluid scales and how the  
 1919 information of the processes at kinetic scales is transferred to these fluid scales remains a mystery. PIC  
 1920 models of magnetic reconnection are a very powerful tool to improve our understanding on how the  
 1921 system self-arranges at system scales under the presence of multiple ion populations..

## 1922 **5.5 Does the WPC alter the suppression of magnetic reconnection?**

1923 As discussed in Section 4.5, the warm plasma cloak can reduce the difference in plasma beta between  
 1924 the two sides of the dayside magnetopause, and this may facilitate magnetic reconnection to proceed  
 1925 under smaller  $B$  field clock angles. This reasoning comes from the current understanding of analytical  
 1926 theory of magnetic reconnection, but this hypothetical effect of the WPC has not been shown. Global  
 1927 modelling of the magnetosphere including the WPC population can be used to test this effect. In

1928 addition, performing statistics of local observations of the flank magnetopause, where this effect should  
1929 be more pronounced, in the SW parameter space can also help understanding the relative importance  
1930 of the WPC in altering the suppression of reconnection.

### 1931 **5.6 Which portion of the reconnection energy is taken by cold and heavy ions?**

1932 When cold and heavy ions of ionospheric origin are present in the reconnection region, they are both  
1933 accelerated and heated. Therefore they take a portion of the converted magnetic energy by  
1934 reconnection, although there exists no quantification on how the available magnetic energy is  
1935 partitioned among the various ion and electron populations. The heating mechanisms and their relative  
1936 importance are not well understood, and hence is difficult to include them in modelling. On the other  
1937 hand, performing statistics on spacecraft observations of heated cold ions at the magnetopause is  
1938 achievable with current datasets.

### 1939 **5.7 What are the effects of cold electrons in magnetic reconnection?**

1940 There is observational evidence that the cold ion populations in the magnetosphere are accompanied by  
1941 cold electrons. The possible effects of this cold electron population to magnetic reconnection or the  
1942 magnetospheric dynamics has not been widely addressed. However, these electrons are challenging to  
1943 measure, because they are often intermixed with spacecraft-originating photoelectrons, and new  
1944 instrumentation capable of adequately resolving the velocity distribution function of cold electrons may  
1945 be required.

### 1946 **5.8 How ionospheric ions in the plasma sheet condition the onset of magnetic reconnection?**

1947 During disturbed times, the mass density of the magnetotail is usually dominated by  $O^+$ . The presence of  
1948 such heavy ions should reduce the tearing instability threshold and therefore facilitate the onset of  
1949 magnetic reconnection. However, various observational studies seem to indicate the contrary, i.e. that  
1950 reconnection becomes more difficult to trigger reconnection when  $O^+$  is present (cf. Section 4.4). How  
1951 ionospheric ions modify the onset of reconnection and therefore affect the driving storms and  
1952 substorms remains not well understood. More reconnection modelling including multiple ion  
1953 populations can help understanding the role of the ionospheric source.

1954

1955 **Table 4.** Summary of open questions in the role of ionospheric ions and magnetic reconnection in the  
 1956 magnetosphere

Global magnetospheric dynamics	What is the relative contribution of solar wind versus ionospheric-originating H <sup>+</sup> to the magnetosphere?
	How is the plasma sheet formed?
	Does the variable magnetospheric density affect the global coupling with the solar wind efficiency?
Kinetic physics of magnetic reconnection	How do the microphysics introduced by multiple ion populations change reconnection at MHD scales?
	Does the WPC alter the suppression of magnetic reconnection?
	Which portion of the reconnection energy is taken by cold and heavy ions?
	What are the effects of cold electrons in magnetic reconnection?
	How ionospheric ions in the plasma sheet condition the onset of magnetic reconnection?

1957

## 1958 **6 Summary and concluding remarks**

1959 The ionosphere is a prime source of particles for the magnetosphere. The polar wind is constantly  
 1960 outflowing at mid and high latitudes, creating low-energy (eV to tens of eV), light ion populations (H<sup>+</sup>  
 1961 and He<sup>+</sup>). At high latitudes, additional energy sources such as waves in the cusp and auroral oval, create  
 1962 more energetic (hundreds of eV) outflows, that include O<sup>+</sup> in addition to light ions. These outflowing  
 1963 ions travel along the magnetic field lines and are convected together with them. Depending on the solar  
 1964 wind IMF orientation, which drives the convection, the initial parallel velocity of the outflowing ions, and  
 1965 their starting latitude and longitude location in the ionosphere, they will end up in the magnetotail, in  
 1966 the outer dayside magnetosphere, or will be trapped in the inner plasmasphere. Each of these paths  
 1967 may result in various energization levels, and the outflows will become part of the plasma sheet, the ring  
 1968 current, the plasmasphere, or the warm plasma cloak. Most of these ions do not return to the  
 1969 ionosphere, and escape the magnetosphere at an average rate of  $\sim 10^{26}$  ions/s.

1970 Magnetic reconnection takes place at the dayside magnetopause and in the magnetotail, is responsible  
 1971 for the coupling of the magnetosphere to the solar wind, drives storms and substorms, as well as  
 1972 magnetospheric convection, and supplies magnetic energy that is converted to kinetic and thermal  
 1973 energies of the particle populations. Near the magnetopause, the magnetospheric mass density is  
 1974 composed of plasma sheet ions (keV to tens of keV) of both solar wind and ionospheric origin, plus  
 1975 various colder populations (eV to hundreds of eV) of ionospheric origin. The magnetospheric mass  
 1976 density near the magnetopause is variable and dominated by the ionospheric source, although this  
 1977 density is usually smaller than the solar wind density on the other side of the magnetopause. In the tail,  
 1978 the near-Earth plasma sheet mass density is dominated by the ionospheric source all the time. In the  
 1979 distant tail, the ionospheric source becomes dominant during active magnetospheric times. During  
 1980 periods of southward IMF, which are associated to increased geomagnetic activity, more ionospheric-  
 1981 originating ions are found at the magnetopause and in the plasma sheet. These variable contributions to  
 1982 the plasma in the reconnecting regions modulate how reconnection proceeds. Additional mass reduces  
 1983 the rate of magnetic energy conversion at the dayside. In addition, a number of kinetic effects are  
 1984 introduced by the different masses and temperatures of the ionospheric-originating ion populations. For  
 1985 instance, waves are generated by ion-ion instabilities in the reconnection regions, which heat the ions.  
 1986 Cold ions have smaller intrinsic spatial scales (gyroradius), and therefore set different ion diffusion  
 1987 regions. In addition, they can remain magnetized inside the separatrices of reconnection, modifying the

1988 perpendicular currents associated with this region. Heavy ions have larger intrinsic time scales  
1989 (gyrofrequency), and may not be able to follow the intermittent and bursty evolution of magnetic  
1990 reconnection in the tail.

1991 The complexity of the magnetospheric system and its dynamics is enormous. Our knowledge has been  
1992 growing significantly since satellite missions enabled in-situ and remote measurements of it, and with  
1993 the aid of computer simulations. We now understand that the ionospheric source is a major supplier of  
1994 plasma and that the variability of this source affects magnetic reconnection in various ways. However,  
1995 there still remain open questions, in particular about how the system responds to this variability in a  
1996 global sense.

#### 1997 **Acknowledgments, Samples, and Data**

1998 The discoverer of energetic O<sup>+</sup> and He<sup>+</sup> of ionospheric origin in the magnetosphere, Dr. Edward G.  
1999 Shelley, passed away in 2020. This review paper is dedicated to his enduring legacy. We are grateful to  
2000 the International Space Science Institute (ISSI), who made possible this review by funding the  
2001 international team *Cold plasma of ionospheric origin in the Earth's magnetosphere*. Data were not used,  
2002 nor created for this research.  
2003

#### 2004 **References**

- 2005 Akasofu, S. I. (2015). Paradigm transitions in solar–terrestrial physics from 1900: my personal  
2006 view. *History of Geo-and Space Sciences*, 6(1), 23–43.
- 2007 Alm, L., M. André, D. B. Graham, Y. V. Khotyaintsev, A. Vaivads, C. R. Chappell, et al. (2019). MMS  
2008 Observations of Multiscale Hall Physics in the Magnetotail. *Geophysical Research Letters*, pp. 1–  
2009 10, doi:10.1029/2019gl084137.
- 2010 Alm, L., M. André, A. Vaivads, Y. V. Khotyaintsev, R. B. Torbert, J. L. Burch, et al. (2018). Magnetotail hall  
2011 physics in the presence of cold ions. *Geophysical Research Letters*, 45(20), 10,941–10,950,  
2012 doi:10.1029/2018GL079857.
- 2013 André, M., and C. M. Cully (2012). Low-energy ions: A previously hidden solar system particle  
2014 population. *Geophysical Research Letters*, 39(3), doi:10.1029/2011GL050242.
- 2015 André, M., K. Li, and A. I. Eriksson (2015). Outflow of low-energy ions and the solar cycle. *Journal of*  
2016 *Geophysical Research: Space Physics*, 120(2), 1072–1085, doi:10.1002/2014JA020714.
- 2017 André, M., W. Li, S. Toledo-Redondo, Y. V. Khotyaintsev, A. Vaivads, D. B. Graham, et al. (2016). Magnetic  
2018 reconnection and modification of the Hall physics due to cold ions at the magnetopause.  
2019 *Geophysical Research Letters*, 43(13), 6705–6712, doi:10.1002/2016GL069665.
- 2020 André, M., S. Toledo-Redondo and A. W. Yau (2020). Cold ionospheric ions in the magnetosphere, *Space*  
2021 *Physics and Aeronomy Collection Volume 2: Magnetospheres in the Solar System*, Geophysical  
2022 Monograph 259, First Edition. Published 2021 by John Wiley & Sons. DOI:  
2023 10.1002/9781119507512
- 2024 André, M., and A. Yau (1997). Theories and Observations of Ion Energization and Outflow in the High  
2025 Latitude Magnetosphere, *Space Science Reviews*, 80, 27–48, doi: 10.1023/A:1004921619885.
- 2026 André, M., Vaivads, A., Khotyaintsev, Y. V., Laitinen, T., Nilsson, H., Stenborg, G., et al. (2010). Magnetic  
2027 reconnection and cold plasma at the magnetopause. *Geophysical research letters*, 37(22).
- 2028 Aunai, N., Belmont, G., & Smets, R. (2011). Proton acceleration in antiparallel collisionless magnetic  
2029 reconnection: Kinetic mechanisms behind the fluid dynamics. *Journal of Geophysical Research:*  
2030 *Space Physics*, 116 (A9). doi: 10.1029/2011ja016688.

- 2031 Axford, W. I. (1968). The polar wind and the terrestrial helium budget. *Journal of Geophysical*  
 2032 *Research*, 73(21), 6855-6859.
- 2033 Bagenal, F., P. A. and Delamere (2011). Flow of mass and energy in the magnetospheres of Jupiter and  
 2034 Saturn. *Journal of Geophysical Research*, 116, A05209, doi:10.1029/2010JA016294.
- 2035 Baker, D. N., Hones Jr, E. W., Young, D. T., & Birn, J. (1982). The possible role of ionospheric oxygen in  
 2036 the initiation and development of plasma sheet instabilities. *Geophysical Research Letters*, 9(12),  
 2037 1337-1340.
- 2038 Banks, P. M., and Holzer, T. E. (1968). The polar wind. *Journal of Geophysical Research*, 73(21), 6846-  
 2039 6854.
- 2040 Banks, P. M., Nagy, A. F., & Axford, W. I. (1971). Dynamical behavior of thermal protons in the mid-  
 2041 latitude ionosphere and magnetosphere, *Planetary and Space Science*, 19(9), 1053-1067.
- 2042 Barakat, A. R., and Schunk, R. W. (2006). A three-dimensional model of the generalized polar  
 2043 wind. *Journal of Geophysical Research: Space Physics*, 111(A12).
- 2044 Baumjohann, W., G. Paschmann, and C. A. Cattell (1989). Average plasma properties in the central  
 2045 plasma sheet. *Journal of Geophysical Research: Space Physics*, 94(A6), 6597-6606.
- 2046 Benson, R. F. (2010). Four decades of space-born radio sounding, *Radio Science Bulletin*, 333(13), 6705–  
 2047 6712, doi:10.1002/2016GL069665.
- 2048 Berube, D., M. B. Moldwin, S. F. Fung, and J. L. Green (2005). A plasmaspheric mass density model and  
 2049 constraints on its heavy ion concentration. *Journal of Geophysical Research*, 110, A04212,  
 2050 doi:10.1029/2004JA010684.
- 2051 Bessho, N., L.-J. Chen, and M. Hesse (2016). Electron distribution functions in the diffusion region of  
 2052 asymmetric magnetic reconnection. *Geophysical Research Letters*, 43(5), 1828–1836,  
 2053 doi:10.1002/2016GL067886,2016GL067886.
- 2054 Birn, J., Runov, A., & Zhou, X.-Z. (2017). Ion velocity distributions in dipolarization events: Distributions in  
 2055 the central plasma sheet. *Journal of Geophysical Research: Space Physics*, 122 (8), 8014-8025,  
 2056 doi:10.1002/2017ja024230.
- 2057 Birn, J., G. Yur, H. U. Rahman, and S. Minami (1992). On the termination of the closed field line region of  
 2058 the magnetotail. *Journal of Geophysical Research*, 97, 14,833, doi:10.1029/92JA01145
- 2059 Birn, J., Drake, J. F., Shay, M. A., Rogers, B. N., Denton, R. E., Hesse, M., et al. (2001). Geospace  
 2060 Environmental Modeling (GEM) magnetic reconnection challenge. *Journal of Geophysical*  
 2061 *Research: Space Physics*, 106(A3), 3715-3719.
- 2062 Borovsky, J. E. (2008). The rudiments of a theory of solar wind/magnetosphere coupling derived from  
 2063 first principles. *Journal of Geophysical Research: Space Physics*, 113(A8).
- 2064 Borovsky, J. E. (2013). Physical improvements to the solar wind reconnection control function for the  
 2065 Earth's magnetosphere. *Journal of Geophysical Research: Space Physics*, 118(5), 2113-2121.
- 2066 Borovsky, J. E., and Birn, J. (2014). The solar wind electric field does not control the dayside  
 2067 reconnection rate. *Journal of Geophysical Research: Space Physics*, 119(2), 751-760.
- 2068 Borovsky, J. E., and M. H. Denton (2006). Differences between CME-driven storms and CIR-driven  
 2069 storms. *Journal of Geophysical Research*, 111(A7), A07S08, doi:10.1029/2005JA011447.7
- 2070 Borovsky, J. E., and M. H. Denton (2008). A statistical look at plasmaspheric drainage plumes. *Journal of*  
 2071 *Geophysical Research*, 113, A09221, doi:10.1029/2007JA012994.
- 2072 Borovsky, J. E., Denton, M. H., Denton, R. E., Jordanova, V. K., & Krall, J. (2013). Estimating the effects of  
 2073 ionospheric plasma on solar wind/magnetosphere coupling via mass loading of dayside

- 2074 reconnection: Ion-plasma-sheet oxygen, plasmaspheric drainage plumes, and the plasma cloak.  
2075 *Journal of Geophysical Research: Space Physics*, 118, 5695–5719. doi:10.1002/jgra.50527
- 2076 Borovsky, J. E., Thomsen, M. F., McComas, D. J., Cayton, T. E., and Knipp, D. J. (1998). Magnetospheric  
2077 dynamics and mass flow during the November 1993 storm. *Journal of Geophysical Research:*  
2078 *Space Physics*, 103, A11, 26,373-26,394.
- 2079 Bouhram, M., Klecker, B., Miyake, W., Reme, H., Sauvaud, J. A., Malingre, M., et al., (2004). On the  
2080 altitude dependence of transversely heated O<sup>+</sup> distributions in the cusp/cleft. In *Annales*  
2081 *Geophysicae*, 22(5), 1787-1798.
- 2082 Brace, L. H. (2013). Langmuir Probe Measurements in the Ionosphere, pp. 23–35, American Geophysical  
2083 Union (AGU), doi:10.1029/GM102p0023.
- 2084 Brambles, O. J., Lotko, W., Damiano, P. A., Zhang, 1., Wiltberger, M. and Lyon, J. (2010). Effects of  
2085 causally driven cusp O<sup>+</sup> outflow on the storm time magnetosphere-ionosphere system using a  
2086 multifluid global simulation. *Journal of Geophysical Research: Space Physics*, 115(A9).
- 2087 Brambles, O. J., Lotko, W., Zhang, B., Ouellette, J., Lyon, J., and Wiltberger, M. (2013). The effects of  
2088 ionospheric outflow on ICME and SIR driven sawtooth events. *Journal of Geophysical. Research:*  
2089 *Space Physics*, 118, 6026– 6041, doi:[10.1002/jgra.50522](https://doi.org/10.1002/jgra.50522).
- 2090 Burch, J. L., Ergun, R. E., Cassak, P. A., Webster, J. M., Torbert, R. B., Giles, B. L., et al. (2018). Localized  
2091 oscillatory energy conversion in magnetopause reconnection. *Geophysical Research Letters*, 45,  
2092 1237–1245
- 2093 Burch, J. L., R. B. Torbert, T. D. Phan, L.-J. Chen, T. E. Moore, R. E. Ergun, et al. (2016). Electron-scale  
2094 measurements of magnetic reconnection in space, *Science*, doi:10.1126/science.aaf2939.
- 2095 Carpenter, D. L., Giles, B. L., Chappell, C. R., Decreau, P. M. E., Anderson, R. R., Persoon, A. M. et al.  
2096 (1993). Plasmasphere dynamics in the duskside bulge region: A new look at an old topic. *Journal*  
2097 *of Geophysical Research*, 98, 19253-19271.
- 2098 Cassak, P.A., and S. A. Fuselier (2016). Reconnection at Earth’s Dayside Magnetopause, in *Magnetic*  
2099 *Reconnection*, Astrophysics and Space Science Library, **427**, edited by W. Gonzalez and E. Parker,  
2100 Springer, Cham, Switzerland, doi:10.1007/978-3-319-26432-5\_6.
- 2101 Cassak, P. a., and M. a. Shay (2007). Scaling of asymmetric magnetic reconnection: General theory and  
2102 collisional simulations, *Physics of Plasmas*, 14(10), 102,114, doi:10.1063/1.2795630.
- 2103 Cassak, P. A., Liu, Y. H., and Shay, M. A. (2017). A review of the 0.1 reconnection rate problem. *Journal of*  
2104 *Plasma Physics*, 83(5).
- 2105 Chappell, C. R. (1972). Recent satellite measurements of the morphology and dynamics of the  
2106 plasmasphere. *Reviews of Geophysics*, 10(4), 951-979.
- 2107 Chappell, C. R. (1974). Detached plasma regions in the magnetosphere. *Journal of Geophysical*  
2108 *Research*, 79(13), 1861-1870.
- 2109 Chappell, C. R. (1988). The terrestrial plasma source: A new perspective in solar-terrestrial processes  
2110 from Dynamics Explorer. *Reviews of Geophysics*, 26(2), 229-248.
- 2111 Chappell, C. R. (2015). The role of the ionosphere in providing plasma to the terrestrial  
2112 magnetosphere—an historical overview. *Space Science Reviews*, 192, 5-25.
- 2113 Chappell, C. R., C. R. Baugher, and J. L. Horwitz (1980). *New advances in thermal plasma research*.
- 2114 Chappell, C. R., Harris, K. K., & Sharp, G. W. (1971). The dayside of the plasmasphere. *Journal of*  
2115 *Geophysical Research*, 76(31), 7632-7647.

- 2116 Chappell, C. R., Huddleston, M. M., Moore, T. E., Giles, B. L., & Delcourt, D. C. (2008). Observations of  
2117 the warm plasma cloak and an explanation of its formation in the magnetosphere. *Journal of*  
2118 *Geophysical Research: Space Physics*, 113(A9).
- 2119 Chappell, C. R., Moore, T. E., & Waite Jr, J. H. (1987). The ionosphere as a fully adequate source of  
2120 plasma for the Earth's magnetosphere. *Journal of Geophysical Research: Space Physics*, 92(A6),  
2121 5896-5910.
- 2122 Chen, S. H., and Moore, T. E. (2006). Magnetospheric convection and thermal ions in the dayside outer  
2123 magnetosphere. *Journal of Geophysical Research: Space Physics*, 111(A3).
- 2124 Cladis, J. B., H. L. Collin, O. W. Lennartsson, T. E. Moore, W. K. Peterson, and C. T. Russel (2000).  
2125 Observations of centrifugal acceleration during compression of magnetosphere. *Geophysical*  
2126 *Research Letters*, 27, 915, doi:10.1029/1999GL010737
- 2127 Craven, P. D., Gallagher, D. L., & Comfort, R. H. (1997). Relative concentration of He<sup>+</sup> in the inner  
2128 magnetosphere as observed by the DE 1 retarding ion mass spectrometer. *Journal of Geophysical*  
2129 *Research: Space Physics*, 102(A2), 2279-2289.
- 2130 Cohen, C. S., A. B. Galvin, F. M. Ipavich, Y. Kol, A. T. Y. Lui, R. A. Lundgren, R. W. McEntire, and D. J.  
2131 Williams (1998). Concurrent observations of solar wind oxygen by Geotail in the magnetosphere  
2132 and Windin interplanetary space. *Geophysical Research Letters*, 25(15), 2987–2990.
- 2133 Collin, H. L., Peterson, W. K., Lennartsson, O. W., & Drake, J. F. (1998). The seasonal variation of auroral  
2134 ion beams. *Geophysical research letters*, 25(21), 4071-4074.
- 2135 Comfort, R. H. (1998): The Magnetic Mirror Force in Plasma Fluid Models, in Modeling Magnetospheric  
2136 Plasma, Volume 44, AGU Geophysical Monograph Series, eds T. E. Moore, J. H. Waite Jr., T. W.  
2137 Moorehead, W. B. Hanson, doi:10.1029/GM044p0051
- 2138 Comisso, L., and A. Bhattacharjee (2016). On the value of thereconnection rate, *Journal of Plasma*  
2139 *Physics*, 82(6), 1–10, doi:10.1017/S002237781600101X.
- 2140 Cully, C. M., E. F. Donovan, A. W. Yau, and G. G. Arkos (2003). Akebono/Suprathermal Mass  
2141 Spectrometer observations of low-energy ion outflow: Dependence on magnetic activity and solar  
2142 wind conditions. *Journal of Geophysical Research:(Space Physics*, 108, 1093,  
2143 doi:10.1029/2001JA009200.
- 2144 Daglis, I. A., Sarris, E. T., & Kremser, G. (1990). Indications for ionospheric participation in the substorm  
2145 process from AMPTE/CCE observations. *Geophysical research letters*, 17(1), 57-60.
- 2146 Daly, P. W. (1986). Structure of the distant terrestrial magnetotail, *Adv. Space Res.*, 6, 245.  
2147 doi:10.1016/0273-1177(86)90041-4
- 2148 Dandouras, I. (2013). Detection of a plasmaspheric wind in the Earth's magnetosphere by the Cluster  
2149 spacecraft. *Annales Geophysicae*, 0992768), 31(7).

- 2150 Dargent, J., N. Aunai, B. Lavraud, S. Toledo-Redondo, and F. Califano(2019). Signatures of Cold Ions in a  
 2151 Kinetic Simulation of the Reconnecting Magnetopause. *Journal of Geophysical Research: Space*  
 2152 *Physics*, 124(4), 2497–2514, doi:10.1029/2018JA026343.
- 2153 Dargent, J., N. Aunai, B. Lavraud, S. Toledo-Redondo, and F. Califano (2020). Simulation of plasmaspheric  
 2154 plume impact on dayside magnetic reconnection. *Geophysical Research Letters*,  
 2155 doi:10.1029/2019GL086546.8
- 2156 Dargent, J., N. Aunai, B. Lavraud, S. Toledo-Redondo, M. A. Shay, P. A. Cassak, and K. Malakit (2017).  
 2157 Kinetic simulation of asymmetric magnetic reconnection with cold ions, *Journal of Geophysical*  
 2158 *Research: SpacePhysics*, 122(5), 5290–5306, doi:10.1002/2016JA023831.
- 2159 Delcourt, D. C., Chappell, C. R., Moore, T. E., & Waite Jr, J. H. (1989). A three-dimensional numerical  
 2160 model of ionospheric plasma in the magnetosphere. *Journal of Geophysical Research: Space*  
 2161 *Physics*, 94(A9), 11893-11920.
- 2162 Delcourt, D. C., J. A. Sauvaud, T. E. Moore (1993). Polar wind ion dynamics in the magnetotail. *Journal of*  
 2163 *Geophysical Research: Space Physics*, 98(A6), 9155-9169.
- 2164 Denton, M. H., M. G. Henderson, N. Maruyama, and S. A. Fuselier (2019). The cold ion population at  
 2165 geosynchronous orbit and transport to the dayside magnetopause: September 2015 to February  
 2166 2016. *Journal of Geophysical Research*, 124, 8685-8694, doi:10.1029/2019JA026973.
- 2167 Desroche, M., F. Bagenal, P. A. Delamere, and N. Erkaev (2013). Conditions at the magnetopause of  
 2168 Saturn and implications for the solar wind interaction. *Journal of Geophysical Research: Space*  
 2169 *Physics*, 118, 3087– 3095, doi:10.1002/jgra.50294.
- 2170 Divin, A., Khotyaintsev, Y. V., Vaivads, A., André, M., Toledo-Redondo, S., Markidis, S., & Lapenta, G.  
 2171 (2016). Three-scale structure of diusion region in the presence of cold ions. *Journal of Geophysical*  
 2172 *Research: Space Physics*, 121 (12), 12001-12013. doi:10.1002/2016JA023606.
- 2173 Drake, J. F., Cassak, P. A., Shay, M. A., Swisdak, M., & Quataert, E. (2009a). A magnetic reconnection  
 2174 mechanism for ion acceleration and abundance enhancements in impulsive flares. *The*  
 2175 *Astrophysical Journal Letters*, 700(1), L16.
- 2176 Drake, J. F., Swisdak, M., Phan, T. D., Cassak, P. A., Shay, M. A., Lepri, et al. (2009b). Ion heating resulting  
 2177 from pickup in magnetic reconnection exhausts. *Journal of Geophysical Research: Space*  
 2178 *Physics*, 114(A5).
- 2179 Dungey, J.W. (1963). Interactions of solar plasma with the geomagnetic field, *Planetary and Space*  
 2180 *Science*, 10, 233-237, doi:10.1016/0032-0633(63)90020-5
- 2181 Eastwood, J. P., Goldman, M. V., Hietala, H., Newman, D. L., Mistry, R., & Lapenta, G. (2015). Ion  
 2182 reflection and acceleration near magnetotail dipolarization fronts associated with magnetic  
 2183 reconnection. *Journal of Geophysical Research: Space Physics*, 120(1), 511-525.
- 2184 Engwall, E., A. I. Eriksson, C. M. Cully, M. André, R. Torbert, and H. Vaith (2009). Earth’s ionospheric  
 2185 outflow dominated by hidden cold plasma, *Nature Geoscience*, 2, 24–27, doi:10.1038/ngeo387.
- 2186 Frank, L. A., K. L. Ackerson, and D. M. Yeager (1977). Observations of Atomic Oxygen (O+) in the Earth’s  
 2187 Magnetotail, *Journal of Geophysical Research*, 82(1).
- 2188 Fuselier, S. A. (2020). Ionospheric Oxygen ions in the dayside magnetosphere. *Journal of Atmospheric*  
 2189 *and Solar-Terrestrial Physics*, 210, 105448.
- 2190 Fuselier, S. A., Burch, J. L., Mukherjee, J., Genestreti, K. J., Vines, S. K., Gomez, R., et al. (2017).  
 2191 Magnetospheric ion influence at the dayside magnetopause. *Journal of Geophysical Research:*  
 2192 *Space Physics*, 122, 8617–8631, doi:10.1002/2017JA024515.

- 2193 Fuselier, S. A., Dayeh, M. A., Galli, A., Funsten, H. O., Schwadron, N. A., Petrinec, S. M., et al. (2020a).  
 2194 Neutral atom imaging of the solar wind-magnetosphere-exosphere interaction near the subsolar  
 2195 magnetopause. *Geophysical Research Letters*, 47(19), e2020GL089362.
- 2196 Fuselier, S. A., R. Frahm, R., W. S. Lewis, A. Masters, J. Mukherjee, S. M. Petrinec, and I. J. Sillanpaa,  
 2197 (2014). The location of magnetic reconnection at Saturn's magnetopause: A comparison with  
 2198 Earth. *Journal of Geophysical Research: Space Physics*, 119, 2563– 2578,  
 2199 doi:10.1002/2013JA019684.
- 2200 Fuselier, S. A., Haaland, S., Tenfjord, P., Paschmann, G., Toledo-Redondo, S., Malaspina, D., et al.  
 2201 (2020b). High-density magnetospheric He<sup>+</sup> at the dayside magnetopause and its effect on  
 2202 magnetic reconnection. *Journal of Geophysical Research: Space Physics*, in press.
- 2203 Fuselier, S. A., Klumpar, D. M., Peterson, W. K., & Shelley, E. G. (1989). Direct injection of ionospheric O<sup>+</sup>  
 2204 into the dayside low latitude boundary layer. *Geophysical Research Letters*, 16(10), 1121-1124.
- 2205 Fuselier, S. A., and Lewis, W. S. (2011). Properties of near-Earth magnetic reconnection from in-situ  
 2206 observations. *Space science reviews*, 160(1-4), 95.
- 2207 Fuselier, S. A., Mukherjee, J., Denton, M. H., Petrinec, S. M., Trattner, K. J., Toledo-Redondo, S., et al.  
 2208 (2019a). High-density O<sup>+</sup> in Earth's outer magnetosphere and its effect on dayside magnetopause  
 2209 magnetic reconnection. *Journal of Geophysical Research: Space Physics*, 124. doi:10.1029/  
 2210 2019JA027396
- 2211 Fuselier, S., K. Trattner, S. Petrinec, M. Denton, S. Toledo-Redondo, M. André, et al. (2019b). Mass-  
 2212 loading the Earth's dayside magnetopause boundary layer and its effect on magnetic  
 2213 reconnection. *Geophysical Research Letters*, 3, 6204-6213, doi:10.1029/2019gl082384.
- 2214 Garcia, K.S., Merkin, V.G. and Hughes, W.J., 2010. Effects of nightside O<sup>+</sup> outflow on magnetospheric  
 2215 dynamics: Results of multifluid MHD modeling. *Journal of Geophysical Research: Space*  
 2216 *Physics*, 115(A12).
- 2217 Garcia-Sage, K., Moore, T.E., Pembroke, A., Merkin, V.G. and Hughes, W.J., 2015. Modeling the effects of  
 2218 ionospheric oxygen outflow on bursty magnetotail flows. *Journal of Geophysical Research: Space*  
 2219 *Physics*, 120(10), pp.8723-8737.
- 2220 Garrett, H. B. (1981). The charging of spacecraft surfaces, *Reviews of Geophysics*, 19(4), 577–616,  
 2221 doi:10.1029/RG019i004p00577
- 2222 Genestreti, K. J., Goldstein, J., Corley, G. D., Farner, W., Kistler, L. M., Larsen, B. A., et al. (2017).  
 2223 Temperature of the plasmasphere from Van Allen Probes HOPE. *Journal of Geophysical Research:*  
 2224 *Space Physics*, 122(1), 310-323.
- 2225 Genestreti, K. J., Nakamura, T. K. M., Nakamura, R., Denton, R. E., Torbert, R. B., Burch, J. L., et al. (2018).  
 2226 How accurately can we measure the reconnection rate EM for the MMS diffusion region event of  
 2227 11 July 2017?. *Journal of Geophysical Research: Space Physics*, 123(11), 9130-9149.
- 2228 George, D. E., & Jahn, J. M. (2020). Energized oxygen in the magnetotail: Current sheet bifurcation from  
 2229 speiser motion. *Journal of Geophysical Research: Space Physics*, 125(2), e2019JA027339.
- 2230 Glocer, A., Toth, G. and Fok, M.C., (2018). Including kinetic ion effects in the coupled global ionospheric  
 2231 outflow solution. *Journal of Geophysical Research: Space Physics*, 123(4), pp.2851-2871.
- 2232 Glocer, A., Tóth, G., Ma, Y., Gombosi, T., Zhang, J.C. and Kistler, L.M., (2009). Multifluid block-adaptive-  
 2233 tree solar wind roe-type upwind scheme: Magnetospheric composition and dynamics during  
 2234 geomagnetic storms—Initial results. *Journal of Geophysical Research: Space Physics*, 114(A12).
- 2235 Glocer, A., Welling, D., Chappell, C. R., Toth, G., Fok, M. C., Komar, C., et al (2020). A case study on the  
 2236 origin of near-Earth plasma. *Journal of Geophysical Research: Space Physics*, e2020JA028205.

- 2237 Gloeckler, G., & Hamilton, D. C. (1987). AMPTE ion composition results. *Physica Scripta*, 1987(T18), 73.
- 2238 Goldstein, J., Sandel, B. R., Thomsen, M. F., Spasojević, M., & Reiff, P. H. (2004). Simultaneous remote  
2239 sensing and in situ observations of plasmaspheric drainage plumes. *Journal of Geophysical*  
2240 *Research: Space Physics*, 109(A3).
- 2241 Graham, D. B., Khotyaintsev, Y. V., Norgren, C., Vaivads, A., André, M., Toledo-Redondo, S., et al.  
2242 (2017a). Lower hybrid waves in the ion diffusion and magnetospheric inflow regions. *Journal of*  
2243 *Geophysical Research: Space Physics*, 122(1), 517-533.
- 2244 Graham, D. B., Khotyaintsev, Yu. V., Vaivads, A., Norgren, C., André, M., Webster, J. M., et al. (2017b).  
2245 Instability of agyrotropic electron beams near the electron diffusion region. *Physical Review*  
2246 *Letters*, 119(2), 025101.
- 2247 Grande, M., Perry, C. H., Hall, A., Fennell, J., Nakamura, R., & Kamide, Y. (2003). What is the effect of  
2248 substorms on the ring current ion population during a geomagnetic storm?. *GMS*, 142, 75.
- 2249 Grard, R. J. L. (1973). Properties of the satellite photoelectron sheath derived from photoemission  
2250 laboratory measurements. *Journal of Geophysical Research*, 78(16), 2885–2906,  
2251 doi:10.1029/JA078i016p02885
- 2252 Haaland, S., A. Eriksson, E. Engwall, B. Lybekk, H. Nilsson, A. Pedersen, et al. (2012a): Estimating the  
2253 capture and loss of cold plasma from ionospheric outflow. *Journal of Geophysical Research*, Vol  
2254 117, A7. doi:10.1029/2012JA017679
- 2255 Haaland, S. E., K. Li, A. Eriksson, M. André, E. Engwall, M. Forster, et al. (2012b). Cold ion outflow as a  
2256 source of plasma for the magnetosphere, *Geophysical Monograph Series*, 199, 341–353,  
2257 doi:10.1029/2012GM001317.
- 2258 Haaland, S. E., K. Svenes, B. Lybekk, and A. Pedersen (2012c). A survey of the polar cap density based on  
2259 Cluster EFW probe measurements: Solar wind and solar irradiation dependence,  
2260 doi:10.1029/2011JA017250.
- 2261 Haaland, S., Paschmann, G., Øieroset, M., Phan, T., Hasegawa, H., Fuselier, S. A., et al, (2020).  
2262 Characteristics of the flank magnetopause: MMS results. *Journal of Geophysical Research: Space*  
2263 *Physics*, 125(3), e2019JA027623.
- 2264 Hamilton, D. C., Gloeckler, G., Ipavich, F. M., Wilken, B., & Stuedemann, W. (1988). Ring current  
2265 development during the great geomagnetic storm of February 1986. *Journal of Geophysical*  
2266 *Research*, 93, 14343–14355, doi:10.1029/JA093iA12p14343
- 2267 Hesse, M., N. Aunai, D. Sibeck, and J. Birn (2014). On the electron diffusion region in planar, asymmetric,  
2268 systems. *Geophysical Research Letters*, 41, 8673–8680, doi:10.1002/2014GL061586.
- 2269 Hesse, M., T. Neukirch, K. Schindler, M. Kuznetsova, and S. Zenitani (2011), The diffusion region in  
2270 collisionless magnetic reconnection. *Space Science Reviews*, 160(1-4), 3–23, doi:10.1007/s11214-  
2271 010-9740-1.
- 2272 Huddleston, M. M., C. R. Chappell, D. C. Delcourt, T. E. Moore, B. L. Giles and M. O. Chandler (2005). An  
2273 examination of the process and magnitude of ionospheric plasma supply to the magnetosphere.  
2274 *Journal of Geophysical Research: Space Physics*, 110(A12).
- 2275 Jahn, J. M., Goldstein, J., Reeves, G. D., Fernandes, P. A., Skoug, R. M., Larsen, B. A., & Spence, H. E.  
2276 (2017). The warm plasma composition in the inner magnetosphere during 2012–2015. *Journal of*  
2277 *Geophysical Research: Space Physics*, 122(11), 11-018.
- 2278 Jahn, J. M., Goldstein, J., Kurth, W. S., Thaller, S., De Pascuale, S., Wygant, J., et al. (2020). Determining  
2279 Plasmaspheric Density From the Upper Hybrid Resonance and From the Spacecraft Potential: How  
2280 Do They Compare?. *Journal of Geophysical Research: Space Physics*, 125(3), e2019JA026860.

- 2281 Karimabadi, H., V. Roytershteyn, C. G. Mouikis, L. M. Kistler, and W. Daughton (2011). Flushing effect in  
 2282 reconnection: Effects of minor-ity species of oxygen ions. *Planetary and Space Science*, 59(7),  
 2283 526–536,doi:10.1016/j.pss.2010.07.014.
- 2284 Kasahara, S., H. Hasegawa, K. Keika, Y. Miyashita, M. N. Nishino, T. Sotirelis, Y. Saito, and T. Mukai (2008).  
 2285 Escape of high-energy oxygen ions through magnetopause reconnection under northward IMF,  
 2286 *Annales Geophysicae*, 26, 3955–3966.9
- 2287 Kelley, M. C. (2009). *The Earth's ionosphere: plasma physics and electrodynamics*. Academic press.
- 2288 Kistler, L. M. (2016). The impact of O<sup>+</sup> on magnetotail dynamics, In Magnetosphere-ionosphere coupling  
 2289 in the solar system, doi:10.1002/9781119066880.ch6
- 2290 Kistler, L. M. (2020). Ionospheric and solar wind contributions to the storm-time near-earth plasma  
 2291 sheet. *Geophysical Research Letters*, 47, doi:10.1029/2020GL090235
- 2292 Kistler, L. M., and C. G. Mouikis (2016). The inner magnetosphere ion composition and local time  
 2293 distribution over a solar cycle. *Journal of Geophysical Research: Space Physics*, 121(3), 2009–2032,  
 2294 doi:10.1002/2015JA021883.
- 2295 Kistler, L. M., C. Mouikis, E. Moebius, B. Klecker, J. A. Sauvaud, H. Reme, et al. (2005), Contribution of  
 2296 nonadiabatic ions to the cross-tail current in an O<sup>+</sup> dominated thin current sheet. *Journal of*  
 2297 *Geophysical Research: Space Physics*, 110(A6), doi:10.1029/2004JA010653.
- 2298 Kistler, L. M., Mouikis, C. G., Spence, H. E., Menz, A. M., Skoug, R. M., Funsten, H. O., et al. (2016). The  
 2299 source of O<sup>+</sup> in the storm time ring current. *Journal of Geophysical Research: Space*  
 2300 *Physics*, 121(6), 5333-5349.
- 2301 Knudsen, D. J., J. K. Burchill, S. C. Buchert, A. I. Eriksson, R. Gill, J.-E. Wahlund, L. Ahlen, M. Smith, and B.  
 2302 Moffat (2017). Thermal ion imagers and Langmuir probes in the Swarm electric field instruments.  
 2303 *Journal of Geophysical Research: Space Physics*, 122(2), 2655-2673, doi:10.1002/2016JA022571.
- 2304 Kolstø, H. M., M. Hesse, C. Norgren, P. Tenfjord, S. F. Spinnangr, and N. Kwagala (2020). Collisionless  
 2305 Magnetic Reconnection in an Asymmetric Oxygen Density Configuration. *Geophysical Research*  
 2306 *Letters*, 47(1), doi:10.1029/2019gl085359.
- 2307 Krcelic, P., S. Haaland, L. Maes, R. Slapak, and A. Schillings (2019) Estimating the fate of oxygen ion  
 2308 outflow from the high altitude cusp. *Annales Geophysicae*, doi:10.5194/angeo-37-125-2019
- 2309 Kronberg, E. A., Ashour-Abdalla, M., Dandouras, I., Delcourt, D. C., Grigorenko, E. E., Kistler, L. M., et al.  
 2310 (2014). Circulation of heavy ions and their dynamical effects in the magnetosphere: Recent  
 2311 observations and models. *Space Science Reviews*, 184(1-4), 173-235.
- 2312 Laakso, H., and Pedersen, A. (1998). Ambient electron density derived from differential potential  
 2313 measurements. *GEOPHYSICAL MONOGRAPH-AMERICAN GEOPHYSICAL UNION*, 102, 49-54.
- 2314 Lavraud, B., Dunlop, M. W., Phan, T. D., Reme, H., Bosqued, J. M., Dandouras, et al. (2002). Cluster  
 2315 observations of the exterior cusp and its surrounding boundaries under northward  
 2316 IMF. *Geophysical research letters*, 29(20), 56-1.
- 2317 Lavraud, B., & Larson, D. E. (2016). Correcting moments of in situ particle distribution functions for  
 2318 spacecraft electrostatic charging. *Journal of Geophysical Research: Space Physics*, 121(9), 8462-  
 2319 8474.
- 2320 Lavraud, B., H. Rème, M. W. Dunlop, J. M. Bosqued, I. Dandouras, J.-A. Sauvaud, et al. (2005). Cluster  
 2321 observes the high-altitude cusp region, *Surveys in. Geophysics*, 26, No. 1-3, 135-175,  
 2322 doi:10.1007/s10712-005-1875-3
- 2323 Lavraud, B., & Borovsky, J. E. (2008). Altered solar wind-magnetosphere interaction at low Mach  
 2324 numbers: Coronal mass ejections. *Journal of Geophysical Research: Space Physics*, 113(A9).

- 2325 Lee, J. H., Chen, L., Angelopoulos, V., and Thorne, R. M. (2012). THEMIS observations and modeling of  
 2326 multiple ion species and EMIC waves: Implications for a vanishing He<sup>+</sup> stop band. *Journal of*  
 2327 *Geophysical Research: Space Physics*, 117(A6).
- 2328 Lee, J. H., and Angelopoulos, V. (2014). On the presence and properties of cold ions near Earth's  
 2329 equatorial magnetosphere. *Journal of Geophysical Research: Space Physics*, 119(3), 1749-1770.
- 2330 Lee, S. H., Zhang, H., Zong, Q. G., Otto, A., Rème, H., & Liebert, E. (2016). A statistical study of  
 2331 plasmaspheric plumes and ionospheric outflows observed at the dayside magnetopause. *Journal*  
 2332 *of Geophysical Research: Space Physics*, 121(1), 492-506.
- 2333 Lemaire, J., & Schunk, R. W. (1992). Plasmaspheric wind. *Journal of atmospheric and terrestrial*  
 2334 *physics*, 54(3-4), 467-477.
- 2335 Lennartsson, W. (1989). Energetic (0.1-to 16-keV/e) magnetospheric ion composition at different levels  
 2336 of solar F10. 7. *Journal of Geophysical Research: Space Physics*, 94(A4), 3600-3610.
- 2337 Lennartsson, W., and Sharp, R. D. (1985). Relative contributions of terrestrial and solar wind ions in the  
 2338 plasma sheet. *Advances in space research*, 5(4), 411-414.
- 2339 Lennartsson, W., and E. G. Shelley (1986). Survey of 0.1- to 16-keV/e plasmashet ion composition.  
 2340 *Journal of Geophysical Research*, 91, 3061–3076,doi:10.1029/JA091iA03p03061.
- 2341 Lennartsson, O. W., Klumpar, D. M., Shelley, E. G., & Quinn, J. M. (1993). Experimental investigation of  
 2342 possible geomagnetic feedback from energetic (0.1 to 16 keV) terrestrial O<sup>+</sup> ions in the  
 2343 magnetotail current sheet. *Journal of Geophysical Research: Space Physics*, 98(A11), 19443-19454.
- 2344 Li, Q., Winglee, R. M., Wilber, M., Chen, L., and Parks, G. (2000). The geopause in relation to the plasma  
 2345 sheet and the low-latitude boundary layer: Comparison between Wind observations and  
 2346 multifluid simulations. *Journal of Geophysical Research*, 105( A2), 2563– 2587,  
 2347 doi:[10.1029/1999JA900369](https://doi.org/10.1029/1999JA900369).
- 2348 Li, W. Y., Andre, M., Khotyaintsev, Y. V., Vaivads, A., Fuselier, S. A., Graham, D. B., . . . Burch, J. (2017).  
 2349 Cold ionospheric ions in the magnetic reconnection outflow region. *Journal of Geophysical*  
 2350 *Research: Space Physics*, 122 (10), 10,194-10,202. doi: 10.1002/2017ja024287.
- 2351 Li, W. Y., Graham, D. B., Khotyaintsev, Y. V., Vaivads, A., André, M., Min, K., et al. (2020). Electron  
 2352 Bernstein waves driven by electron crescents near the electron diffusion region. *Nature*  
 2353 *Communications*, 11(1), 141.
- 2354 Li, K., Haaland, S., Eriksson, A., André, M., Engwall, E., Wei, Y., ... & Ren, Q. Y. (2013). Transport of cold  
 2355 ions from the polar ionosphere to the plasma sheet. *Journal of Geophysical Research: Space*  
 2356 *Physics*, 118(9), 5467-5477.
- 2357 Liang, H., Ashour-Abdalla, M., Lapenta, G., & Walker, R. J. (2016). Oxygen impacts on dipolarization  
 2358 fronts and reconnection rate. *Journal of Geophysical Research: Space Physics*, 121(2), 1148-1166.
- 2359 Liang, H., Lapenta, G., Walker, R. J., Schriver, D., El-Alaoui, M., & Berchem, J. (2017). Oxygen acceleration  
 2360 in magnetotail reconnection. *Journal of Geophysical Research: Space Physics*, 122(1), 618-639.
- 2361 Liao, J., Cai, X., Kistler, L. M., Clauer, C. R., Mouikis, C. G., Klecker, B., & Dandouras, I. (2014). The  
 2362 relationship between sawtooth events and O<sup>+</sup> in the plasma sheet. *Journal of Geophysical*  
 2363 *Research: Space Physics*, 119(3), 1572–1586. <http://doi.org/10.1002/2013JA019084>
- 2364 Liao, J., Kistler, L. M., Mouikis, C. G., Klecker, B., Dandouras, I., & Zhang, J. C. (2010). Statistical study of  
 2365 O<sup>+</sup> transport from the cusp to the lobes with Cluster CODIF data. *Journal of Geophysical Research:*  
 2366 *Space Physics*, 115(A12).

- 2367 Liao, J., Kistler, L. M., Mouikis, C. G., Klecker, B., & Dandouras, I. (2012). Solar cycle dependence of the  
 2368 cusp O<sup>+</sup> access to the near-Earth magnetotail. *Journal of Geophysical Research: Space*  
 2369 *Physics*, 117(A10).
- 2370 Liao, J., Kistler, L. M., Mouikis, C. G., Klecker, B., & Dandouras, I. (2015). Acceleration of O<sup>+</sup> from the cusp  
 2371 to the plasma sheet. *Journal of Geophysical Research: Space Physics*, 120(2), 1022-1034.
- 2372 Liemohn, M. W., Moore, T. E., & Craven, P. D. (2007). Geospace activity dependence of cold, streaming  
 2373 ions in the near-Earth magnetotail. *Journal of atmospheric and solar-terrestrial physics*, 69(1-2),  
 2374 135-141.
- 2375 Lindstedt, T., Y. V. Khotyaintsev, A. Vaivads, M. André, H. Nilsson, and M. Waara (2010). Oxygen  
 2376 energization by localized perpendicular electric fields at the cusp boundary. *Geophysical Research*  
 2377 *Letters*, 37, L09103, doi:10.1029/2010GL043117.
- 2378 Liu, Y., Kistler, L. M., Mouikis, C. G., Klecker, B., & Dandouras, I. (2013). Heavy ion effects on substorm  
 2379 loading and unloading in the Earth's magnetotail. *Journal of Geophysical Research: Space*  
 2380 *Physics*, 118(5), 2101-2112.
- 2381 Liu, Y. H., & Hesse, M. (2016). Suppression of collisionless magnetic reconnection in asymmetric current  
 2382 sheets. *Physics of Plasmas*, 23(6), 060704.
- 2383 Liu, Y.-H., M. Hesse, P. A. Cassak, M. A. Shay, S. Wang, and L.-J. Chen(2018). On the collisionless  
 2384 asymmetric magnetic reconnection rate, *Geophysical Research Letters*,45(8), 3311–3318,  
 2385 doi:10.1002/2017GL076460.
- 2386 Liu, Y. H., M. Hesse, F. Guo, W. Daughton, H. Li, P. A. Cassak, & M. A. Shay (2017). Why does Steady-  
 2387 State Magnetic Reconnection have a Maximum Local Rate of Order 0.1?, *Physical Review*  
 2388 *Letters*,118(8), 1–6,doi:10.1103/PhysRevLett.118.085101.
- 2389 Liu, Y. H., C. G. Mouikis, L. M. Kistler, S. Wang, V. Roytershteyn, & H. Karimabadi (2015). The heavy ion  
 2390 diffusion region in magnetic reconnection in the Earth's magnetotail. *Journal of Geophysical*  
 2391 *Research*,120(5), 3535–3551, doi:10.1002/2015JA020982.
- 2392 Lopez, R. E. (2016). The integrated dayside merging rate is controlled primarily by the solar wind. *Journal*  
 2393 *of Geophysical Research: Space Physics*, 121(5), 4435-4445.
- 2394 Louarn, P., N. Andre, C. M. Jackman, S. Kasahara, E. A. Kronberg, & M. F. Vogt (2015). Magnetic  
 2395 Reconnection and Associated Transient Phenomena Within the Magnetospheres of Jupiter and  
 2396 Saturn, *Space Science. Reviews*, 187, 181–227, doi:10.1007/s11214-014-0047-5.
- 2397 Lund, E. J., Nowrouzi, N., Kistler, L. M., Cai, X., & Frey, H. U. (2018). On the Role of Ionospheric Ions in  
 2398 Sawtooth Events. *Journal of Geophysical Research: Space Physics*, 123(1), 665–684.  
 2399 <http://doi.org/10.1002/2017JA024378>
- 2400 Lybekk, B., A. Pedersen, S. Haaland, K. Svenes, A. N. Fazakerley, A. Masson, M. G. G. T. Taylor, and J.-G.  
 2401 Trotignon (2012). Solar cycle variations of the Cluster spacecraft potential and its use for electron  
 2402 density estimations. *Journal of Geophysical Research: Space Physics*, 117, A01217,  
 2403 doi:10.1029/2011JA016969.
- 2404 Maggiolo, R., and Kistler, L. M. (2014). Spatial variation in the plasma sheet composition: Dependence  
 2405 on geomagnetic and solar activity. *Journal of Geophysical Research: Space Physics*, 119(4), 2836-  
 2406 2857.
- 2407 Markidis, S., Lapenta, G., Bettarini, L., Goldman, M., Newman, D., & Andersson, L. (2011). Kinetic  
 2408 simulations of magnetic reconnection in presence of a background O<sup>+</sup> population. *Journal of*  
 2409 *Geophysical Research: Space Physics*, 116(A1).
- 2410 Masters, A., J. P. Eastwood, M. Swisdak, M. F. Thomsen, C. T. Russell, N. Sergis, et al. (2012). The

- 2411 importance of plasma  $\beta$  conditions for magnetic reconnection at Saturn's magnetopause.  
2412 *Geophysical Research Letters*, 39, L08103, doi:10.1029/2012GL051372.
- 2413 Moore, T. E., Chandler, M. O., Fok, M. C., Giles, B. L., Delcourt, D. C., Horwitz, J. L., & Pollock, C. J. (2001).  
2414 Ring currents and internal plasma sources. *Space Science Reviews*, 95(1-2), 555-568.
- 2415 Moore, T. E., C. R. Chappell, M. O. Chandler, P. D. Craven, B. L. Giles, C. J. Pollock, et al. (1997). High-  
2416 altitude observations of the polar wind, *Science*, 277, 349–351,  
2417 doi:10.1126/science.277.5324.349.
- 2418 Moore, T.E. and Delcourt, D.C. (1995). The geopause. *Reviews of Geophysics*, 33(2), pp.175-209.
- 2419 Moore, T.E., Fok, M. C., Chandler, M. O., Chappell, C. R., Christon, S. P., Delcourt, D. C., et al. (2005).  
2420 Plasma sheet and (nonstorm) ring current formation from solar and polar wind sources. *Journal of*  
2421 *Geophysical Research: Space Physics*, 110(A2).
- 2422 Moore, T. E., and J. L. Horwitz (2007). Stellar ablation of planetary atmospheres, *Reviews of Geophysics*,  
2423 45, RG3002, doi:10.1029/2005RG000194.
- 2424 Mouikis, C. G., Kistler, L. M., Liu, Y. H., Klecker, B., Korth, A., & Dandouras, I. (2010). H<sup>+</sup> and O<sup>+</sup> content  
2425 of the plasma sheet at 15–19 Re as a function of geomagnetic and solar activity. *Journal of*  
2426 *Geophysical Research: Space Physics*, 115(A12).
- 2427 Nagai, T., Johnson, J. F. E., & Chappell, C. R. (1983). Low-energy (< 100 eV) ion pitch angle distributions in  
2428 the magnetosphere by ISEE 1. *Journal of Geophysical Research: Space Physics*, 88(A9), 6944-6960.
- 2429 Nagai, T., Fujimoto, M., Saito, Y., Machida, S., Terasawa, T., Nakamura, R., et al. (1998). Structure and  
2430 dynamics of magnetic reconnection for substorm onsets with geotail observations. *Journal of*  
2431 *Geophysical Research: Space Physics*, 103 (A3), 4419-4440. doi: 10.1029/97ja02190.
- 2432 Nilsson, H., E. Engwall, A. Eriksson, P. A. Puhl-Quinn, and S. Arvelius (2010). Centrifugal acceleration in  
2433 the magnetotail lobes, *Annales Geophysicae*, 28, 569, doi:10.5194/angeo-28-569-2010
- 2434 Nilsson, H., Waara, M., Marghita, O., Yamauchi, M., Lundin, R., Reme, H., et al. (2008). An assessment of  
2435 the role of the centrifugal acceleration mechanism in high altitude polar cap oxygen ion outflow,  
2436 *Annales Geophysicae*, 26, 145, doi: 10.5194/angeo-26-145-2008
- 2437 Nishida, A., T. Mukai, T. Yamamoto, Y. Saito, and M. Kokubun (1996). Magnetotail convection in  
2438 geomagnetically active times, 1. distance to the neutral lines, *Journal of Geophys. Geomagn.*, 48,  
2439 489, doi:10.5636/jgg.48.489
- 2440 Nosé, M., Ieda, A., & Christon, S. P. (2009). Geotail observations of plasma sheet ion composition over  
2441 16 years: On variations of average plasma ion mass and O<sup>+</sup> triggering substorm model. *Journal of*  
2442 *Geophysical Research: Space Physics*, 114(A7).
- 2443 Ogawa, Y., I. Häggström, S. C. Buchert, K. Oksavik, S. Nozawa, M. Hirahara, et al. (2009). On the source of  
2444 the polar wind in the polar top- side ionosphere: First results from the EISCAT Svalbard radar,  
2445 *Geophysical Research Letters*, 36, L24103, doi:10.1029/2009GL041501.
- 2446 Parker, E. N. 1973 The reconnection rate of magnetic fields. *Astrophys. J.* 180, 247.
- 2447 Perroomian, V. and Ashour-Abdalla, M. (1995). Relative contribution of the solar wind and the auroral  
2448 zone to near-Earth plasmas. *GEOPHYSICAL MONOGRAPH-AMERICAN GEOPHYSICAL UNION*, 93,  
2449 pp.213-218.
- 2450 Perroomian, V., El-Alaoui, M., Abdalla, M.A. and Zelenyi, L.M. (2007). A comparison of solar wind and  
2451 ionospheric plasma contributions to the September 24–25, 1998 magnetic storm. *Journal of*  
2452 *atmospheric and solar-terrestrial physics*, 69(3), pp.212-222.

- 2453 Peterson, W. K., L. Andersson, B. C. Callahan, H. L. Collin, J. D. Scudder, and A. W. Yau (2008). Solar-  
 2454 minimum quiet time ion energization and outflow in dynamic boundary related coordinates.  
 2455 *Journal of Geophysical Research: Space Physics*, 113, A07222, doi:10.1029/2008JA013059.
- 2456 Peterson, W. K., H. L. Collin, O. W. Lennartsson, and A. W. Yau (2006). Quiet time solar illumination  
 2457 effects on the fluxes and characteristic energies of ionospheric outflow. *Journal of Geophysical*  
 2458 *Research: Space Physics*, 111, A11S05, doi: 10.1029/2005JA011596.
- 2459 Phan, T. D., Paschmann, G., Gosling, J. T., Oieroset, M., Fujimoto, M., Drake, J. F., & Angelopoulos, V.  
 2460 (2013). The dependence of magnetic reconnection on plasma  $\beta$  and magnetic shear: Evidence  
 2461 from magnetopause observations. *Geophysical Research Letters*, 40(1), 11-16.
- 2462 Pollock, C. J., Burch, J. L., Henderson, M. G., Jahn, J. M., McComas, D. J., Mende, S. B., et al. (2003). The  
 2463 role and contributions of energetic neutral atom (ENA) imaging in magnetospheric substorm  
 2464 research. In *Magnetospheric Imaging—The Image Prime Mission* (pp. 155-182). Springer,  
 2465 Dordrecht.
- 2466 Runov, A., Angelopoulos, V., Artemyev, A., Birn, J., Pritchett, P. L., & Zhou, X.-Z. (2017). Characteristics of  
 2467 ion distribution functions in dipolarizing flux bundle: Event studies. *Journal of Geophysical*  
 2468 *Research: Space Physics*, 122 (6), 5965-5978. doi: 10.1002/2017ja024010.
- 2469 Sandel, B. R., J. Goldstein, D. L. Gallagher, and M. Spasojevic (2003). Extreme Ultraviolet Imager  
 2470 Observations of the Structure and Dynamics of the Plasmasphere. *Space Science Reviews*, 109,  
 2471 25–46, doi:10.1023/B:SPAC.0000007511.47727.5b.
- 2472 Sauvaud, J.-A., R. Lundin, H. Rème, J. P. McFadden, C. Carlson, G. K. Parks, et al. (2001). Intermittent  
 2473 thermal plasma acceleration linked to sporadic motions of the magnetopause, first Cluster results,  
 2474 *Annales Geophysicae*, 19, doi:10.5194/angeo-19-1523- 2001.
- 2475 Schillings, A., Slapak, R., Nilsson, H., Yamauchi, M., Dandouras, I., & Westerberg, L. G. (2019). Earth  
 2476 atmospheric loss through the plasma mantle and its dependence on solar wind parameters. *Earth,*  
 2477 *Planets and Space*, 71(1), 1-13.
- 2478 Schunk, R. W., Raitt, W. J., & Banks, P. M. (1975). Effect of electric fields on the daytime high-latitude E  
 2479 and F regions. *Journal of Geophysical Research*, 80(22), 3121-3130.
- 2480 Schunk, R. W. (2007). Time-dependent simulations of the global polar wind. *Journal of atmospheric and*  
 2481 *solar-terrestrial physics*, 69(16), 2028-2047.
- 2482 Seki, K., Hirahara, M., Hoshino, M., Terasawa, T., Elphic, R. C., Saito, Y., et al, (2003). Cold ions in the hot  
 2483 plasma sheet of Earth's magnetotail. *Nature*, 422(6932), 589-592.
- 2484 Shay, M. A., Drake, J. F., & Swisdak, M. (2007). Two-scale structure of the electron dissipation region  
 2485 during collisionless magnetic reconnection. *Physical review letters*, 99(15), 155002.
- 2486 Shay, M. A., Drake, J. F., Denton, R. E., & Biskamp, D. (1998). Structure of the dissipation region during  
 2487 collisionless magnetic reconnection. *Journal of Geophysical Research: Space Physics*, 103 (A5),  
 2488 9165-9176. doi: 10.1029/97ja03528.
- 2489 Shay, M. A., T. D. Phan, C. C. Haggerty, M. Fujimoto, J. F. Drake, K. Malakit, P. A. Cassak, and M. Swisdak  
 2490 (2016). Kinetic signatures of the region surrounding the X line in asymmetric (magnetopause)  
 2491 reconnection. *Geophysical Research Letters*, 43, 4145–4154, doi:10.1002/2016GL069034.
- 2492 Sheeley, B. W., Moldwin, M. B., Rassoul, H. K., & Anderson, R. R. (2001). An empirical plasmasphere and  
 2493 trough density model: CRRES observations. *Journal of Geophysical Research: Space*  
 2494 *Physics*, 106(A11), 25631-25641.
- 2495 Shelley, E. G., Johnson, R. G., and R. D. Sharp (1972). Satellite observations of energetic heavy ions  
 2496 during a geomagnetic storm. *Journal of Geophysical Research: Space Physics*, 77(31), 6104-6110.

- 2497 Shen, Y., D. J. Knudsen, J. K. Burchill, A. D. Howarth, A. W. Yau, D. M. Miles, H. G. James, G. W. Perry, and  
2498 L. Cogger (2018). Low-altitude ion heating, downflowing ions, and elf waves in the return current  
2499 region. *Journal of Geophysical Research: Space Physics*, 123(4), 3087–3110,  
2500 doi:10.1002/2017JA024955.
- 2501 Slapak, R., M. Hamrin, T. Pitkänen, M. Yamauchi, H. Nilsson, T. Karlsson, A. Schillings (2017).  
2502 Quantification of the total ion transport in the near-Earth plasma sheet. *Annales Geophysicae*,  
2503 Volume 35, Issue 4, 2017, pp.869-877, doi:10.5194/angeo-35-869-2017.
- 2504 Slapak, R., H. Nilsson, L. G. Westerberg (2015) O<sup>+</sup> transport in the dayside magnetosheath and its  
2505 dependence on the IMF direction, *Annales Geophysicae*, 33(3), 301-307, doi:10.5194/angeo-33-  
2506 301-2015.
- 2507 Slapak, R., A. Schillings, H. Nilsson, M. Yamauchi, L.-G. Westerberg, and I. Dandouras (2017).  
2508 Atmospheric loss from the dayside open polar region and its dependence on geomagnetic activity:  
2509 implications for atmospheric escape on evolutionary timescales, *Annales Geophysicae*, 35(3), 721–  
2510 731, doi:10.5194/angeo-35-721-2017.
- 2511 Spasojevic, M., and Sandel, B. R. (2010). Global estimates of plasmaspheric losses during moderate  
2512 disturbance intervals. In *Annales Geophysicae*, 28(1), 27-36.
- 2513 Sorathia, K. A., V. G. Merkin, A. Y. Ukhorskiy, R. C. Allen, K. Nykyri, and S. Wing (2019). Solar wind ion  
2514 entry into the magnetosphere during northward IMF. *Journal of Geophysical Research: Space*  
2515 *Physics*, 124(7), 5461-5481.
- 2516 Spinnagr, S. F., Hesse, M., Tenfjord, P. Norgren, C., Kolsto, H. M., Kwagala, N. K., and Jorgensen, T. M.  
2517 (2020). The micro-macro coupling of mass-loading symmetric magnetic reconnection with cold  
2518 ions. *Geophysical Research Letters*, submitted.
- 2519 Strangeway, R. J., R. E. Ergun, Y. J. Su, C. W. Carlson, and R. C. Elphic (2005). Factors controlling  
2520 ionospheric outflows as observed at intermediate altitudes. *Journal of Geophysical Research*, 110,  
2521 A03221, doi: 10.1029/2004JA010829
- 2522 Su, Y.-J., J. L. Horwitz, T. E. Moore, B. L. Giles, M. O. Chandler, P. D. Craven, M. Hirahara, and C. J. Pollock  
2523 (1998). Polar wind survey with the Thermal Ion Dynamics Experiment/Plasma Source Instrument  
2524 suite aboard POLAR. *Journal of Geophysical Research*, 103, 29,305–29,338,  
2525 doi:10.1029/98JA02662.
- 2526 Su, Y. J., Borovsky, J. E., Thomsen, M. F., Elphic, R. C., & McComas, D. J. (2000). Plasmaspheric material at  
2527 the reconnecting magnetopause. *Journal of Geophysical Research: Space Physics*, 105(A4), 7591-  
2528 7600.
- 2529 Svenes, K. R., B. Lybekk, A. Pedersen, and S. Haaland (2008). Cluster observations of near-Earth  
2530 magnetospheric lobe plasma densities – a statistical study. *Annales Geophysicae*, 26, 2845 – 2852.
- 2531 Swisdak, M., M. Opher, J. F. Drake, & F. Alouani Bibi (2010). The vector direction of the interstellar  
2532 magnetic field outside the heliosphere. *Astrophysical Journal*, 710(2), 1769 –1775,  
2533 doi:10.1088/0004-637X/710/2/1769.
- 2534 Swisdak, M., B. N. Rogers, J. F. Drake, & M. A. Shay (2003). Diamagnetic suppression of component  
2535 magnetic reconnection at the magnetopause. *Journal of Geophysical Research*, 108(A5), 1218,  
2536 doi:10.1029/2002JA009726.

- 2537 Tenfjord, P., M. Hesse, C. Norgren, S. F. Spinnangr, and H. Kolstø (2019), The Impact of Oxygen on the  
 2538 Reconnection Rate. *Geophysical Research Letters*, 46(12), 6195–6203,  
 2539 doi:10.1029/2019GL082175.10
- 2540 Tenfjord, P., N. Østgaard, S. E. Haaland, K. Snekvik, K. M. Laundal, J. P. Reistad, et al. (2018). How the IMF  
 2541 By Induces a Local By Component During Northward IMF Bz and Characteristic Timescales. *Journal*  
 2542 *of Geophysical Research: Space Physics*, 123(5), 3333–3348, doi:10.1002/2018JA025186.
- 2543 Tenfjord, P., Hesse, M., Norgren, C., Spinnangr, S. F., Kolstø, H., & Kwagala, N. (2020). Interaction of Cold  
 2544 Streaming Protons with the Reconnection Process. *Journal of Geophysical Research: Space*  
 2545 *Physics*, 125(6), e2019JA027619.
- 2546 Thorne, R. M. (2010). Radiation belt dynamics: The importance of wave-particle  
 2547 interactions. *Geophysical Research Letters*, 37(22).
- 2548 Toledo-Redondo, S., André, M., Khotyaintsev, Y. V., Lavraud, B., Vaivads, A., Graham, D. B., et al. (2017).  
 2549 Energy budget and mechanisms of cold ion heating in asymmetric magnetic reconnection. *Journal*  
 2550 *of Geophysical Research: Space Physics*, 122(9), 9396-9413.
- 2551 Toledo-Redondo, S., André, M., Khotyaintsev, Y. V., Vaivads, A., Walsh, A., Li, W., et al. (2016a). Cold ion  
 2552 demagnetization near the X-line of magnetic reconnection. *Geophysical Research Letters*, 43(13),  
 2553 6759-6767.
- 2554 Toledo-Redondo, S., André, M., Vaivads, A., Khotyaintsev, Y. V., Lavraud, B., Graham, D. B., et al.  
 2555 (2016b). Cold ion heating at the dayside magnetopause during magnetic  
 2556 reconnection. *Geophysical Research Letters*, 43(1), 58-66.
- 2557 Toledo-Redondo, S., Dargent, J., Aunai, N., Lavraud, B., André, M., Li, W., et al. (2018). Perpendicular  
 2558 current reduction caused by cold ions of ionospheric origin in magnetic reconnection at the  
 2559 magnetopause: Particle-in-cell simulations and spacecraft observations. *Geophysical Research*  
 2560 *Letters*, 45(19), 10-033.
- 2561 Toledo-Redondo, S., Lavraud, B., Fuselier, S. A., André, M., Khotyaintsev, Y. V., Nakamura, N., et al.  
 2562 (2019). Electrostatic spacecraft potential structure and wake formation effects for  
 2563 characterization of cold ion beams in the Earth's magnetosphere. *Journal of Geophysical Research:*  
 2564 *Space Physics*, 124, 10048– 10062. doi:10.1029/2019JA027145
- 2565 Toledo-Redondo, S., A. Vaivads, M. André, and Y. V. Khotyaintsev (2015). Modification of the Hall physics  
 2566 in magnetic reconnection due to cold ions at the Earth's magnetopause. *Geophysical Research*  
 2567 *Letters*, 42(15), 6146–6154, doi:10.1002/2015GL065129.
- 2568 Torkar, K., R. Nakamura, M. Tajmar, C. Scharlemann, H. Jeszenszky, G. Laky, et al. (2016), Active  
 2569 Spacecraft Potential Control Investigation. *Space Science Reviews*, 199, 515–544,  
 2570 doi:10.1007/s11214-014-0049-3.
- 2571 Varney, R.H., Wiltberger, M., Zhang, B., Lotko, W. and Lyon, J., 2016a. Influence of ion outflow in  
 2572 coupled geospace simulations: 1. Physics-based ion outflow model development and sensitivity  
 2573 study. *Journal of Geophysical Research: Space Physics*, 121(10), pp.9671-9687.
- 2574 Varney, R.H., Wiltberger, M., Zhang, B., Lotko, W. and Lyon, J., 2016b. Influence of ion outflow in  
 2575 coupled geospace simulations: 2. Sawtooth oscillations driven by physics-based ion  
 2576 outflow. *Journal of Geophysical Research: Space Physics*, 121(10), pp.9688-9700.
- 2577 Vasylunas, V. M. (1975). Theoretical models of magnetic field line merging. *Reviews of*  
 2578 *Geophysics*, 13(1), 303-336.
- 2579 Vasylunas, V. M., (1983). Plasma distribution and flow, in *Physics of the Jovian Magnetosphere*, edited  
 2580 by A. J. Dessler, pp. 395-453, Cambridge University Press, New York.

- 2581 Vernisse, Y., Lavraud, B., Faganello, M., Fadanelli, S., Sisti, M., Califano, F., et al. (2020). Latitudinal  
 2582 Dependence of the Kelvin-Helmholtz Instability and Beta Dependence of Vortex-Induced High-  
 2583 Guide Field Magnetic Reconnection. *Journal of Geophysical Research: Space Physics*, 125(5),  
 2584 e2019JA027333.
- 2585 Vines, S. K., Fuselier, S. A., Trattner, K. J., Burch, J. L., Allen, R. C., Petrinec, S. M., et al., (2017).  
 2586 Magnetospheric ion evolution across the low-latitude boundary layer separatrix. *Journal of*  
 2587 *Geophysical Research: Space Physics*, 122(10), 10-247.
- 2588 Walsh, B. M., Sibeck, D. G., Nishimura, Y., & Angelopoulos, V. (2013). Statistical analysis of the  
 2589 plasmaspheric plume at the magnetopause. *Journal of Geophysical Research: Space*  
 2590 *Physics*, 118(8), 4844-4851.
- 2591 Wang, S., Kistler, L. M., Mouikis, C. G., Liu, Y., & Genestreti, K. J. (2014). Hot magnetospheric O<sup>+</sup> and cold  
 2592 ion behavior in magnetopause reconnection: Cluster observations. *Journal of Geophysical*  
 2593 *Research: Space Physics*, 119(12), 9601-9623.
- 2594 Wang, S., Kistler, L. M., Mouikis, C. G., & Petrinec, S. M. (2015). Dependence of the dayside  
 2595 magnetopause reconnection rate on local conditions. *Journal of Geophysical Research: Space*  
 2596 *Physics*, 120(8), 6386-6408.
- 2597 Westerberg, L.-G. (2019). Earth atmospheric loss through the plasma mantle and its dependence on  
 2598 solar wind parameters. *Earth, Planets and Space*, 71(1), doi:10.1186/s40623-019-1048-0
- 2599 Welling, D. T., André, M., Dandouras, I., Delcourt, D., Fazakerley, A., Fontaine, D., et al. (2015). The  
 2600 Earth: Plasma sources, losses, and transport processes. *Space Science Reviews*, 192(1-4), 145-208.
- 2601 Welling, D.T., Barakat, A.R., Eccles, J.V., Schunk, R.W. and Chappell, C.R. (2016). Coupling the generalized  
 2602 polar wind model to global magnetohydrodynamics: Initial results. *AGU Monograph. Series*
- 2603 Welling, D.T., Jordanova, V.K., Zaharia, S.G., Glocer, A. and Toth, G. (2011). The effects of dynamic  
 2604 ionospheric outflow on the ring current. *Journal of Geophysical Research: Space Physics*, 116(A2).
- 2605 Welling, D.T. and Liemohn, M.W. (2014). Outflow in global magnetohydrodynamics as a function of a  
 2606 passive inner boundary source. *Journal of Geophysical Research: Space Physics*, 119(4), pp.2691-  
 2607 2705.
- 2608 Welling, D.T. and Zaharia, S.G. (2012). Ionospheric outflow and cross polar cap potential: What is the  
 2609 role of magnetospheric inflation?. *Geophysical research letters*, 39(23).
- 2610 Whipple, E. C. (1981). Potentials of surfaces in space, Rep. Prog. Phys., 44, 1197–1250,  
 2611 doi:10.1088/0034-4885/44/11/002
- 2612 Wilken, B., Q. G. Zong, I. A. Daglis, T. Doke, S. Livi, K. Maezawa, Z. Y. Pu, S. Ullaland, and T. Yamamoto  
 2613 (1995). Tailward flowing energetic oxygen ion bursts associated with multiple flux ropes in the  
 2614 distant magnetotail: GEOTail observations. *Geophysical Research Letters*, 22(23), 3267–3270,  
 2615 doi:10.1029/95GL02980.
- 2616 Winglee, R.M., 1998. Multi-fluid simulations of the magnetosphere: The identification of the geopause  
 2617 and its variation with IMF. *Geophysical research letters*, 25(24), pp.4441-4444.
- 2618 Winglee, R. M., Chua, D., Brittnacher, M., Parks, G. K., & Lu, G. (2002). Global impact of ionospheric  
 2619 outflows on the dynamics of the magnetosphere and cross-polar cap potential. *Journal of*  
 2620 *Geophysical Research: Space Physics*, 107(A9), SMP-11.
- 2621 Winglee, R. M., & Harnett, E. (2011). Influence of heavy ionospheric ions on substorm onset. *Journal of*  
 2622 *Geophysical Research: Space Physics*, 116(A11).

- 2623 Wiltberger, M., Lotko, W., Lyon, J.G., Damiano, P. and Merkin, V. (2010). Influence of cusp O<sup>+</sup> outflow on  
 2624 magnetotail dynamics in a multifluid MHD model of the magnetosphere. *Journal of Geophysical*  
 2625 *Research: Space Physics*, 115(A10).
- 2626 Wygant, J. R., Cattell, C. A., Lysak, R., Song, Y., Dombek, J., McFadden, J., et al. (2005). Cluster  
 2627 observations of an intense normal component of the electric field at a thin reconnecting current  
 2628 sheet in the tail and its role in the shock-like acceleration of the ion fluid into the separatrix  
 2629 region. *Journal of Geophysical Research: Space Physics*, 110 (A9). doi: 10.1029/2004ja010708.
- 2630 Xu, Y., Fu, H. S., Norgren, C., Toledo-Redondo, S., Liu, C. M., & Dong, X. C. (2019). Ionospheric cold ions  
 2631 detected by mms behind dipolarization fronts. *Geophysical Research Letters*, 46 (14), 7883-7892,  
 2632 doi:10.1029/2019gl083885.
- 2633 Yamada, M., R. Kulsrud, and H. Ji (2010). Magnetic reconnection. *Reviews of Modern Physics*, 82(1), 603–  
 2634 664, doi:10.1103/RevModPhys.82.603.
- 2635 Yamauchi (2019). Terrestrial ion escape and relevant circulation in space. *Annales Geophysicae*, 37,  
 2636 1197-1222.
- 2637 Yau, A. W., T. Abe, M. André, A. D. Howart and W. K. Peterson (2020). Ionospheric ion acceleration and  
 2638 transport, Space Physics and Aeronomy Collection Volume 2: Magnetospheres in the Solar  
 2639 System, Geophysical Monograph, Published 2021 by John Wiley & Sons, DOI:  
 2640 10.1002/9781119507512
- 2641 Yau, A. W., T. Abe, and W. K. Peterson (2007). The polar wind: Recent observations. *Journal of*  
 2642 *Atmospheric and Solar-Terrestrial Physics*, 69, 1936–1983, doi: 10.1016/j.jastp.2007.08.010.
- 2643 Yau, A. W., and M. André (1997). Sources of Ion Outflow in the High Latitude Ionosphere. *Space Science*  
 2644 *Reviews*, 80, 1–25, doi:10.1023/A:1004947203046.
- 2645 Yau, A.W., Peterson, W.K., & Abe, T. (2017). Measurements of ion outflows from the Earth’s ionosphere,  
 2646 In Magnetosphere-Ionosphere Coupling in the Solar System, Geophysical Monograph 222, First  
 2647 Edition. American Geophysical Union. Published by John Wiley & Sons, Inc.
- 2648 Young, D. T., Balsiger, H., & Geiss, J. (1982). Correlations of magnetospheric ion composition with  
 2649 geomagnetic and solar activity. *Journal of Geophysical Research: Space Physics*, 87(A11), 9077-  
 2650 9096.
- 2651 Young, D. T., Burch, J. L., Gomez, R. G., De Los Santos, A., Miller, G. P., Wilson, P., ... & Pollock, C. J.  
 2652 (2016). Hot plasma composition analyzer for the magnetospheric multiscale mission. *Space*  
 2653 *Science Reviews*, 199(1-4), 407-470.
- 2654 Zhang, B., Brambles, O. J., Wiltberger, M., Lotko, W., Ouellette, J. E., & Lyon, J. G. (2016). How does mass  
 2655 loading impact local versus global control on dayside reconnection?. *Geophysical Research*  
 2656 *Letters*, 43(5), 1837-1844.
- 2657 Zhang, B., Brambles, O. J., Cassak, P. A., Ouellette, J. E., Wiltberger, M., Lotko, W., & Lyon, J. G. (2017).  
 2658 Transition from global to local control of dayside reconnection from ionospheric-sourced mass  
 2659 loading. *Journal of Geophysical Research: Space Physics*, 122(9), 9474-9488.
- 2660 Zhang, B., Brambles, O. J., Lotko, W., & Lyon, J. G. (2020). Is nightside outflow required to induce  
 2661 magnetospheric sawtooth oscillations. *Geophysical Research Letters*, 47, e2019GL086419. doi :  
 2662 [10.1029/2019GL086419](https://doi.org/10.1029/2019GL086419)
- 2663 Zheng, Y., Moore, T.E., Mozer, F.S., Russell, C.T. and Strangeway, R.J. (2005). Polar study of ionospheric  
 2664 ion outflow versus energy input. *Journal of Geophysical Research: Space Physics*, 110(A7).

2665 Zong, Q. G., B. Wilken, J. Woch, T. Mukai, T. Yamamoto, G. D. Reeves, et al. (1998), Energetic oxygen ion  
2666 bursts in the distant magnetotail as a product of intense substorms: Three case studies. *Journal of*  
2667 *Geophysical Research*, 103(A), 20,339–20,364, doi:10.1029/97JA01146.